DIAGNOSING SUBSYNCHRONOUS VIBRATIONS IN TURBOMACHINERY – STABLE OR UNSTABLE

A Thesis

by

VINAYAKA NARAYANAN RAJAGOPALAN

Submitted to the Office of Graduate Studies of
Texas A&M University
in partial fulfillment of the requirements for the degree of

MASTER OF SCIENCE

August 2007

Major Subject: Mechanical Engineering

DIAGNOSING SUBSYNCHRONOUS VIBRATIONS IN TURBOMACHINERY – STABLE OR UNSTABLE

A Thesis

by

VINAYAKA NARAYANAN RAJAGOPALAN

Submitted to the Office of Graduate Studies of
Texas A&M University
in partial fulfillment of the requirements for the degree of

MASTER OF SCIENCE

Approved by:

Chair of Committee,	John M.Vance
Committee Members,	Dara W. Childs
	Guy Battle
Head of Department,	Dennis O'Neal

August 2007

Major Subject: Mechanical Engineering

ABSTRACT

Diagnosing Subsynchronous Vibrations in Turbomachinery – Stable or Unstable.

(August 2007)

Vinayaka Narayanan Rajagopalan, B.E., R.V College of Engineering, India

Chair of Advisory Committee: Dr. John M.Vance

Rotordynamic instability, commonly observed as subsynchronous vibration, is a serious problem that can cause heavy damage to a turbomachine or make it incapable of operation because of high vibration levels. All subsynchronous vibrations, howver, are not necessarily unstable. If the amplitude of the subsynchronous vibration is large, it can cause damage to seals, bearings, or process wheels. If it is small, the question arises as to whether it has the potential to grow larger ("instability") or whether it is benign and harmless. A way to know would be helpful.

The objective of this study is to signal analyze subsynchronous vibrations in turbomachinery and distinguish benign subsynchronous vibration from the true potential instabilities. Effort is also made to identify unique signatures to a cause to aid in faster diagnosis.

First, a computer simulation study is conducted on four rotors, including two gas-reinjection compressors that went unstable, to examine the possibility of using the change in the synchronous phase angle as a possible indicator of impending instability. Results indicate that, phase angle can be used as an indicator of potential instability, provided that a judicious approach is used, as the synchronous phase angle, by itself,

cannot classify between benign and unstable motion. It can confirm, however, a true rotordynamic instability.

Several causes of subsynchronous vibration in turbomachinery are studied experimentally. Signals are measured from a rotor having a dead-band clearance between the bearing outer race and the housing. It is studied as another example of a subsynchronous vibration arising because of a benign cause. The effect is studied with the rotor in the horizontal and vertical positions, and clear indicators are observed that confirm the subsynchronous vibration to be benign in nature.

Dry friction whip is also experimentally produced on a test rig. The measurements show that dry friction whip defies the general rules of thumb for diagnosing a true instability and at the same time is a very violent one as well.

The last phenomenon to be studied is coupled lateral-torsional vibrations. A special test rig was built to study this effect, and clear indicators have been identified to distinguish the response as resulting from torsional vibrations and also classify it as a benign source of subsynchronous vibration. The test rig is also mathematically modeled to predict its torsional natural frequencies.

DEDICATION

To my parents and Dr.Vance

"The question is not what you look at, but what you see."

- Henry David Thoreau

ACKNOWLEDGMENTS

I would like to express my deep appreciation and gratitude to Dr. John Vance for giving me the opportunity to work with him at the Turbomachinery Laboratory. Without his guidance and input this thesis would not have been possible. I am also grateful to Dr. Dara Childs and Dr. Guy Battle for consenting to serve on my advisory committee.

I would like to thank my friends at the Turbomachinery Laboratory, especially Aaron Schomerus, for assisting me with my experiments, Adam Jones for helping me with the electronics, Ahmed Gamal for his innovative ideas and Mohsin Jafri for his analytical input. Special thanks to Eddie Denk for helping me with my test rig hardware and setup.

I would also like to thank the Turbomachinery Research Consortium for sponsoring this study for two consecutive years.

Last but definitely not least, my parents have been unwavering in their support and encouragement. They are the rock upon which I have built my life and this thesis is the result of all their sacrifices for me through the years.

NOMENCLATURE

c	Damping, lb-s/in (N-s/m)
D	Diameter, in (m)
G	Shear modulus, psi (Pa)
I	Polar moments of inertia, lb-in-sec^2 (kg-m^2)
k	Lateral stiffness, lb/in (N/m)
K	Shaft torsional stiffness, lb-in/rad (N-m/rad)
L	Length, in (m)
m	modal mass, lb-sec^2/in (kg)
N	Gear ratio
r	Rotor synchronous response, in (m)
T	Instantaneous torque, lb-in (N-m)
(x,y)	Rotor linear displacements in two orthogonal directions, in (m)
β	Phase angle, rad
θ	Instantaneous torsional degree of freedom, radians
κ	Cross-coupled stiffness, lb/in (N/m)
ω	Excitation frequency, rad/sec

Subscripts

1	Refers to D.C. motor location
2	Refers to primary gear location
3	Refers to secondary gear location
4	Refers to brake wheel location

p	Refers to primary shaft
s	Refers to secondary shaft

TABLE OF CONTENTS

Page

CHAPTER Page

LIST OF FIGURES

Page

Page

Page

Page

Page

CHAPTER I

INTRODUCTION

Turbomachinery design has always been done with emphasis on aero-thermodynamic performance. Over the years, this has resulted in higher operating speeds, more stages, higher pressures, higher temperatures, tighter impeller and seal clearances, and lighter machines with smaller footprints – all with a view to offer the customer, the best value for the investment. In this race to build high-performance turbomachinery, machines are often designed to operate on the absolute knife-edge of maximum technical capability. This leaves little or no room for error and often, a small change of one operating parameter can lead to engine breakdown or component damage. The costs involved when a turbomachine stops working are enormous. Often, whole production plants are brought to a standstill when a machine is shutdown. Apart form the costs of broken equipment, the loss in terms of production time run into millions of dollars with each passing day.

Rotordynamic instability is one such problem which can cause heavy damage to a turbomachine or make it incapable of operation due to high vibration. Vance [1] explains rotordynamic instability as one characterized by whirling of the rotor-bearing system at frequencies other than shaft speed. It is normally characterized by a non-tracking, non-synchronous vibration, which is almost independent of change in rotor

---

This thesis follows the style of the Journal of Engineering for Gas Turbines and Power.

speed. Instabilities are normally observed in rotors that operate super-critically, with the self-excited non-synchronous whirl usually occurring at the first eigenvalue of free vibration. The cause of rotordynamic instability is never imbalance of the rotor. It is a self-excited vibration. A typical compressor instability is shown in Fig 1. In an unstable rotor, amplitudes can increase exponentially without limit leading to destructive consequences. Often however, the amplitudes become bounded in limit cycles due to non-linear effects, and if the amplitudes are not high enough to damage seals and bearings, the instability is tolerated and the machine is allowed to run. However, the question arises as to whether a subsynchronous vibration is potentially unstable or not.

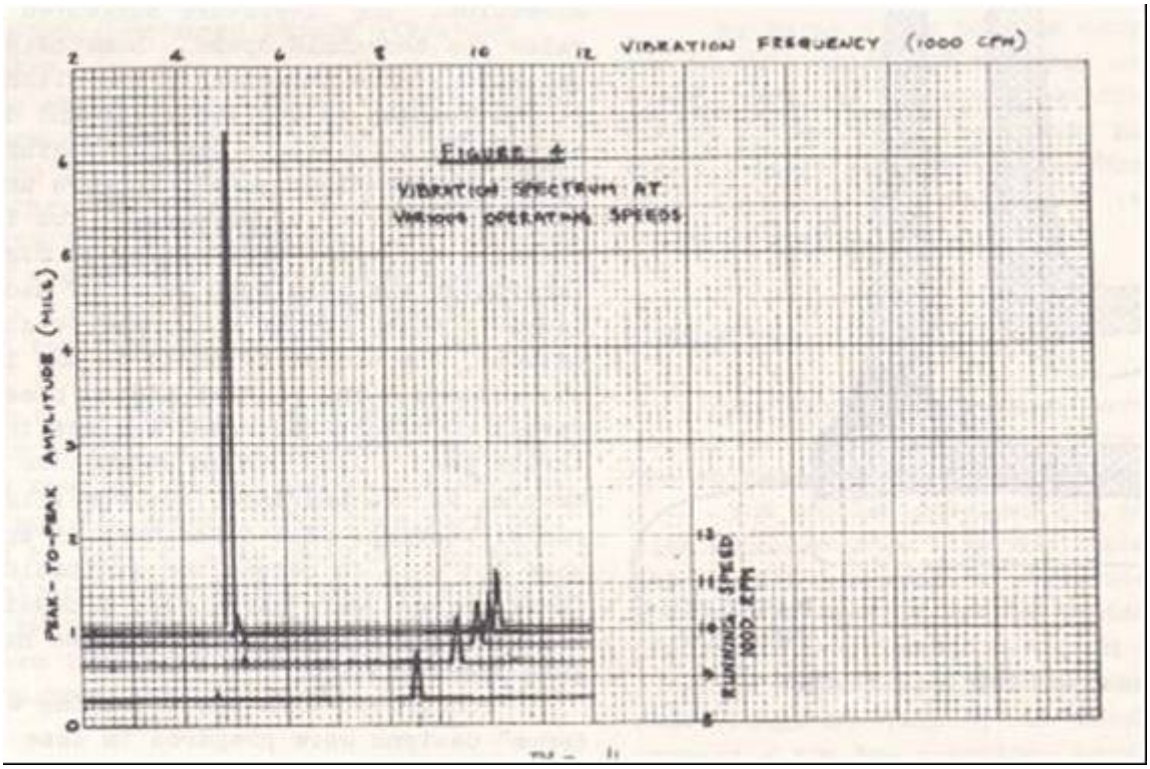

Fig 1: Typical rotordynamic instability, Fowlie and Miles [2]

Objective

Sometimes, during machine health monitoring, a signal may be observed which appears like an instability. For example, a frequency spectrum could show a subsynchronous vibration at an eigenvalue of free vibration that does not die out with time. Normally, the engine is immediately shutdown for possibly a strip examination. As mentioned earlier, this leads to mounting costs in terms of lost production time. However, many phenomena that are not potentially unstable can give an 'instability-like' signal.

The objective of this thesis is to analyze subsynchronous vibrations, classify them as unstable or benign vibrations and if possible, find unique indicators to the cause of the vibration.

Literature Review

Since Newkirk [3] first published his findings on internal friction related instability giving rise to subsynchronous vibrations in GE blast furnace compressors, there have been innumerable instances and records of rotordynamic instabilities due to various phenomena. Kimball [4] built a test rig to study internal friction and proposed a mathematical model for the same. Kimball [4] and Newkirk [3] both observed that the internal friction instability occurred only in super-critical rotors and that the shaft whipping was always at its first critical speed. This shaft whipping was independent of the mass imbalance of the rotor or its running speed. Ehrich and Childs [5] discuss some of the common instability causing phenomena and offer general methods to identify these and also preventive measures that can be taken to preempt these instabilities.

Internal friction, half-frequency oil whip, high cross-coupled forces from labyrinth/annular liquid seals, Alford's forces and trapped rotor fluid are some of the common causes of instability in turbomachines. A common indicator for all the instabilities is an observed frequency independent of rotor running speed or any external stimulus and occurring at or near one of the shaft natural frequencies. The amplitude of this vibration is high or continues to increase as the rotor running speed or power increases. The whirl direction is usually forward.

Reverse whirl instabilities are a rarely observed phenomenon in turbomachinery. However, one very destructive form of backward whirl instability is dry-friction whip. Black [6] developed a model to predict the motion due to rubs between a rotor and stator, with Coulomb friction at the rubbing interface. His analysis predicts the frequency range in which dry friction whirl occurs, the Coulomb friction μ required to maintain dry friction whirl and also the onset speed of dry friction whip. Childs and Bhattacharya [7] combine and analyze results from recent dry friction whip experiments and cite examples that agree with and contradict Black's solutions. Schultheis [8] presents a detailed work on diagnosing rubs in turbomachinery. He mentions some of the indicators as large 1X vibration with shifting phase, increased rotor resonance frequency and deformed or odd shaped orbits as some of the indicators of rotor-stator rubs. Yu et. al. [9] conducted annular rub experiments with Teflon and bronze seals and came to similar conclusions as Schultheis. However, they also explore the effect of mass unbalance on the onset speed of whip and effect of shaft speed on maintaining 360^0 annular contact.

There are numerous cases in literature of compressors and other turbomachinery going unstable in the field and the steps taken to eliminate the instabilities. One of the more famous cases of compressors going unstable is that of Phillips Norway's Ekofisk Compressor and Chevron's Kaybob Compressor, for not only the long time-span taken to solve the instabilities, but also for the millions of dollars lost in petroleum production with each passing day. A number of known fixes were tried before the compressors began to work normally, many months after the instability first occurred. It is now believed that large cross-coupled forces in the central labyrinth seal were the most likely primary cause of the instability. Smith [10] and Fowlie and Miles [2] describe in detail the Kaybob Compressor problem and Doyle [11] and Wachel [12] describe the problem and the solution path for the Ekofisk Compressor.

There are also a number of cases in literature where there have been instability-like signals (subsynchronous vibrations) that have actually been from benign sources. Wachel and Szenasi [13] report an instance where the third torsional natural frequency of a compressor, which coincided with the first lateral critical speed, was excited and showed up in the lateral spectrum as a subsynchronous vibration and mislead engineers on the wrong solution path. The source of the apparent instability was suspected only after there was some damage to gear teeth and a torsiograph was then used to confirm the presence of torsional vibrations. The solution was to change the lateral support stiffness, to move the first lateral critical speed away from the third torsional natural frequency. One other phenomenon that causes benign subsynchronous motion in turbomachinery is a bearing with a significant clearance between its outer race and the

housing. Bently [14] experimentally showed that the constantly changing 'normal tight' and 'normal loose' condition of a bearing causes fractional frequency whirl. In all his experiments, the tracking subsynchronous motion started only at speeds above close to or above the rotor first natural frequency. He also mentions that the ½ rotative speed motion occurs in a rotor speed bandwidth of 6100 rpm to 6700 rpm, with a rotor first critical speed being at 3470 rpm. Bently repeatedly calls the tracking subsynchronous vibrations as "Mathieu action", but does not provide a mathematical model using the Mathieu equation. Childs [15] proposed and solved the mathematical model for a Jeffcott rotor on loose bearing and predicted that ½X and 1/3X speed dependent subsynchronous vibrations would be most likely to occur. Being a tracking non-synchronous motion, this phenomenon is benign in nature.

In a new approach to the subject, Ertas, Kar and Vance [16] began a study on phenomena that gave instability-like signatures but were actually benign. They identified a number of possible indicators that could help differentiate between genuine and pseudo instability signals. Kar and Vance [17] further continued the study by analyzing subsynchronous vibrations from a non-linear support stiffness and found clear indicators that identified these vibrations to be benign in nature. They also conducted studies on the possibility of using phase angle as a potential indicator of instability and proposed further research in that area. This thesis is a continuation of the study on signal analyzing subsynchronous vibrations and aims at accurately diagnosing certain phenomena causing instability or false-instability signals and being able to correctly differentiate between them with a view to saving down-time of turbomachinery on the field.

Research Procedure

Experiments were conducted on a Bently Rotor Kit with loose ball-bearing supports. The resulting subsynchronous vibration was analyzed to classify it as unstable or benign vibrations.

Dry friction whip was experimentally simulated on a modified Bently Rotor Kit. Unique indicators to identify and classify dry friction whip were observed.

A theoretical analysis of four rotors was conducted in XLTRC^2 to identify the possibility of using phase angle as a potential indicator of instability. A new finding is reported.

A new test rig was built to study subsynchronous motion arising from torsional effects. A torsional mathematical model for the rotor was solved to predict the torsional natural frequencies. Subsynchronous motion at the first torsional frequency was then excited externally through an electric circuit and the subsynchronous motion was signal analyzed.

CHAPTER II

PHASE ANGLE ANALYSIS

Introduction

The change of the synchronous phase angle near the critical speed of a potentially unstable system was reported by Kar and Vance [17]. In most cases, the cause of a machine going unstable is the cross-coupling in the system exceeding a certain critical value (say κ). κ depends on the total effective damping in the rotor. In general, the effect of cross-coupled stiffness on whirl stability is shown in Fig 2 below. The abscissa in the figure shows the ratio of the cross-coupling κ in the system to the effective shaft stiffness. The ordinate gives the non-dimensional form of the real part of the eigenvalue and is an indicator of system stability. Therefore, for a rotor, given the effective damping, there exists a certain value of κ at which the rotor can potentially go unstable. In practice however, it is not easy to measure κ, determine effective system damping and then compute if the system is stable or not. One system parameter that depends on both the cross-coupled stiffness and damping is the phase angle β, and it can be easily measured real-time provided good instrumentation is available.

Mathematically, the relationship between the phase angle, damping and cross-coupled stiffness can be seen from the simple Jeffcott model of a rotor, given by:

$$m\ddot{x} + c\dot{x} + kx + \kappa_{xy} y = m\omega^2 u \cos(\omega t)$$

$$m\ddot{y} + c\dot{y} + ky + \kappa_{yx} x = m\omega^2 u \sin(\omega t)$$

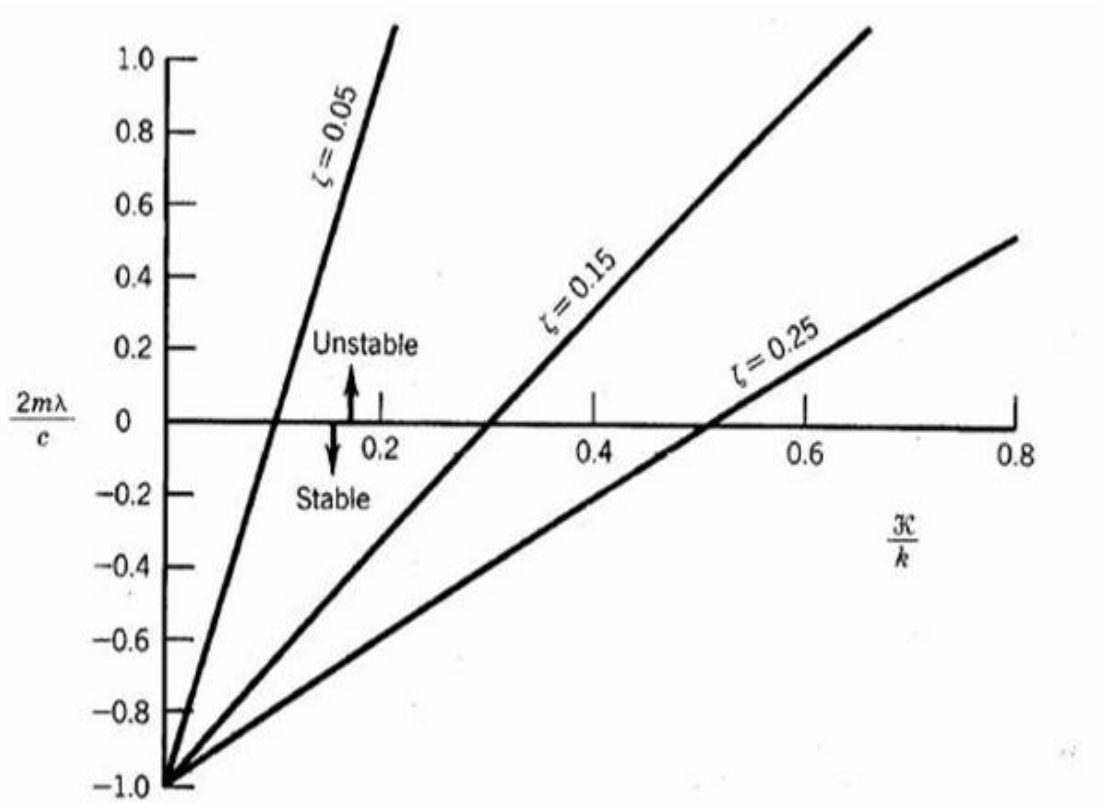

Fig 2: Effect of cross-coupled stiffness on rotor stability. (From Vance [1])

where C (N-s/m) is the total damping present in the system, K (N/m) is the total modal stiffness, m (kg) is the modal mass and ω(rad/s) is the shaft operating speed. It can be seen that when $k_{xy} = -k_{yx}$, the stiffness matrix becomes skew symmetric. This causes a couple that drives the rotor in the+ forward whirl direction for any instantaneous displacement, thus effectively destabilizing the rotor. In practicality, destabilizing cross-coupled stiffness can be caused by fixed arc journal bearings, seals and fluid forces around impellers. The solution to the Jeffcott model, resolved in amplitude (r) and phase (β) is given as:

$$|r| = \left|\sqrt{x^2 + y^2}\right| = \frac{m\omega^2 u}{\left(k - m\omega^2\right)^2 + \left(\omega c - \kappa\right)^2}$$

$$\beta = \tan^{-1}\left(\frac{\omega c - \kappa}{k - m\omega^2}\right)$$

It can be seen that cross-coupling κ can have an effect on the phase angle. It is therefore worthwhile to study the change in phase and thereby determine if the system is stable or not.

In all, four rotors were analyzed. The four rotors studied were chosen such that two were actual compressor rotors on tilt-pad bearings that went unstable and the remaining two were rotors in the Turbomachinery Laboratory, Texas A&M University, that ran on ball-bearings and had little or no external damping. The two 'real-world' rotors that were analyzed were the Ekofisk Compressor Rotor and Chevron's Kaybob Compressor Rotor, and two ball-bearing rotors were the Swirl Inducer Rig and Shell Two-disc Internal Friction Test Rig.

In all the cases analyzed except the Internal Friction test rig, the instability was induced by increasing the cross-coupling stiffness value of the rotor until the damping constant went negative. The cross coupling stiffness values were kept constant at all speeds. In the case of the Internal Friction Test Rig, the cross coupled moments were arbitrarily increased until instability was induced.

It should also be mentioned here that cross-coupled stiffness coefficients from the best available labyrinth seal codes were input into the rotordynamics model of the compressors and were found to be inadequate in predicting the observed instability. This may indicate that the cross-coupled forces were generated from different sources to

ultimately drive the compressors unstable, or that the labyrinth seal codes are inadequate. The detailed analysis using the labyrinth seal code from XLTRC^2 is shown in Appendix I and Appendix II for the Ekofisk and Kaybob compressors respectively.

Swirl Inducer Test Rig

Kar and Vance [17] present experimental data from a test rig rotor with a swirl Inducer - first when it is running in a stable manner and then, when it is intentionally driven unstable. They compare the phase at a speed equal to twice the first critical speed and report a change of 7.3^0. However, they recommend comparing the phase at the critical speed, where the change in phase should be more pronounced. A computer simulation of the swirl Inducer test rig rotor is conducted to verify if there is any prominent change in phase at the critical speed.

Fig 3 shows the general arrangement of the test rig. The rotor is mounted on ball bearings constrained at the inner race by a non-rotating cantilevered steel support rod. Pressurized air drives the air-turbine up to a maximum speed of 6000 rpm. The swirl inducer housing has nozzles arranged around the periphery of the rotor to induce air swirl when pressurized. The air swirl is in the direction of rotor rotation and generates whirl instability from destabilizing cross coupled stiffness above the first critical speed (2100 rpm). Two calibrated orthogonally mounted eddy current proximity probes are used to capture vibration data from the rotor. Another proximity probe was used to read tachometer pulses from a notch on the rotor surface. A recently developed data acquisition system was used to collect and analyze the experimental data.

Fig 4 shows a computer model of the rotor. The instability in the model is initiated by introducing cross-coupling at the swirl inducer location. The cross-coupled stiffness values are increased gradually, till the rotor becomes unstable. The phase angle vs. speed plots at the left bearing, right bearing and shaft mid-span is shown in Fig 5, Fig 6 and Fig 7 respectively.

As is evident from the simulation, change in the synchronous phase angle at the critical speed can be used as a diagnostic indicator for instability.

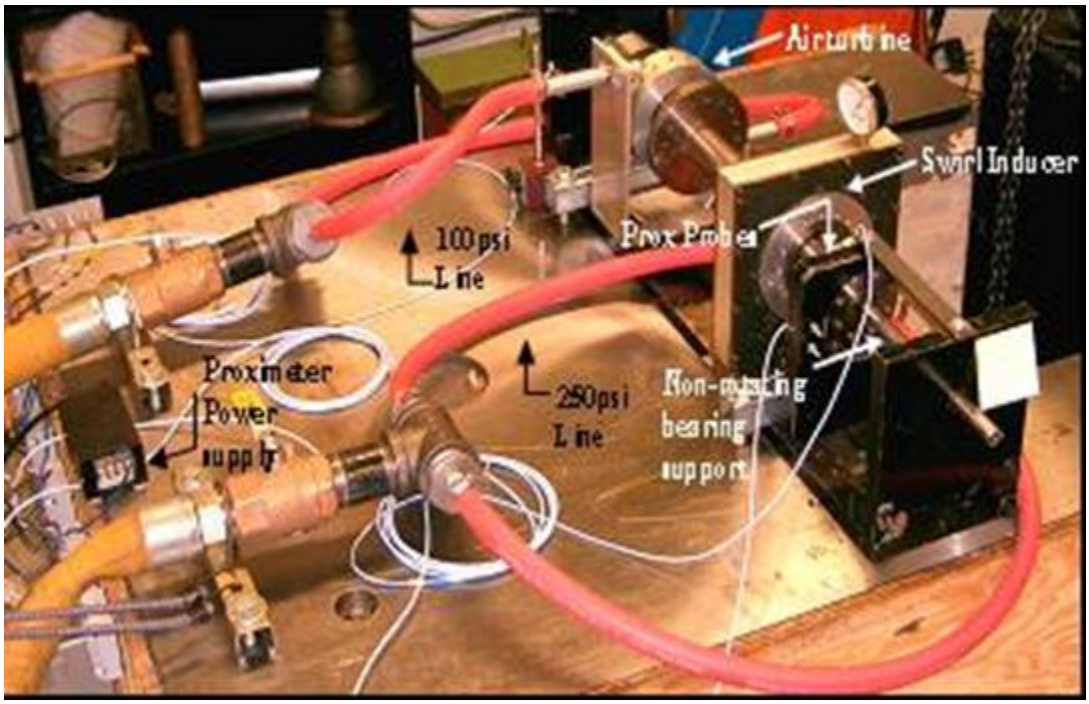

Fig 3: Swirl inducer test rig (Kar and Vance [17])

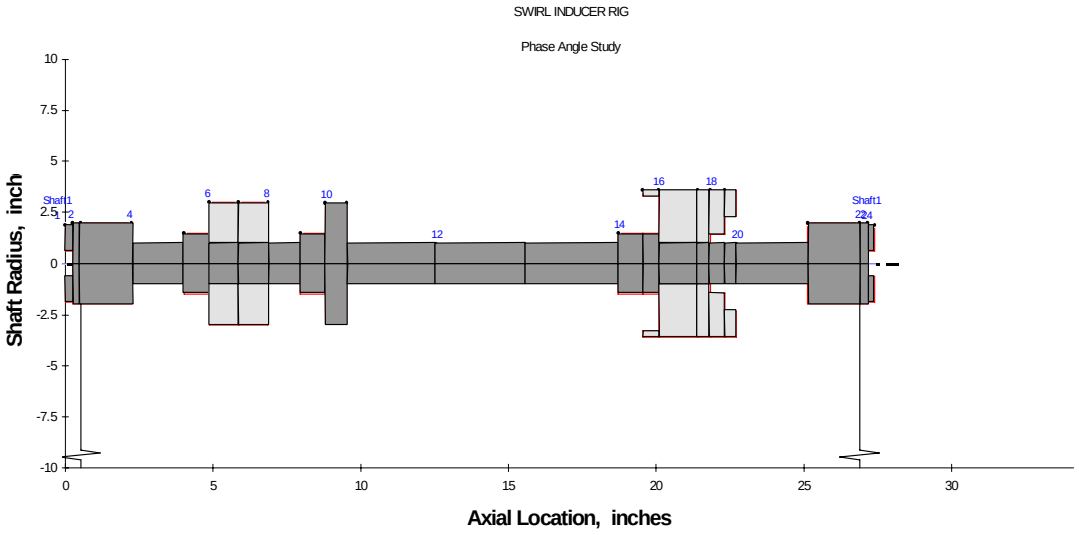

Fig 4: XLTRC^{2TM} model of swirl inducer rig

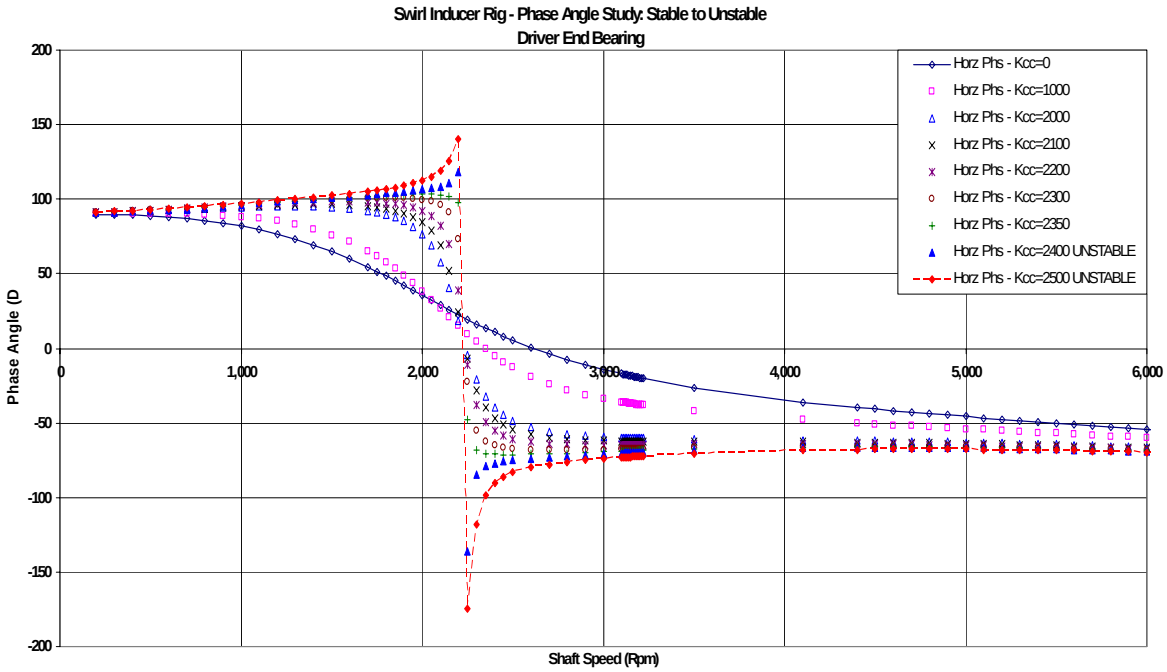

Fig 5: Chart showing phase angle change at the critical speed from stable to unstable at driver bearing location

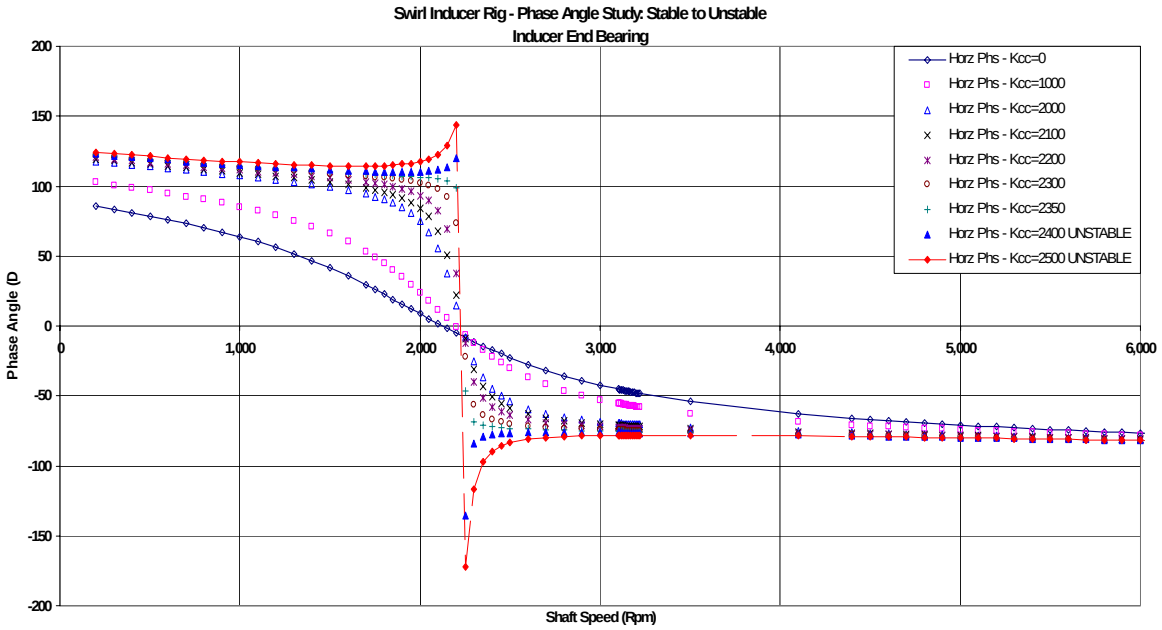

Fig 6: Chart showing phase angle change at the critical speed from stable to unstable at inducer bearing location

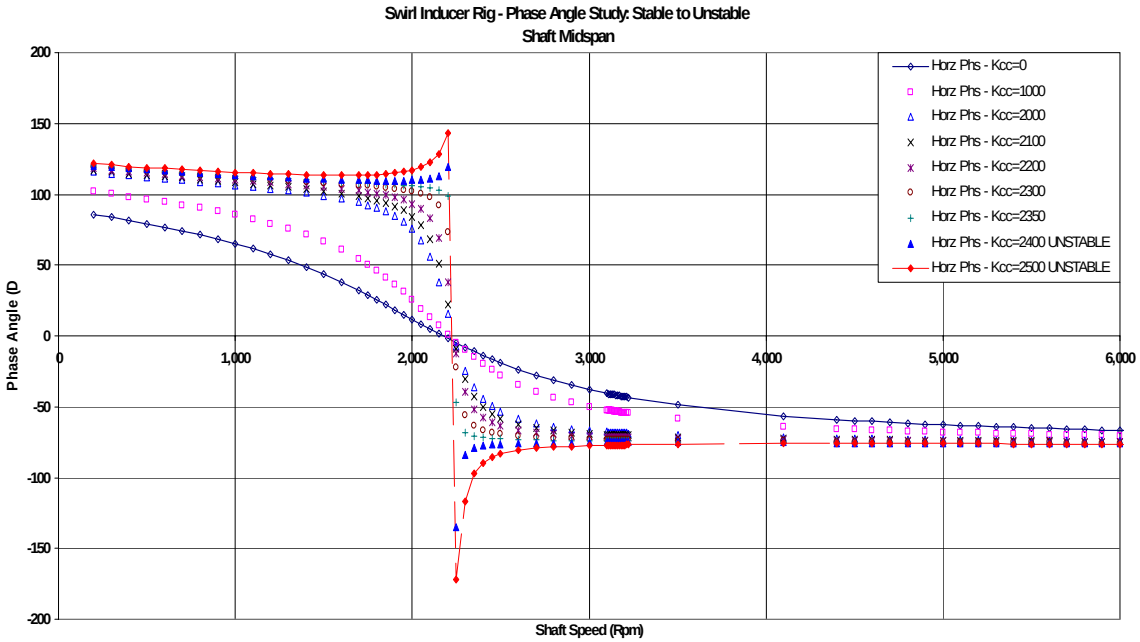

Fig 7: Chart showing phase angle change at the critical speed from stable to unstable at shaft midspan

Internal Friction Test Rig

The internal friction test rig rotor analyzed here has been used in the Turbomachinery Laboratory for a study of internal friction effects due to shrink fits in rotor assemblies. Jafri [18] details the theory of internal friction arising in rotors and driving whirl instability due to inadequate shrink fits and the experimental data to support it. Relevant portions from his work are presented here.

Fig 8 shows the test setup of the two-disk internal friction rotor. It consists of a 1.5in (38.1 mm) thick shaft mounted on ball bearings at a bearing span of 48in (1219.2 mm). The two disks are 9in (228.6 mm) each in diameter and 2in (50.8 mm) thick and are spaced at 18in (457.2 mm) about the shaft mid-span. An aluminum sleeve, 0.5in (12.7 mm) in thickness, is mounted with an axial interference of 2in (50.8 mm) on one disc and 1in (25.4 mm) on the other. The rotor can be run to a maximum speed of 13,000 rpm with the first critical at 6700 rpm.

Fig 9 shows the rotordynamic model of the rotor. The foundation parameters have also been included in the model. The internal friction at the disc-sleeve interface has been modeled as cross-coupled moments. Fig 10 shows the phase change simulated, and Fig 11 shows actual test data. The test data was taken on the run down after the rotor went unstable at a shaft rotative speed of 9800 rpm.

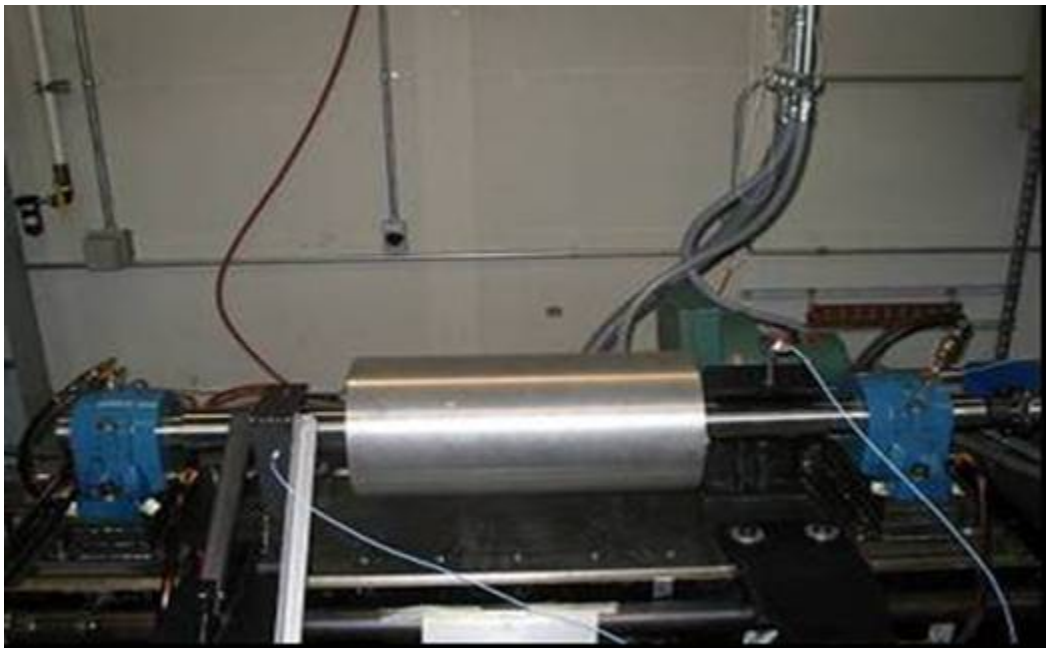

Fig 8: Two-disc internal friction rotor test set-up, Jafri [18]

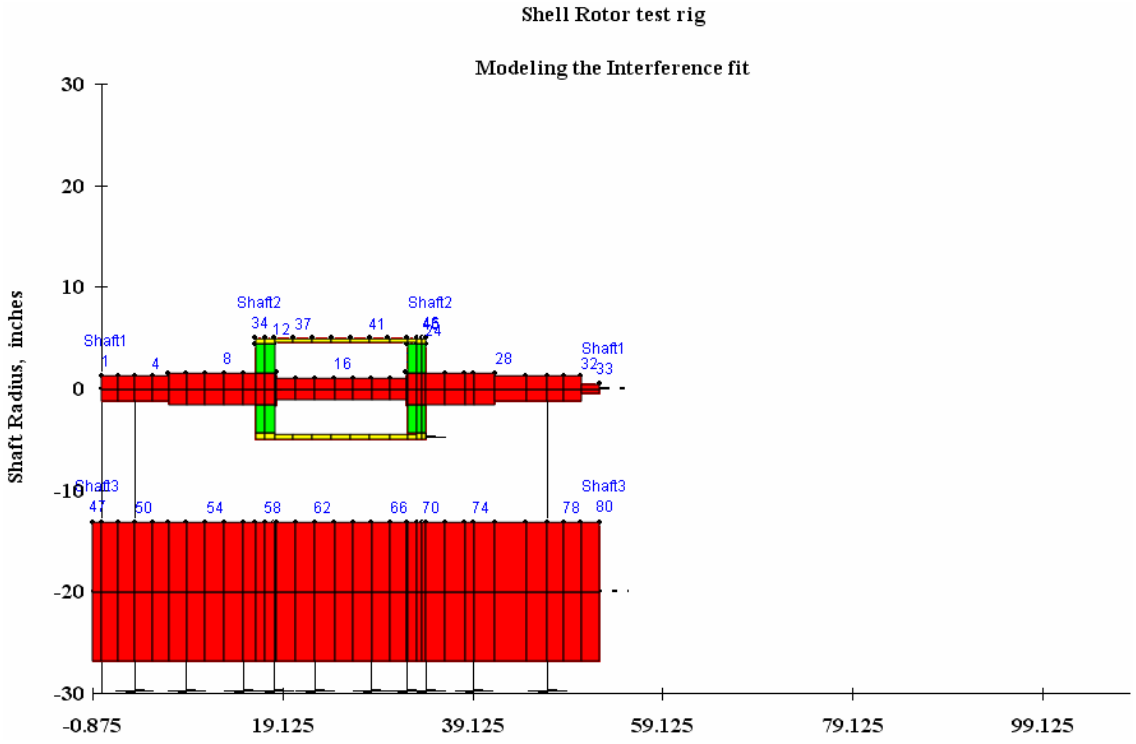

Fig 9: XLTRC^{2TM} model of two-disc internal friction rotor, Jafri [18]

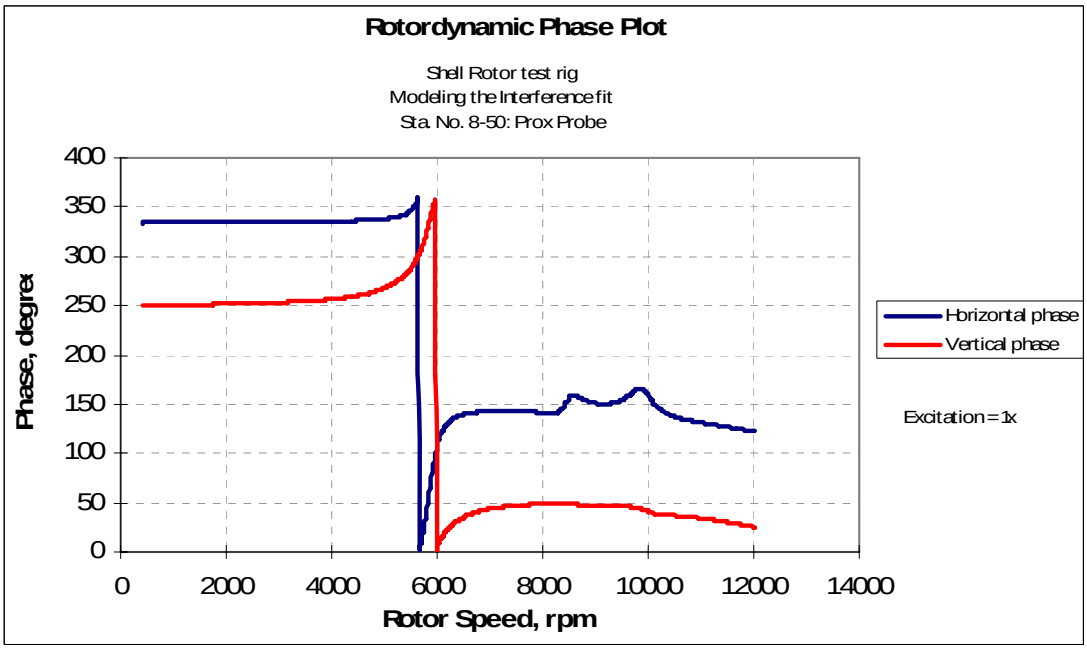

Fig 10: Chart showing phase angle change at proximity probe location of shaft

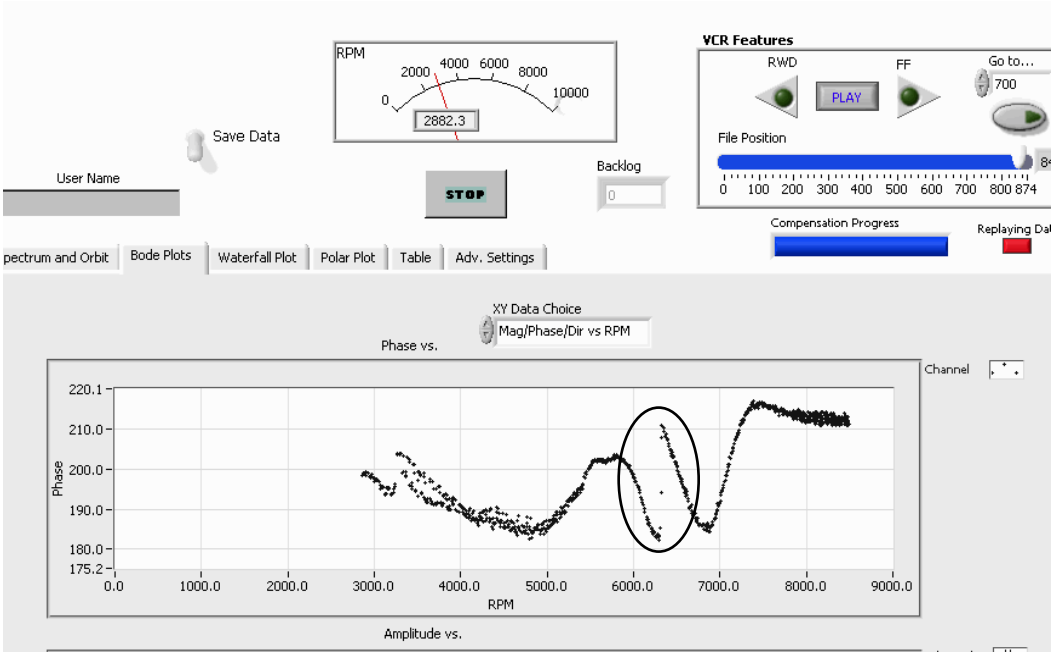

Fig 11: Phase angle vs. speed in experimental test run

Ekofisk Compressor

The Ekofisk Compressor instability problem, along with Chevron's Kaybob Compressor, are probably the most infamous of compressor instabilities - one of the main reasons being the huge financial losses incurred with each passing day of inoperation of the compressor. Doyle [11] and Wachel [12] give a detailed account of the problem. The Ekofisk Compressor was a gas reinjection compressor installed by the Phillips Petroleum Norway Group in the Ekofisk Oil Field off the Norwegian Sector of the North Sea. The 22,000 horsepower, eight stage compressor with back-to-back impellers was rated at 8500 rpm, had a design suction pressure of 3500 psi (24.1 MPa), and discharge pressure of 9200 psi (63.4 MPa). The calculated first critical speed of the rotor was 3800 cpm for a bearing span of 206 cm (81 inches).

The Ekofisk rotor was modeled in XLTRC^{2TM} Software and the geometric plot is shown in Fig 12. The total rotor length was 102.8in with a bearing span of 81.3in. The weight of the rotor was 1421 lb (645.9 kg). The first rigid support critical speed was calculated at 4500 rpm. This agrees closely with 3800 rpm documented by Wachel [12] as the first critical speed. Incorporating the aero cross-coupling at the wheels increased the first critical speed to almost 5000 rpm.

Wachel's formula (Wachel [12]) was used to calculate the aerodynamic cross-coupling, at each impeller, and the same was input into the model. The cross-coupling at the central labyrinth seal was varied from zero to the value at which the rotor became unstable. Bode Plots were plotted for each iteration, and the change in phase angle monitored. Finally the graph of Phase Angle vs. Shaft Speed was plotted for different values of cross-coupled stiffness and for three different locations on shaft, viz., shaft midspan and bearing locations. These plots are shown in Fig 13, Fig 15 and Fig 17. The phase angle plot obtained using XLLaby^{TM} labyrinth seal code for the rotordynamic analysis is also shown for the purpose of comparison. The instability was not predicted using the labyrinth seal code. Appendix I provides a detailed explanation of the rotordynamic analysis using the built-in codes in XLTRC^2. Using these codes, an effective damping of 1.7% is obtained at the critical speed. This explains the sharp change in phase angle (at the critical speed) shown in Fig 14, Fig 16 and Fig 18 for the bearing locations and shaft mid-span.

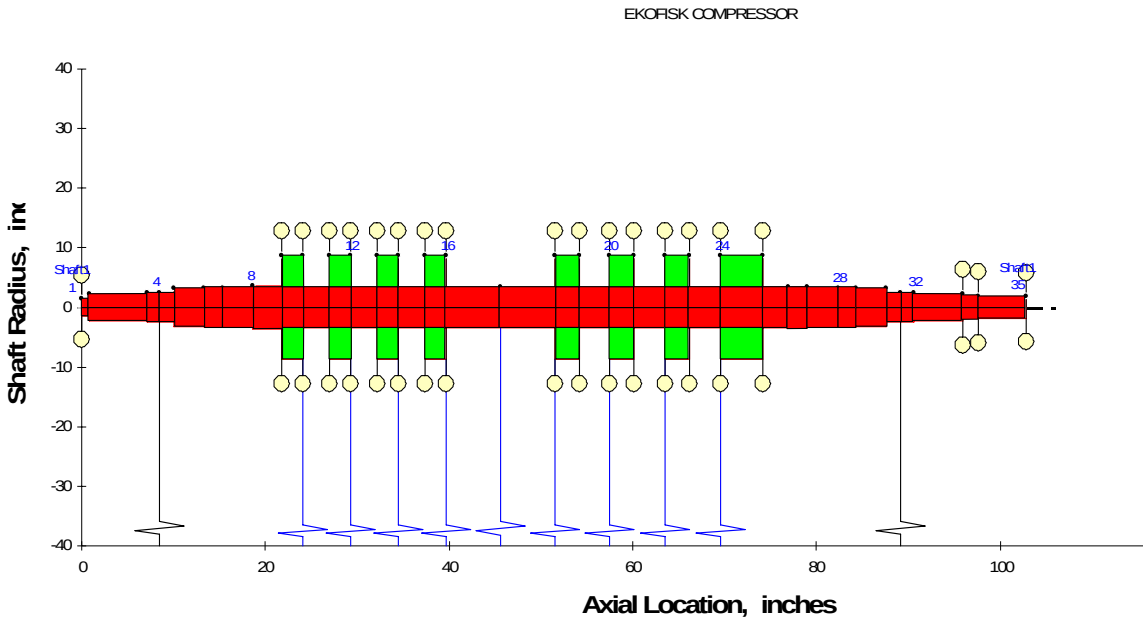

Fig 12: XLTRC^{2TM} model of Ekofisk compressor

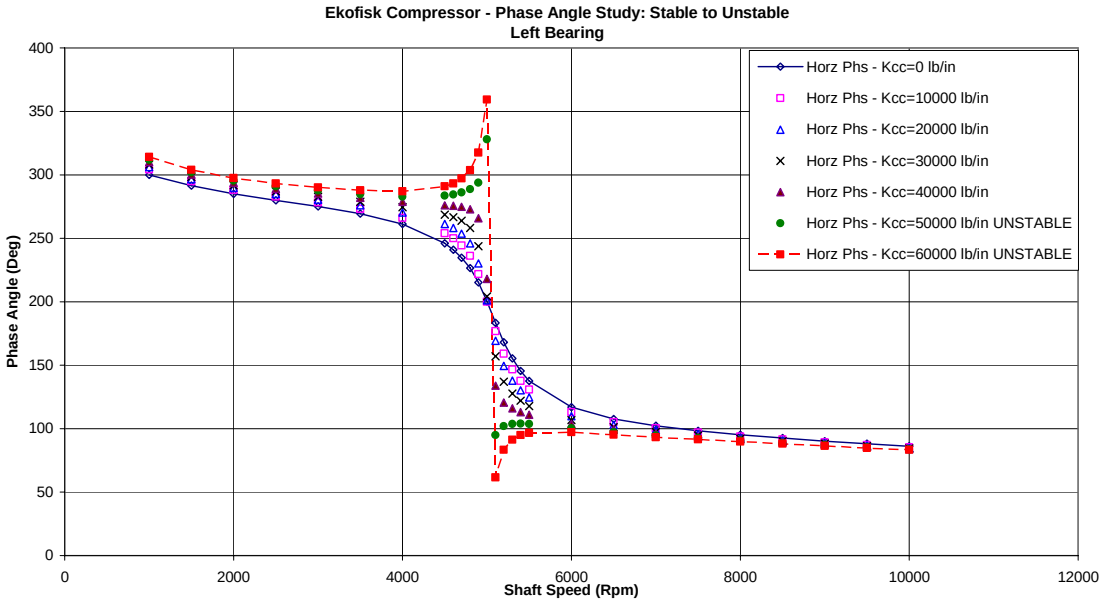

Fig 13: Chart showing phase angle change at the critical speed from stable to unstable at left bearing location

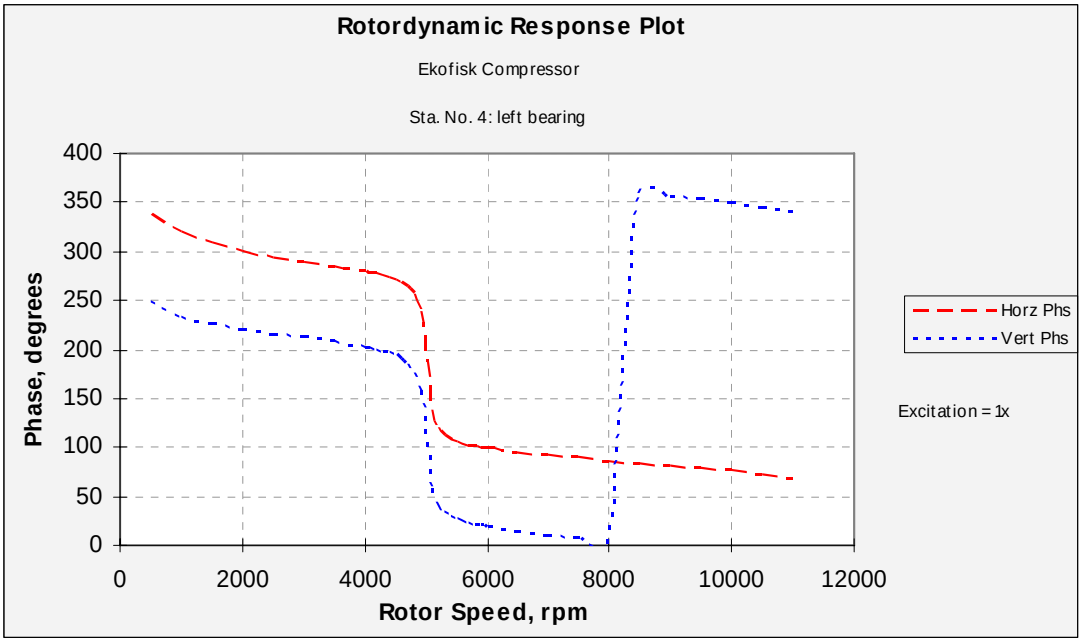

Fig 14: Phase angle plot at left bearing location obtained using XLLaby labyrinth seal code

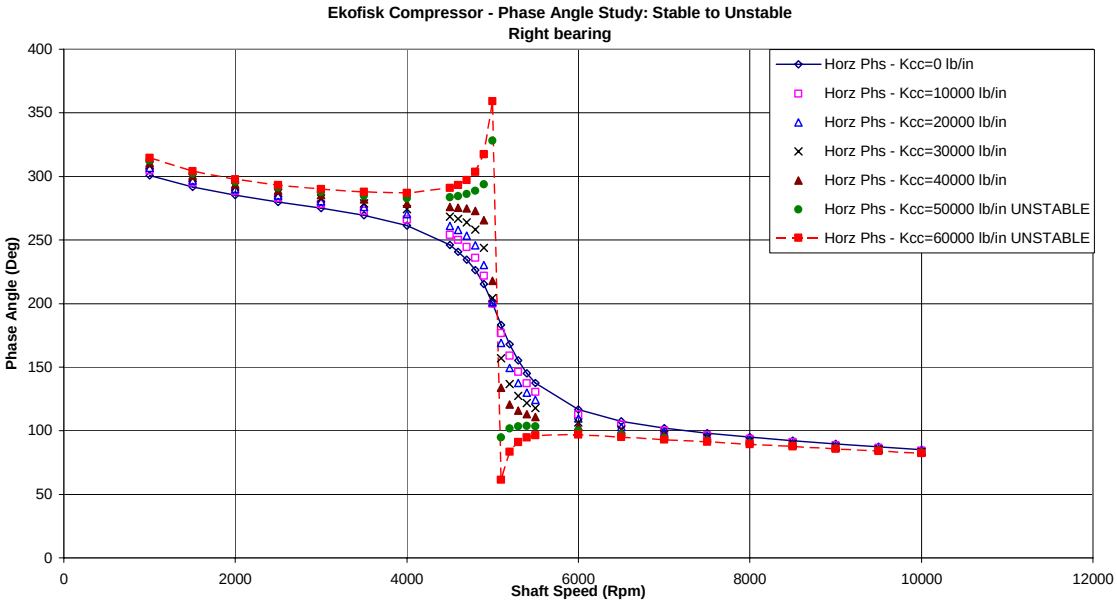

Fig 15: Chart showing phase angle change at the critical speed from stable to unstable at right bearing location

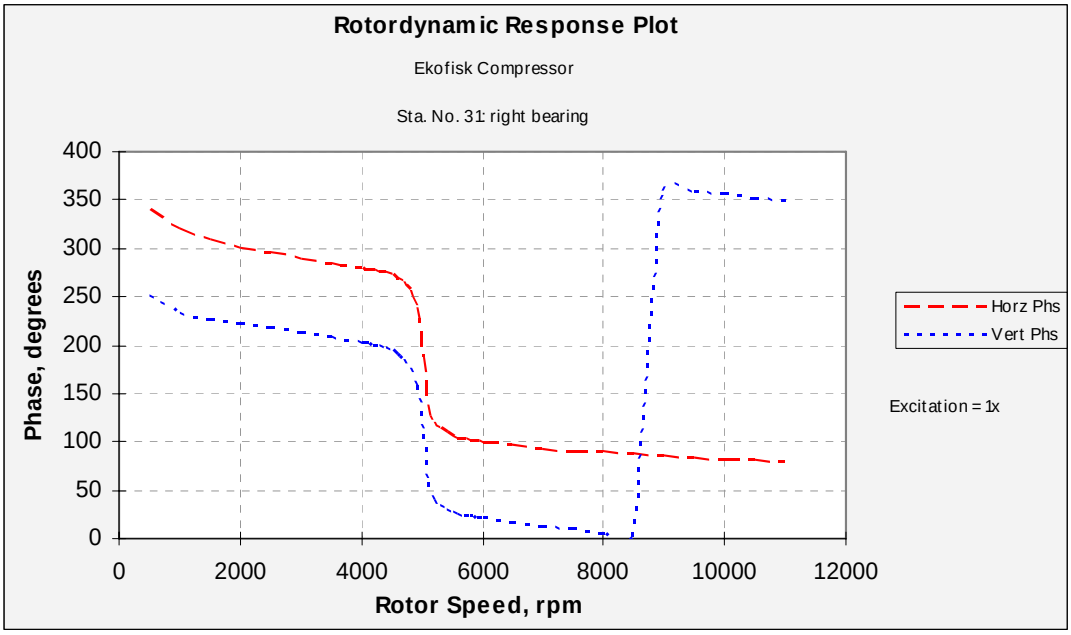

Fig 16: Phase angle plot at right bearing location obtained using XLLaby labyrinth seal code

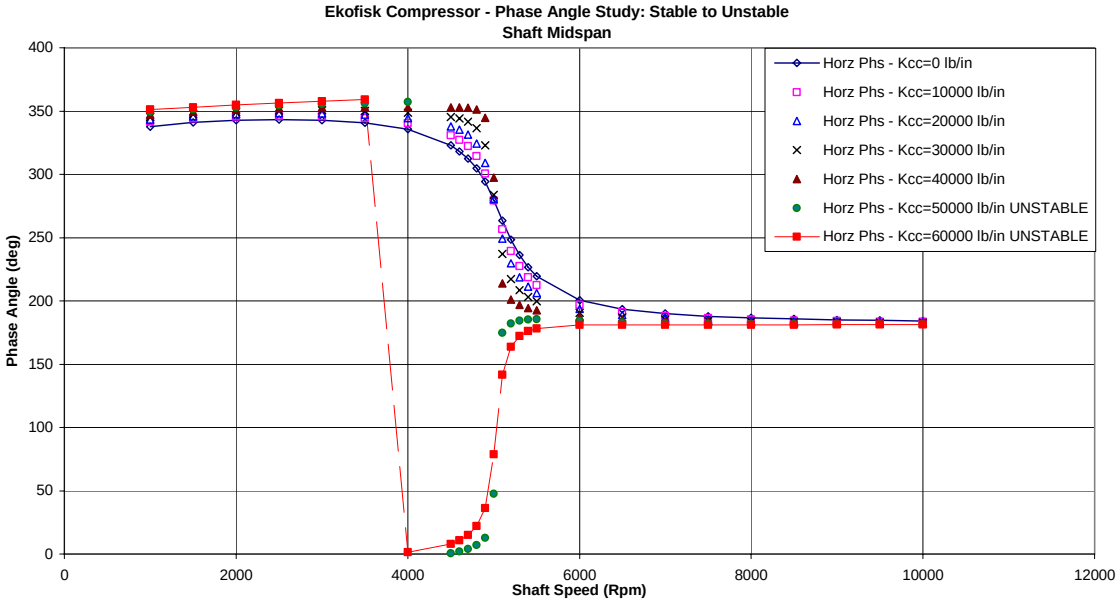

Fig 17: Chart showing phase angle change at the critical speed from stable to unstable at shaft mid-span

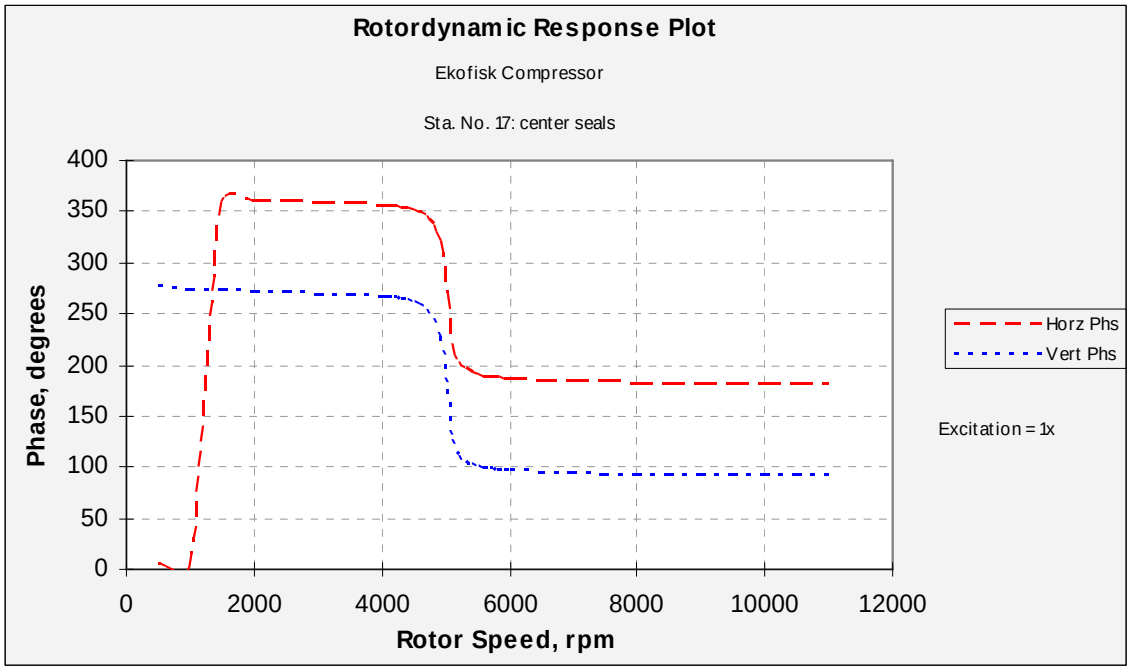

Fig 18: Phase angle plot code at shaft mid span obtained using XLLaby labyrinth seal

Kaybob Compressor

The Kaybob Compressor that infamously went unstable was one of the three gas re-injection compressors at the Kaybob South Beaverhill Lake plant near Fox Creek, Alberta, Canada operated by Chevron-Standard. A detailed account of the problem, the solution path and the solution is given by Fowlie and Miles [2] and Smith [10].

Since an exact model was not available, the rotor model in the paper by Smith [10] was scanned and scaled uniformly such that the bearing span was 59-11/16in (1516 mm) as specified. 5-pad tilt pad bearing were chosen with Load-on-Pad configuration. Small adjustments were made to the wheels in terms of thickness and outer diameter and to the bearing pre-load to bring the undamped critical speed as close as possible to 3915 rpm, which was the calculated first undamped critical speed. The undamped critical

speed for the simulation model was 3890 rpm. Further, the whirl amplitude at instability was 4577 rpm compared to the recorded 4350 rpm. The geometric plot of the rotor is shown in Fig 19.

Since no information was available on stage horsepower, densities of gases etc., aerodynamic cross-coupling effects were estimated. The cross-coupling at the centre labyrinth seal was increased till the rotor became unstable. At each increment of the labyrinth cross-coupling, the Bode plot was plotted and the change in phase angle recorded. A graph of Phase Angle vs. Shaft Speed was plotted for three locations on the shaft, viz,. shaft midspan and bearing locations, and the same is shown at Fig 20, Fig 22 and Fig 24.

The phase angle plot obtained using XLLaby^{TM} labyrinth seal code for the rotordynamic analysis is also shown for the purpose of comparison. The instability was not predicted using the labyrinth seal code. Appendix II provides a detailed explanation of the rotordynamic analysis using the built-in codes in XLTRC^2. Using these codes, an effective damping of 10% is obtained at the critical speed. This is a reasonably high damping value and explains the gradual and smooth change in phase angle (at the critical speed) shown in Fig 21, Fig 23 and Fig 25 for the bearing locations and shaft mid-span.

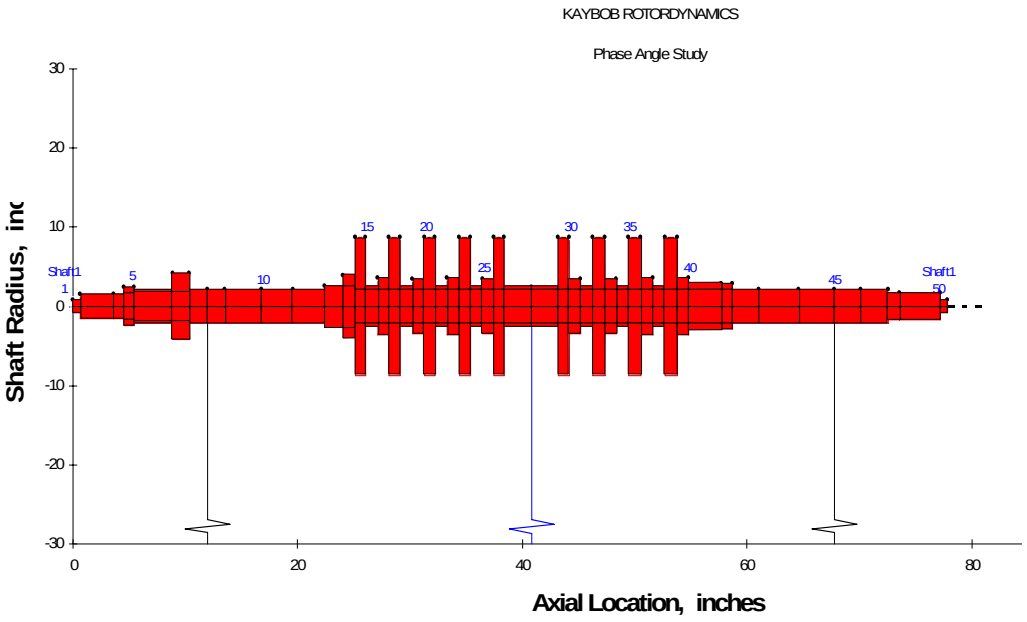

Fig 19: XLTRC^{2TM} model of Kaybob compressor

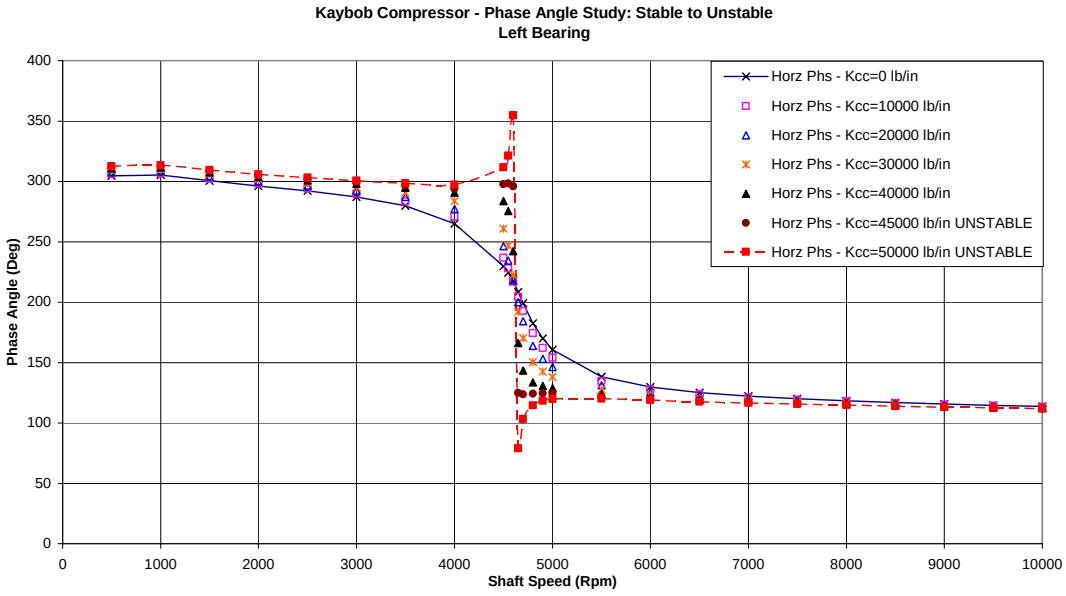

Fig 20: Chart showing phase angle change at the critical speed from stable to unstable at left bearing location

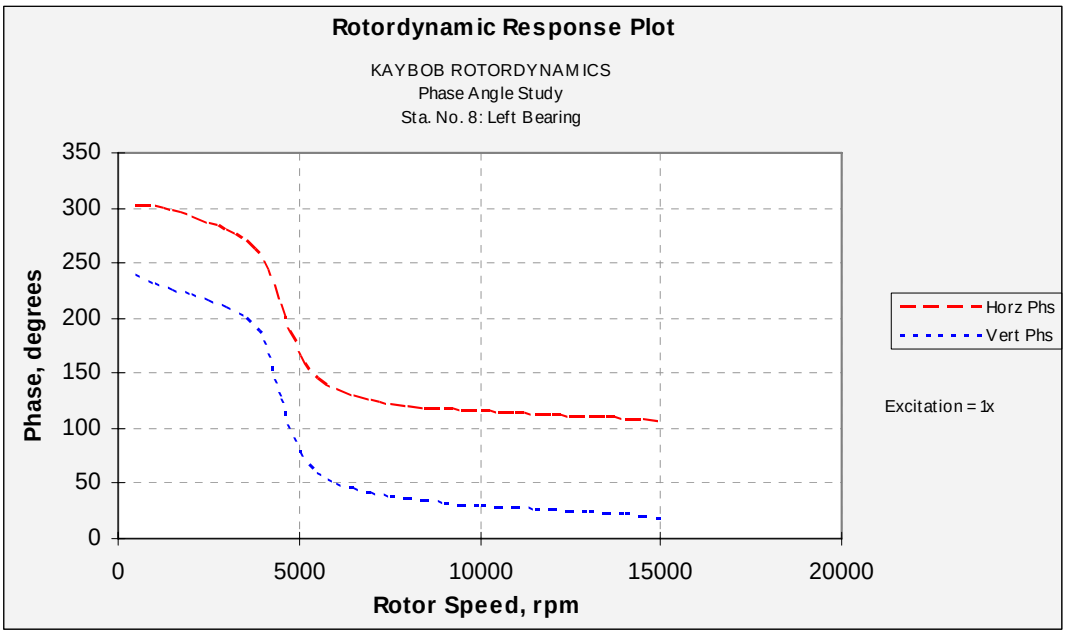

Fig 21: Phase angle plot at left bearing location obtained using XLLaby labyrinth seal code

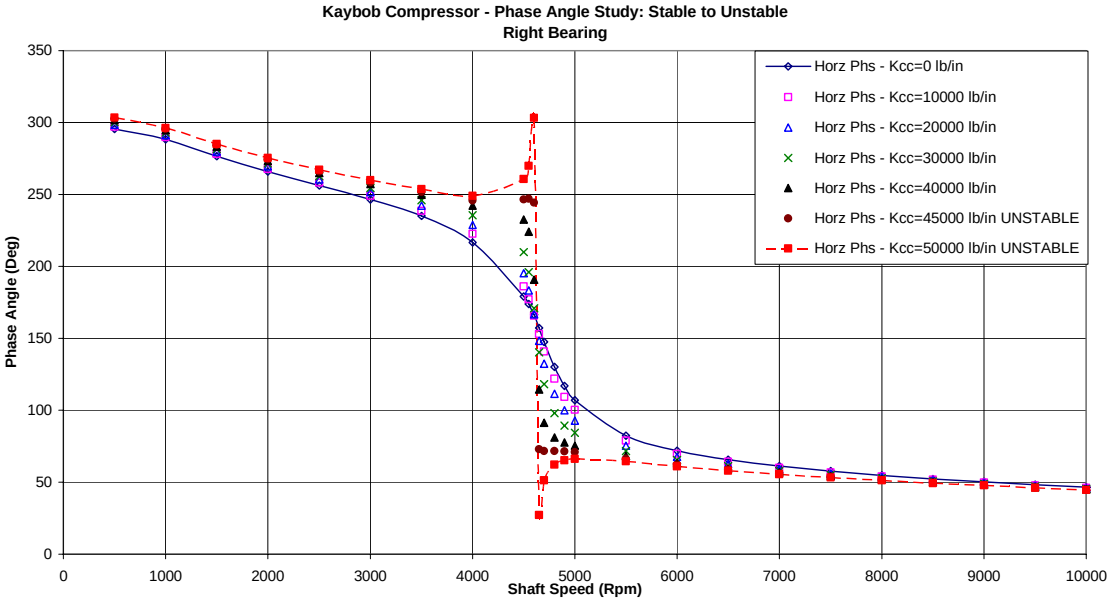

Fig 22: Chart showing phase angle change at the critical speed from stable to unstable at right bearing location

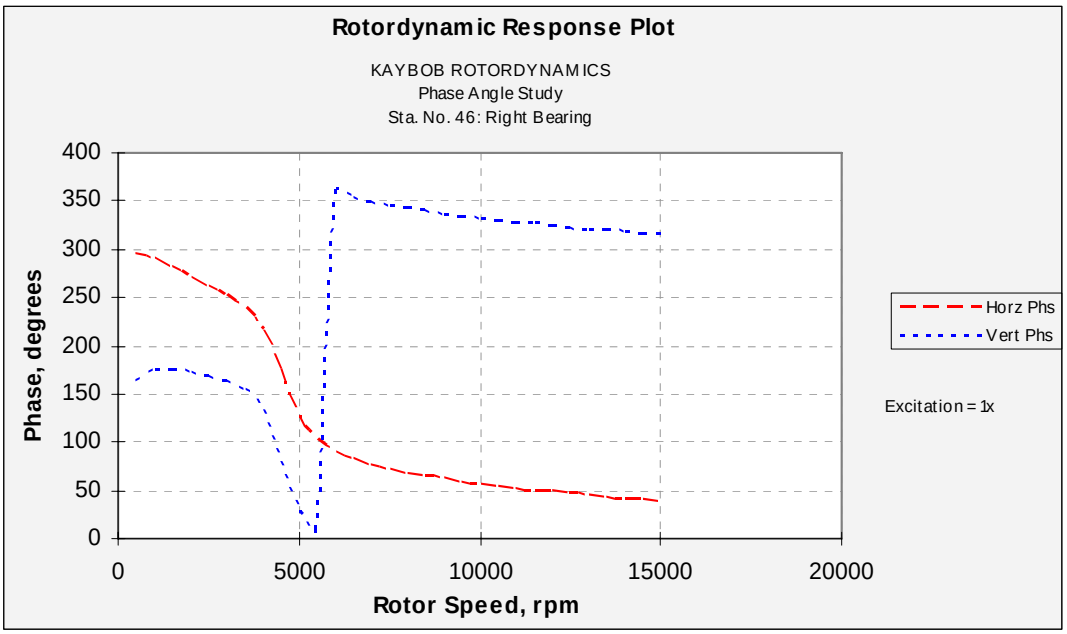

Fig 23: Phase angle plot at right bearing location obtained using XLLaby labyrinth seal code

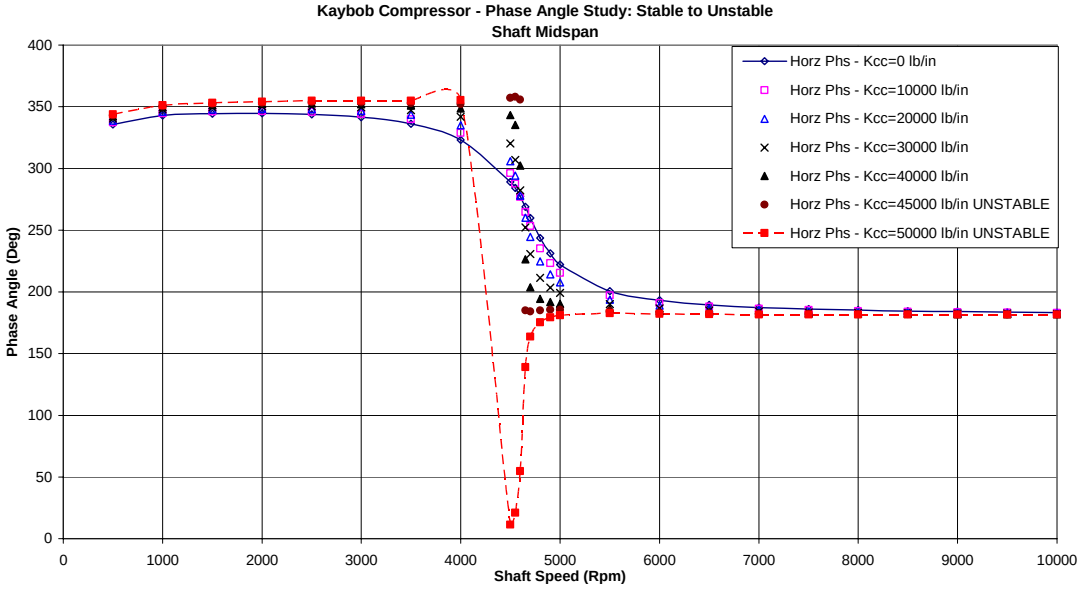

Fig 24: Chart showing phase angle change at the critical speed from stable to unstable at shaft mid-span

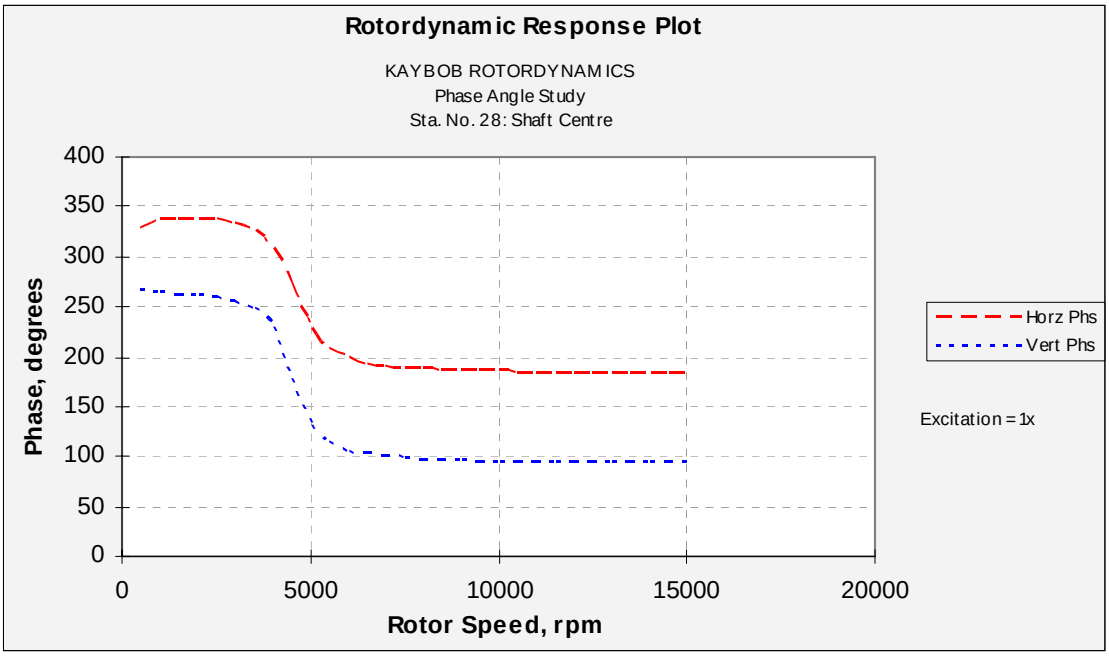

Fig 25: Phase angle plot at shaft mid span obtained using XLLaby labyrinth seal code

It can be seen easily from the simulations of the rotors done above that the phase angle changes in an abrupt and definitive manner near the critical speed as the system approaches instability. There is no clear 180^0 transition through the critical speed. Further, this change can be measured practically at any point along the length of the rotor. This result is only seen in the cases where the cross-coupled stiffness was assumed constant over the entire speed range. The rotordynamic analysis conducted using the XLLaby^{TM} labyrinth seal code did not predict instability. However, in the case of the Ekofisk Compressor, the phase angle change at the critical speed was rapid - a result similar to the one obtained assuming constant cross-coupled stiffness, just before the rotor went unstable. In the case of the Kaybob compressor, the labyrinth seal code was grossly inadequate in predicting the instability and therefore shows a gradual and smooth

change in the phase angle through the critical speed. Since actual phase angle data for these compressors is not available in the literature, the conclusion of an abrupt change in phase angle at the critical speed is proposed as a possibility.

However, a phase angle change at the critical as shown in the charts above can be easily mistaken for a 'scale change' (change-over at 360^0) that can sometimes be caused by the data acquisition system used. This can be seen in the Ekofisk and Kaybob compressor cases. However, results from the Swirl Inducer Rig and the Internal Friction Test Rig show that this is not necessarily true always. If an instability-like signal is observed along with an abrupt phase change at the critical, a judicious approach is required to diagnose the vibration signature. It has to be kept in mind that merely observing the phase angle does not indicate the root cause of the subsynchronous vibration. It provides a definitive way to help confirm whether the instability-like signal is a benign signal or is a true instability. To determine the root cause of the subsynchronous signal and zero-in on the actual problem, it would probably be necessary to study the time charts, obit plots etc., and look for indicators described in this report and in Kar and Vance [17].

The above conclusions from the phase angle analysis was based on test results from rotors in the Turbomachinery Laboratory, Texas A&M University and applied to field compressors that went unstable. Actual phase angle data from these compressors is not available. The phase angle results can be true for instabilities arising from large cross-coupled forces from bearings, seals etc., and may not necessarily apply to thermal or rub based instabilities.

CHAPTER III

SIGNALS PRODUCED DUE TO REPEATED IMPACT FROM A LOOSE BEARING

Test Rig

Vibrations at the natural frequency can occur in super-critical rotors due to the bearing banging around in the dead-band clearance between the outer race and housing. Experiments were conducted to study the nature of these vibrations and determine if these subsynchronous vibrations can be identified.

The test rig was a modified Bently Rotor Kit shown in Fig 26. The Bentley Rotor Kit consists of a 2in (50.8 mm) diameter and 1in (25.4 mm) thick steel disk mounted on a slender shaft of diameter 0.38in (9.65 mm) and 23in (584.2 mm) long. The shaft is supported on two ball bearings at each end with a bearing span of 22in (558.8 mm). It is driven by a 0.1hp (0.0735 kW) electric motor through a flexible rubber coupling. The speed of the motor could be controlled from 0 – 10,000 rpm (max) by turning a knob on the motor controller. The first natural frequency is at 25Hz as verified by rap tests, and the calculated second critical is at 183.3 Hz and beyond the maximum operating speed of the rotor. A dead – band clearance of 2 mils (0.05 mm) was intentionally machined between the bearing and the housing. A set screw in the housing was used to eliminate the clearance (in the tightened position) whenever required. Two proximity probes – one in the horizontal axis and the other in the vertical axis were used to measure shaft motion. The output from the proximity probes were fed into a LVTRC Data Acquisition

System and analyzed in detail. The results shown are screenshots of the saved experimental data.

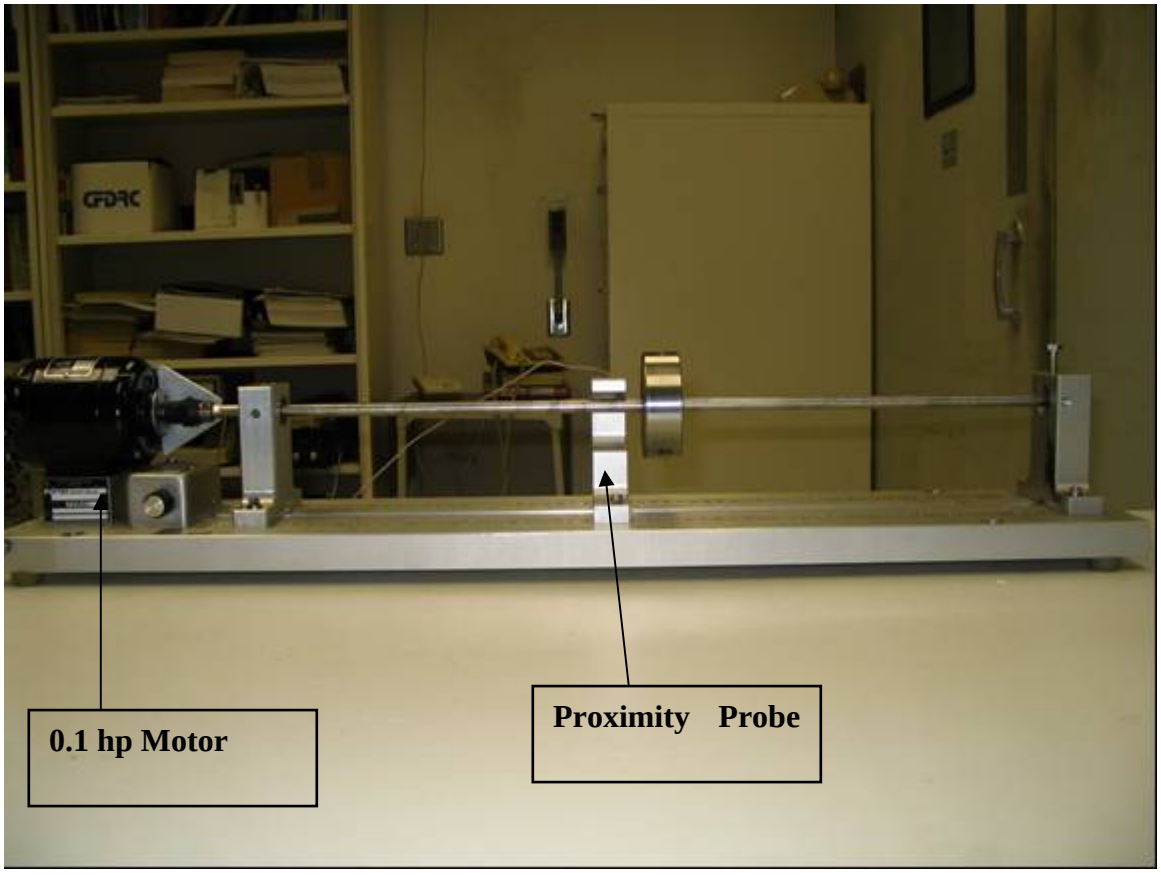

Fig 26: Bently rotor test kit

Rotor without Dead-band Clearance

Horizontal Arrangement

The rotor was first tested by tightening the bearing housing set screw so that the dead-band clearance was eliminated and the results are shown in Fig 27 and Fig 28. It

can be seen that there is no subsynchronous vibration. The experiment was repeated for different imbalance levels i.e. the rotor was tested in well balanced condition as well as not balanced at all, and there was no difference in the result. The rotor was run to its maximum operating speed of 10,000 rpm.

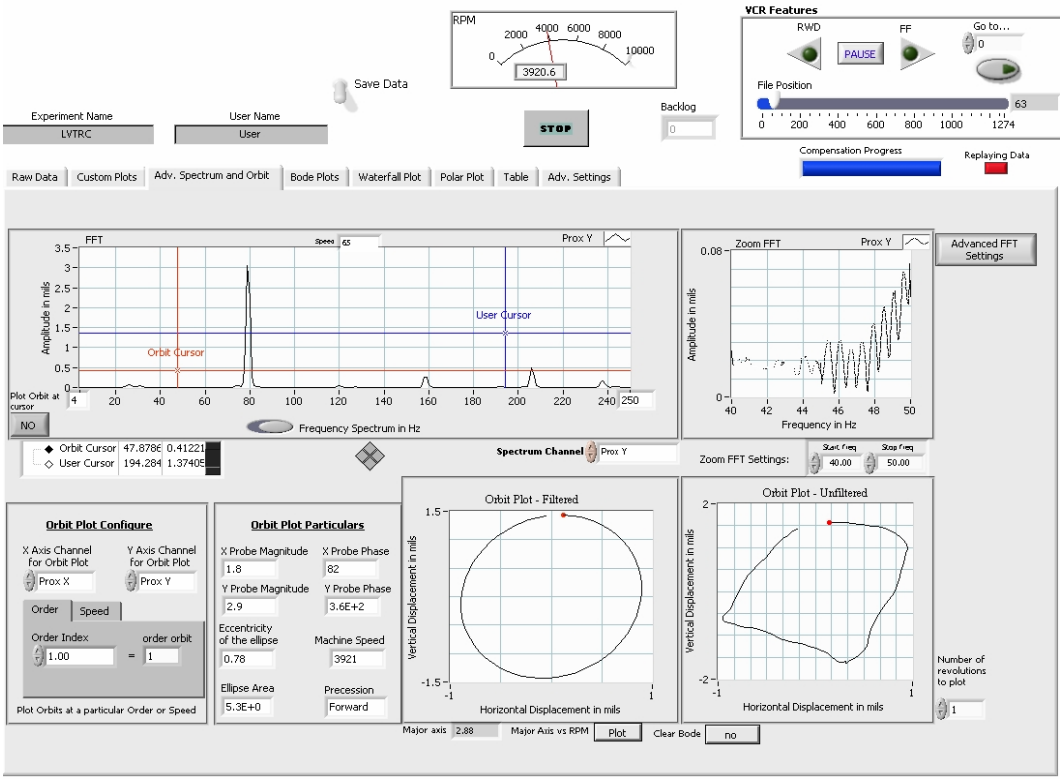

Fig 27: Horizontal arrangement baseline test frequency spectrum and orbit plot

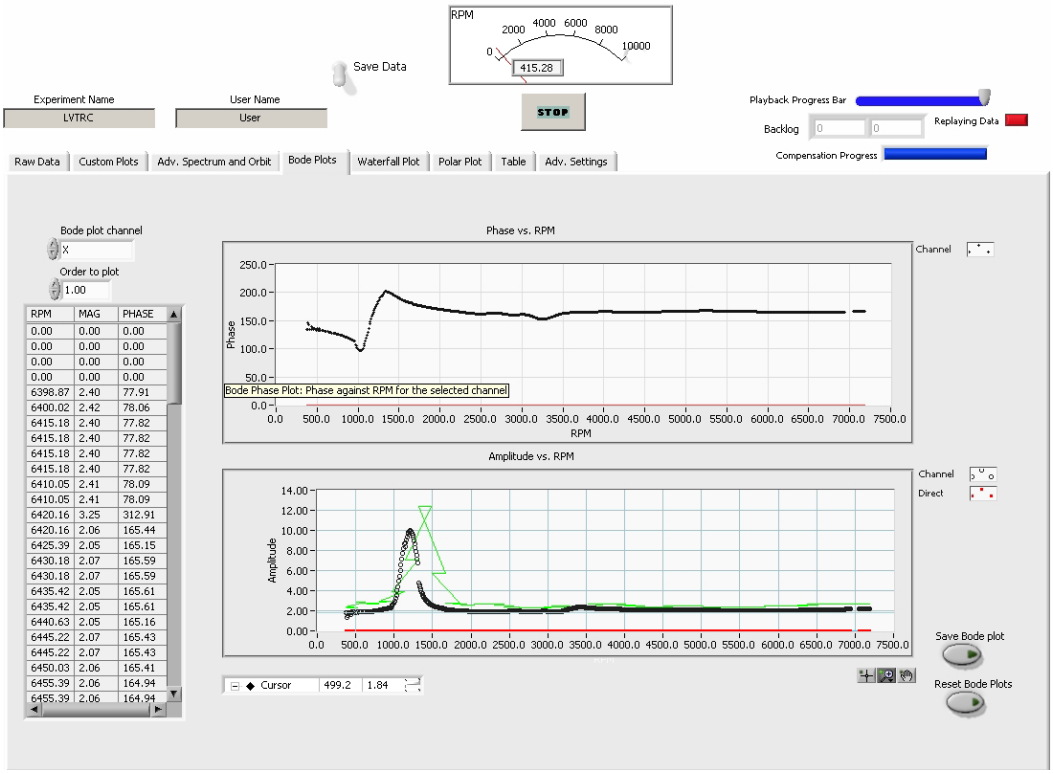

Fig 28: Horizontal arrangement baseline test Bode plot

Vertical Arrangement

The rotor kit was mounted vertically against a wooden support as shown in Fig 29. A level gauge was used to check the straightness and it was found to be within 1^0(least count on the level gauge). The rotor was run all the way to its maximum speed and no subsynchronous vibrations were observed in the entire speed range. The results are shown in Fig 30 and Fig 31.

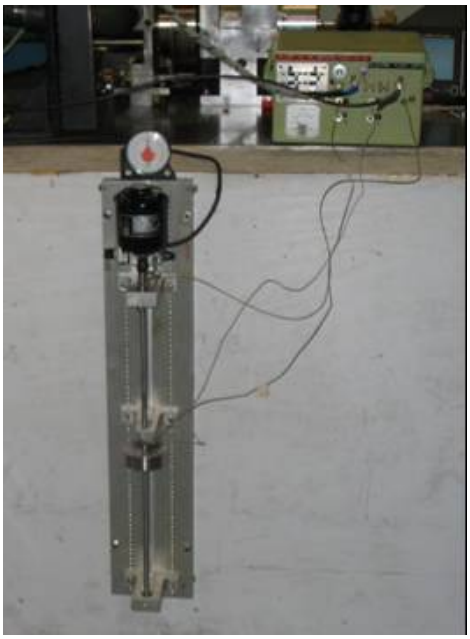

Fig 29: Vertically mounted Bently rotor kit

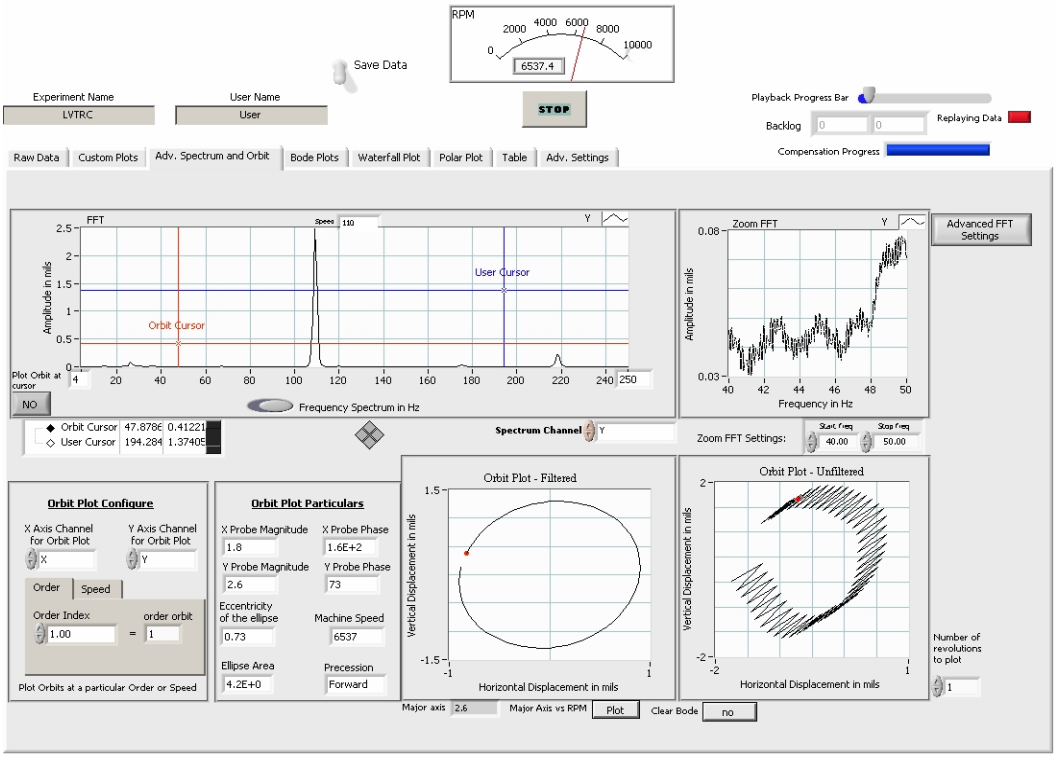

Fig 30: Frequency spectrum and orbit plot of vertical arrangement baseline test

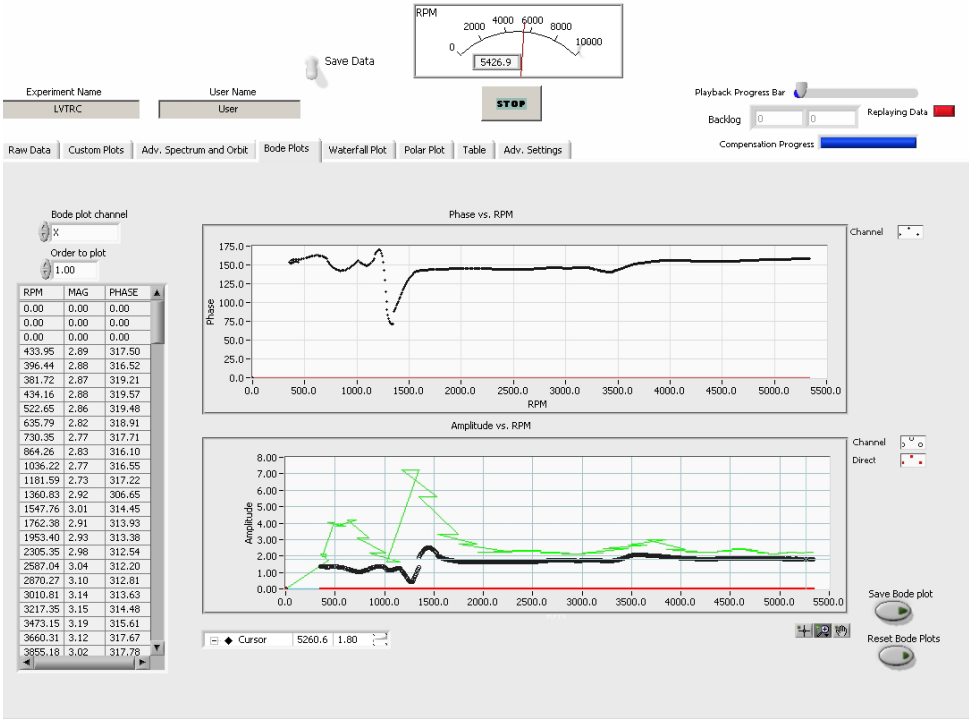

Fig 31: Bode plot of vertical arrangement baseline run

Rotor with Dead-band Clearance

Horizontal Arrangement

To introduce dead-band clearance, the set screw was loosened to an extent that the bearing outer race would never come into contact with it. The rotor ran smoothly at most speeds. However, there was a speed range between 60-75 Hz, termed as the "false instability" speed range, in which the rotor was likely to be disturbed and produced a large subsynchronous vibration at the natural frequency that often exceeded the synchronous response of the rotor. The subsynchronous frequency did not track the rotor running speed. Moreover, the subsynchronous response was a 'breathing' response by nature, i.e., the amplitude was constantly increasing and decreasing. Also, the response

was more likely to occur with a well balanced rotor than a rotor with large unbalance. Furthermore, squirting a few drops of oil into the clearance made the subsynchronous vibrations disappear. The synchronous phase angle was also observed during the experiment, and no change was observed from the baseline experiments with no dead-band clearance. The LVTRC test screen shot is shown in Fig 32.

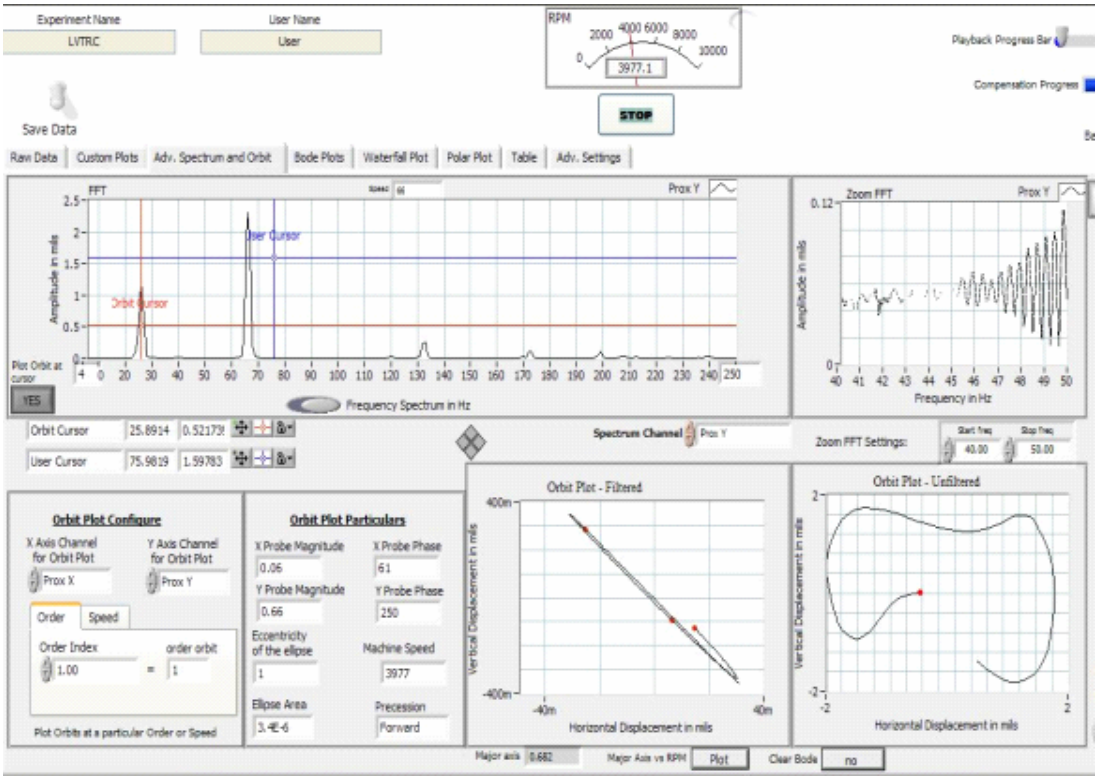

Fig 32: Frequency spectrum and orbit plot for vibrations from a loose bearing cap

Vertical Arrangement

The set screw in the bearing housing was loosened to introduce dead-band clearance. The response was smooth up to a speed of 100Hz. However a large

subsynchronous vibration at 20.5Hz was observed just beyond 100Hz and remained locked at that frequency till about 135Hz when the rotor had to be rundown because of excessive vibration. As in the horizontal configuration experiments, there was no tracking subsynchronous vibration observed. The LVTRC test screen shot is shown in Fig 33.

The variation in the results between the horizontal and vertical arrangements is immediately apparent. Whereas in the horizontal case the subsynchronous vibration was 'breathing' (fluctuating amplitude) in nature, the subsynchronous response is constant in the vertical arrangement case. There also seems to be a lowering of the natural frequency in the vertical case since the subsynchronous vibration occurs at 20.5 Hz. This is because the vertical arrangement was mounted against a wooden base as opposed to a solid steel base in the horizontal test arrangement. The lowering of the support stiffness probably reduced the natural frequency.

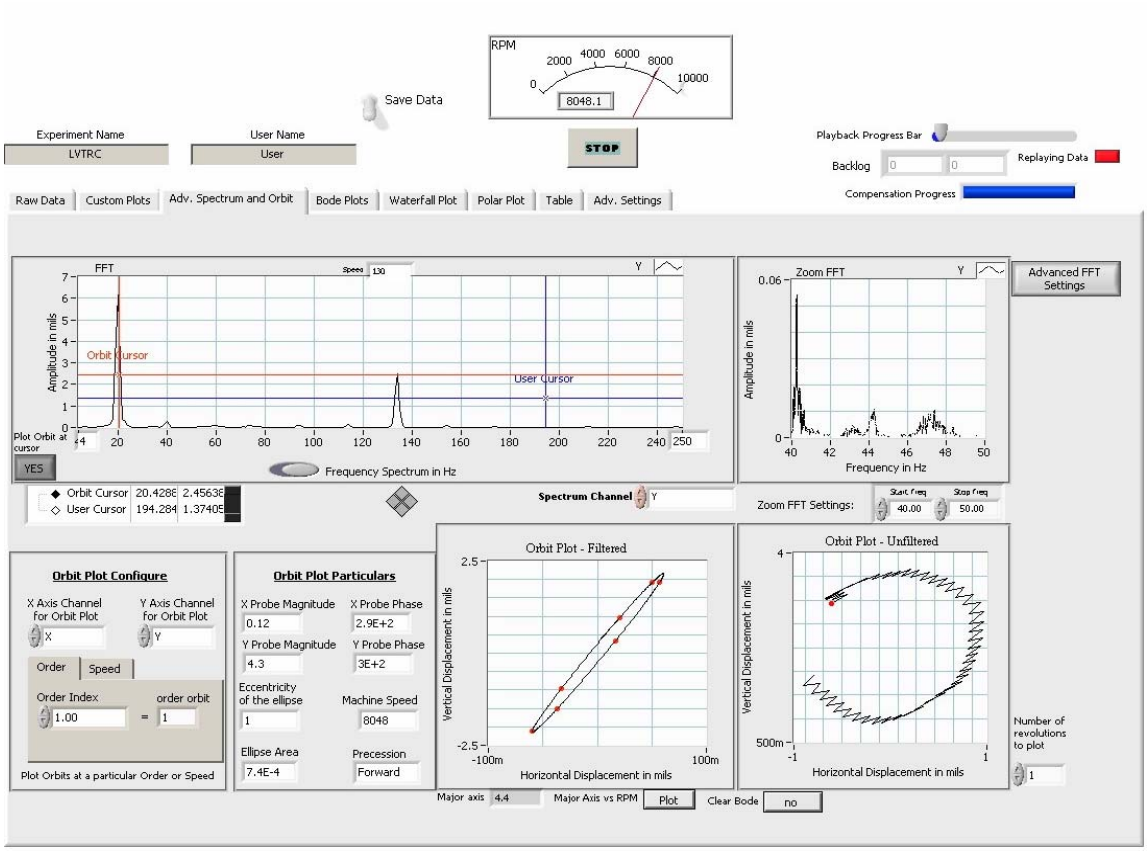

Fig 33: Frequency spectrum showing subsynchronous vibration from bearings dead-band effect at 8048 rpm

Also, the "false instability" speed range shifted from 60-75 Hz to beyond 100Hz. At this point, it can be only explained as a change in the operating condition of the rotor that changed the instability speed range. The shift of the instability range however was consistent, i.e. once the rotor was shifted back to the horizontal position, the instability range became 60-75 Hz and vice-versa.

With the rotor in horizontal position, the occurrence of subsynchronous vibration seemed sensitive to rotor imbalance i.e., lesser the imbalance, higher was the chance of

seeing subsynchronous motion. In the vertical arrangement experiments, the occurrence of subsynchronous vibrations was less sensitive to the imbalance of the system.

The results from the above experiments are significantly different from the loose baring experiments conducted by Bently [14]. Whereas Bently [14] reports a speed dependent subsynchronous motion, the results obtained above show only non-tracking subsynchronous motion occurring at the first natural frequency of the rotor. Bently [14] also suggests balancing the rotor as one of the remedies for the problem. However, it was consistently observed in the above experiments that the subsynchronous vibration was more likely to occur with a well balanced rotor, more so with the rotor in horizontal configuration. The differences could be because of the bearing arrangement. The experiments in Bently [14] are conducted with the rotor supported on bushings oversized by 0.015in (0.381 mm), diametrically. The above experiments are conducted with the rotor supported on ball-bearings, with a 0.004in (0.1 mm) clearance between the outer race and the housing.

There was no change in the synchronous phase angle variation from the baseline experiments with no dead-band clearance. The subsynchronous orbits are extremely elliptical and almost planar in both the horizontal and vertical cases. It is very highly unlikely that they would go unstable with time, though they appear like instabilities.

CHAPTER IV

ROTOR-STATOR RUBS

Introduction

Rotor to stator rubs in turbomachines are often encountered in the blade- shroud or journal-seal locations. They are usually secondary effect phenomena and occur as a result of high rotor imbalance, fluid forces, shock loads etc. The nature and extent of the rub determines the severity of the response as also the potential damage that can be caused. There can be a 'light or partial' rub where the rotor makes intermittent but brief contact with the stationery element. The contact forces are minimal and these do not usually threaten the integrity of the machine. The second case is the case of a full annular rub, which can lead to a catastrophic failure of the whole machine through a phenomenon called dry-whip. Jiang and Ulbrich [19] define dry-whip as a condition wherein the rotor is in continuous contact with the stator, slipping continuously on the contact surface and whirling backwards. In fact, this is the only source of instability (as will be shown later in this section) in which the rotor whirls backwards. All other sources of instability put energy into the system by driving the rotor forward, thus making it unstable. The rub phenomenon was studied experimentally in detail so as to identify a diagnostic indicator for this type of instability.

Test Rig

A modified version of the Bently Rotor Kit (described in Chapter II) is used for the annular rub experiments and is shown in Fig 34. A steel sleeve mounted inside a bracket, as shown in Fig 35, is placed just aft of the disc such that the shaft is concentric with the sleeve. The concentricity is adjusted by three bolts mounted on the bracket. A square piece supports the sleeve from the bottom. The aluminum sleeve has an outer diameter of 0.5in (12.7 mm) and inner diameter of 0.380in (9.652 mm). The shaft itself is 0.375in (9.525 mm) in diameter.

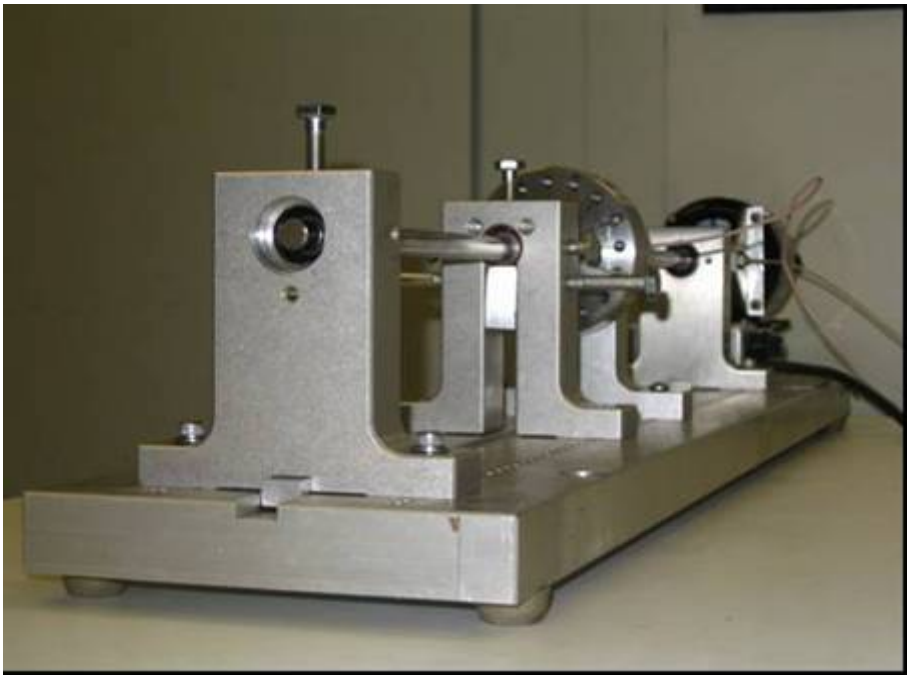

Fig 34: Modified Bently rotor kit for annular rub experiments

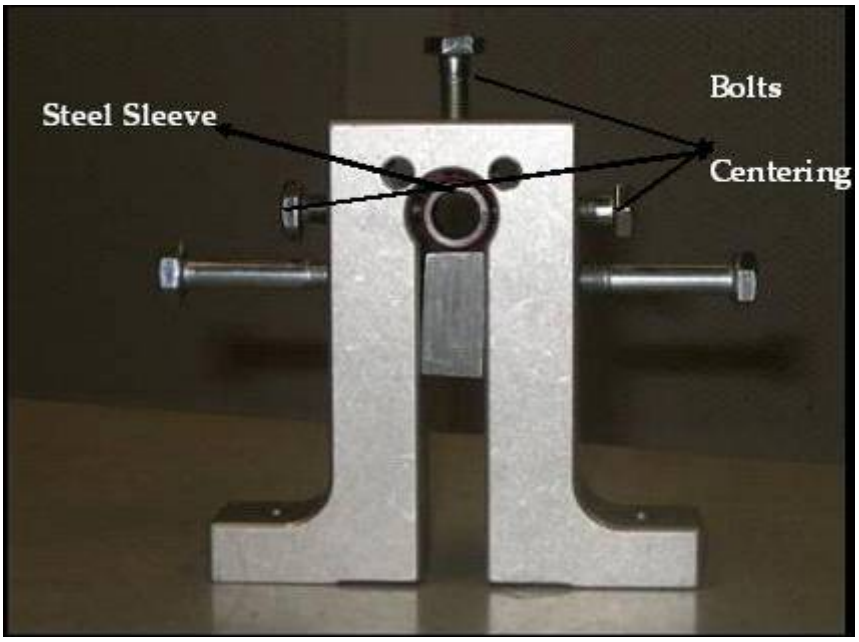

Fig 35: Bracket mounting sleeve

360^0 Annular Rub

The Bently Rotor Kit has a baseline critical of 1500 rpm. At low sub critical speeds (<500 rpm), a number of harmonics were excited around the first natural frequency region including the 2X and 3X response. The natural frequency orbit fluctuated between forward and backward whirl with backward whirl being the predominant mode. As the rotor pulled beyond the critical into the super critical region, dry friction whip became more and more prominent and the first natural frequency reverse precession response sometimes exceeded the synchronous response throwing the rotor into heavy vibrations. The rotor was run up to around 8500 rpm before it had to be rundown. The sub-critical and super-critical responses are shown in Fig 36 and Fig 31 respectively. The amplitude vs. time plot is shown in Fig 32.

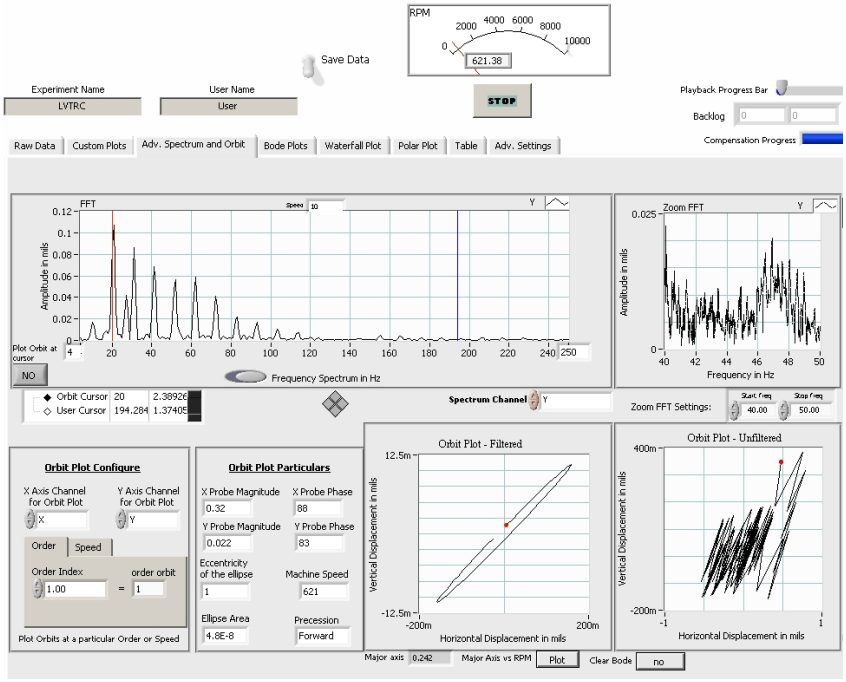

Fig 36: Rub response at subcritical speed

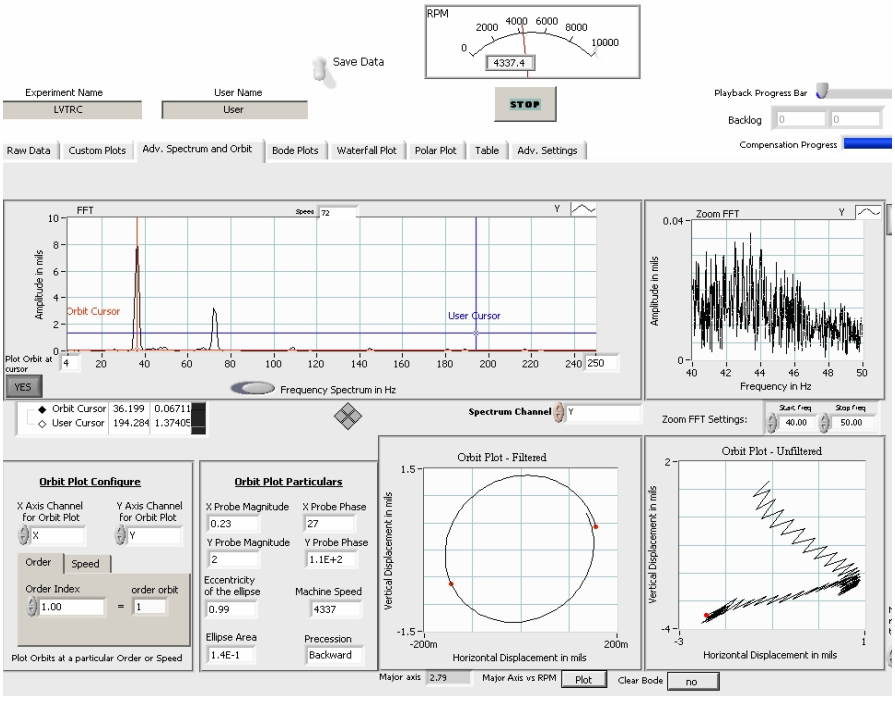

Fig 37: Rub response at 4337 rpm (super-critical speed)

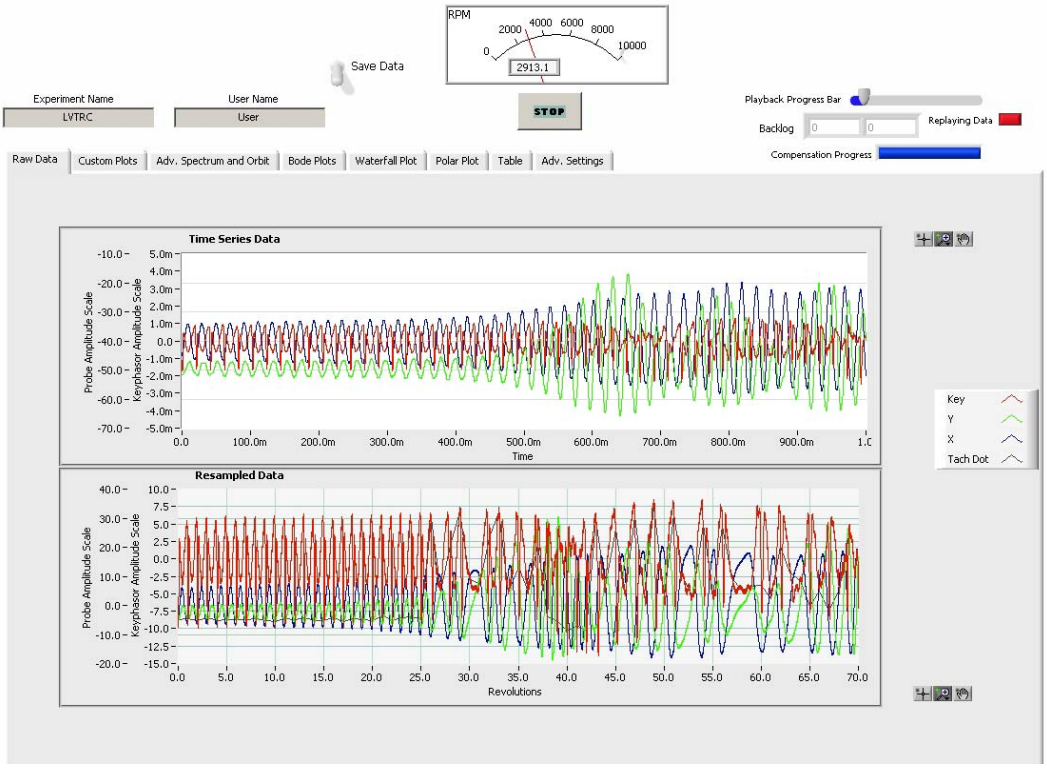

Fig 38: Time traces for rub response

During the rub, the natural frequency also increased because of the additional stiffness provided by the sleeve during the rub. Dry friction whirl was observed from 27 Hz to 38 Hz after which the frequency remained locked at 38 Hz.

The Bode plot for the baseline run and the full annular rub was plotted and this provided a further definitive indicator for annular rub. The first critical was shifted to the right of the baseline critical indicating an increased stiffness and a sudden 'jump down' was noticed as soon as the peak was reached and this was typical of very run conducted. The comparison is shown at Fig 39 below.

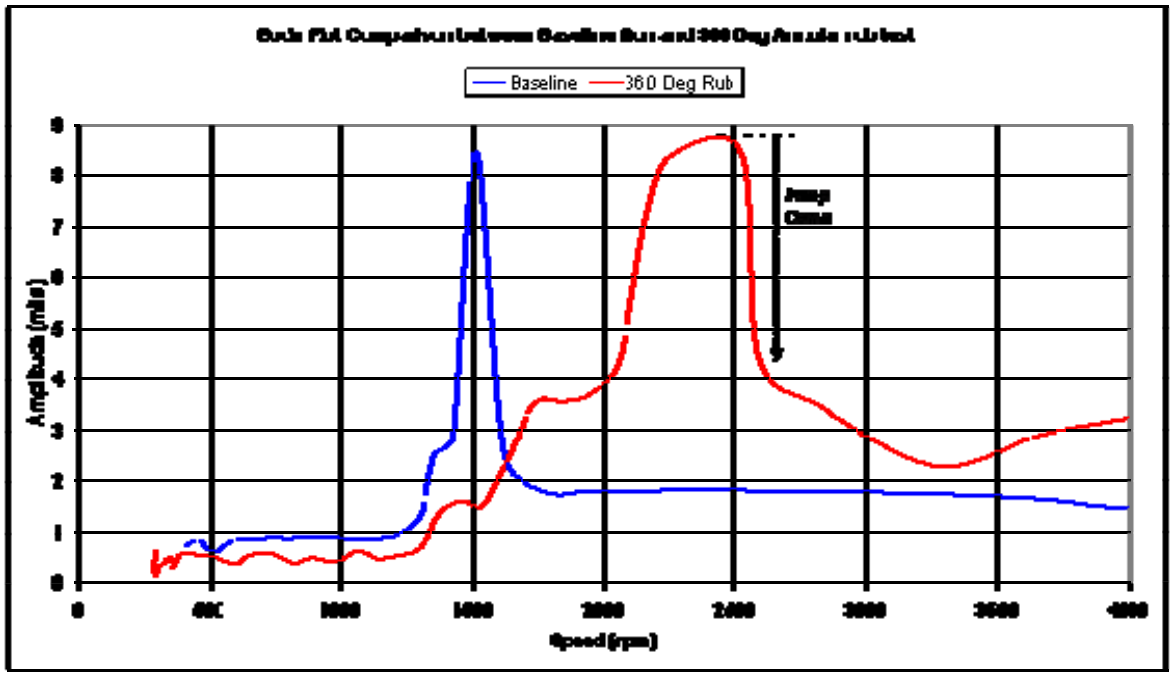

Fig 39: Chart comparing the bode plots of the baseline run and full annular rub test

For the dry friction whip experiments conducted above, the rotor was not balanced (i.e. it had its native imbalance). For most test runs, no external force/impact was necessary to actuate the whipping action. Dry friction whip occurred at super-critical speeds. For speeds upto 8500 rpm (maximum speed being 10,000 rpm), the whipping action continued with increase in severity of vibrations. The orbit filtered at the dry friction whip frequency was circular. The orbits during partial rub were more elliptical. For a well balanced rotor, it was hard to induce whipping even after impacting the rotor.

The results obtained above agree well with Lingener's [20] and Yu et. al. [9] experimental results. The radius to clearance ratio for this test rig was 75 as compared to 13.3 for Yu et. al. [9] and 2 for Lingener's [20] test rig. The jump-down phenomenon

reported was also observed in the experiments by Yu et. al. [9] and mass imbalance was the cause of onset of dry friction whirl and whip. The current study of dry friction whip is primarily diagnostic by nature and as such, a mathematical model has not been developed to predict whirl frequency range or onset speed of whip. However, based on the study by Childs and Bhattacharya [7], it is believed that a multiple rotor model, correctly accounting for the location of rub, can reasonably predict whip onset speed and frequency.

CHAPTER V

DIAGNOSING COUPLED LATERAL-TORSIONAL VIBRATIONS

Introduction

If excited, torsional natural frequencies can often show up in the lateral vibration spectrum as subsynchronous vibration. As already cited in the Literature Review section, Wachel and Szenasi [13] present a field example of torsional vibrations showing up in the lateral vibration spectrum and also exciting an apparent instability in the compressor. The effect of torsional natural frequencies was suspected only after the lateral instability was accompanied by severely damaged gear teeth. A torsiograph was then used to confirm the suspicions.

In order to study this phenomenon in detail, a new test rig was built with parallel shafts coupled by gears, driven by a D.C. motor on one end and loaded at the other end to closely simulate a real-world machine.

The following sections of this chapter present a way to directly identify torsional subsynchronous vibrations without installing specialized measuring equipment and be able to classify it as unstable or benign vibration.

The Test Rig

Fig 40 shows the test rig built to study coupled lateral-torsional vibrations. It consists of two parallel shafts – the primary (driving) and secondary (driven) shaft – connected by spur gears with a gear ratio of 1.75. The gear arrangement is such that the

secondary shaft rotates faster than the primary shaft. The primary shaft is driven by a high capacity D.C. motor, and at the outboard end of the secondary shaft, a brake wheel is used to load the system and keep the gear teeth in contact at all times. The motor used in this case is a Bauer E1604-1 aircraft D.C. generator rated at 30V and 400 amps and capable of operation up to 8000 rpm. A motor of this size was chosen with a view to provide a large inertia at one end thus keeping the torsional frequencies as low as possible. A torsionally rigid clamp-on coupling was used to transfer the torque from the motor to the primary shaft.

The primary shaft is 3/8in (9.525 mm) in diameter and 24in (609.6 mm) in length and is supported on three ball bearings. The primary inboard and outboard bearings have a span of 22in (559 mm), and the primary gear is mounted at the midspan. The third bearing is mounted about 1.5in (38mm) aft the primary gear. This third point of support was provided to prevent excessive bending of the shaft under the gear radial load. The primary gear itself has a pitch diameter of 3.5in (88.9 mm) and 42 teeth at a pressure angle of 14.5^0. The first lateral natural frequency of this shaft is at 6900 rpm.

The primary gear meshes with the secondary gear, which has a pitch diameter of 2in (50.4 mm) and 24 teeth at the same pressure angle of 14.5^0. The secondary gear is mounted on the secondary shaft through a sleeve and overhangs off the secondary inboard bearing. The secondary shaft itself is 0.5in (12.7 mm) in diameter and 24in (609.6 mm) in length. It sis supported on the secondary inboard and outboard bearings with a span of 20in (508 mm). A large brake-wheel is overhung off the secondary outboard

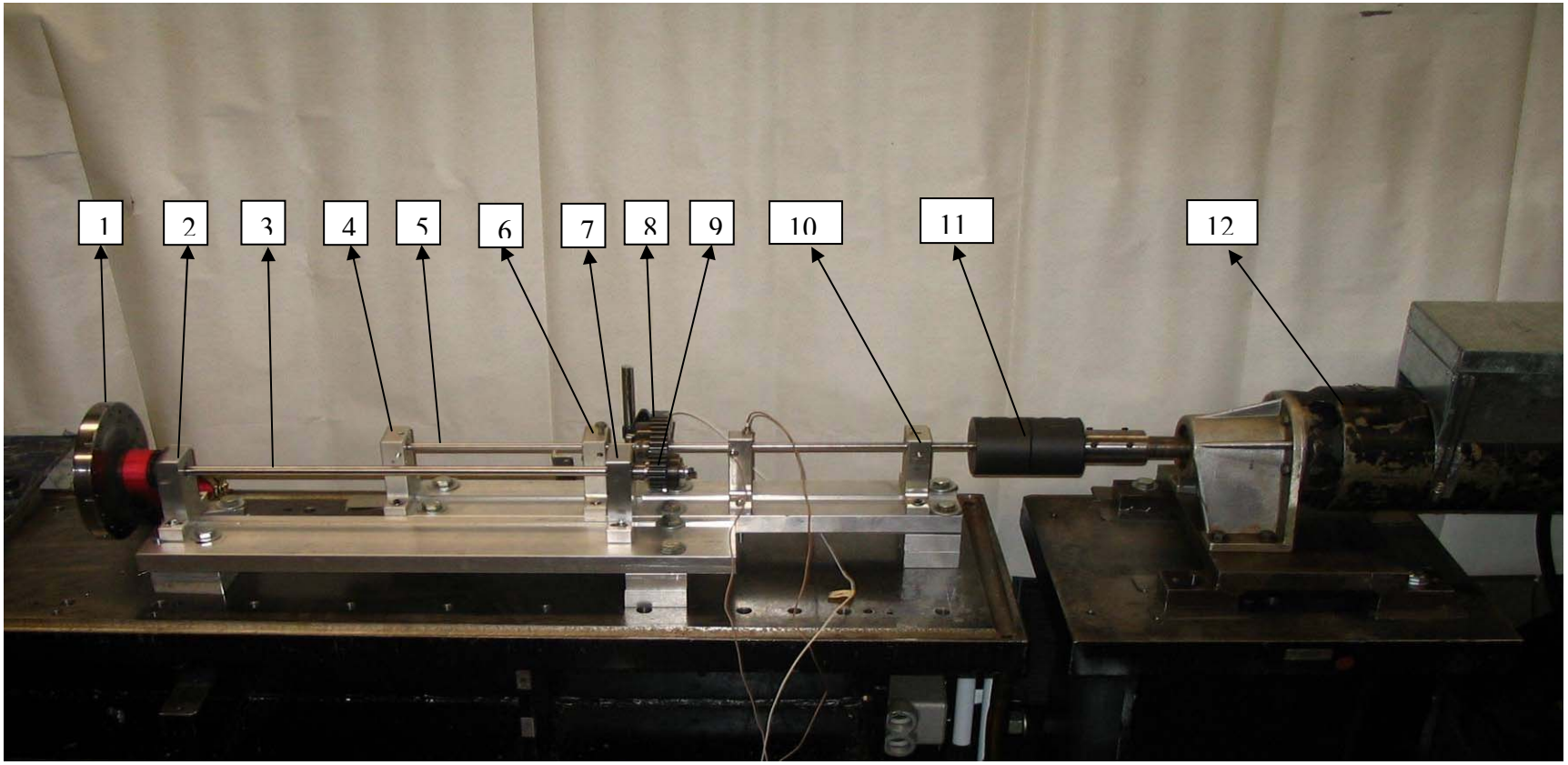

Fig 40: Coupled lateral-torsional vibrations test rig. (1) Brake-wheel (2) Secondary outboard bearing (3) Secondary shaft (4) Primary outboard bearing (5) Primary shaft (6) Primary midspan bearing (7) Secondary inboard bearing (8) Primary gear (9) Secondary gear (10) Primary inboard bearing (11) Clamp-on coupling (12) D.C. motor

bearing. The brake-wheel consists of two cylindrical sections – one 7.0in (177.8 mm) in diameter and the other, 2.0in (50.4 mm) in diameter. .

Forty slots were machined on the larger diameter to use the brake-wheel as a tachometer signal encoder. Load is applied on the break-wheel through a nylon webbing connected to a pawl and ratchet mechanism. A graphite based lubricant capable of temperatures up to 400 ^{0}F (204 ^{0}C) is applied at the interface between the webbing and the break-wheel. The first lateral critical speed of this shaft is at 4000 rpm.

The test rig was designed with the criterion of having its first torsional natural frequency in the 10-15 Hz range. This criterion puts the natural frequency in the torsional natural frequency range of many industrial turbomachinery. Furthermore, the test rig layout is similar to industrial compressors that have a driving motor or a gas turbine at one end and the compressor itself as the loading element with a step-up gear box in between.

Excitation Technique

The Bauer E1604-1 D.C. motor was powered by a Hewlett Packard (HP) 6469C power supply unit that supplies the voltage and current directly to the motor armature. The HP 6469C power supply is capable of 0-36V and 0-300 amps and has coarse and fine knob controls for both voltage and current for speed regulation.

The torsional excitation to the rotor was supplied at the field winding of the D.C. motor. The principle is that, while the armature is supplied with a voltage and current level to keep it running at a constant speed, the external excitation at the field will provide a pulsating torque, effectively alternating the speed of the rotor about its mean

speed. Since field effects tend to be amplified in a D.C. motor, small voltage and current levels are sufficient to excite the rotor.

The external excitation was supplied to the motor by a signal generator via a power amplifier and a safety fuse. The excitation voltage at the required frequency was supplied by a Hewlett Packard 35670A dynamic signal analyzer, which was coupled to a Radio Shack MPA-250A power amplifier. A 0.5 amp fuse was introduced between the power amplifier and the field winding of the motor. Fig 41 shows the excitation circuit components, and Fig 42 shows the schematic diagram of the circuit used for exciting torsional vibrations in the rotor. The signal analyzer supplied the excitation voltage at 1mV-pk. If the frequency was at the torsional natural frequency of the test rig, very small input was required from the amplifier to obtain response from the rotor. The response of the rotor to frequencies other than the natural frequency was limited even after amplification from the amplifier.

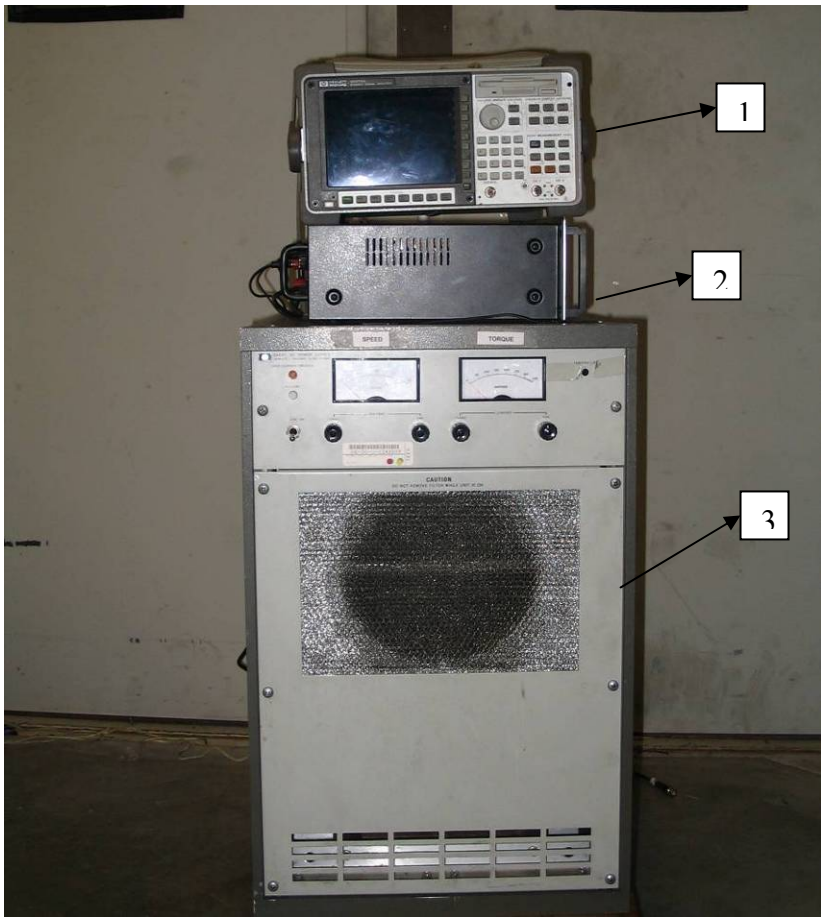

Fig 41: Excitation Circuit Elements. (1) Hewlett Packard 35670A signal analyzer (2) Radio Shack MPA-250A power amplifier (3) Hewlett Packard 6469C D.C. power supply

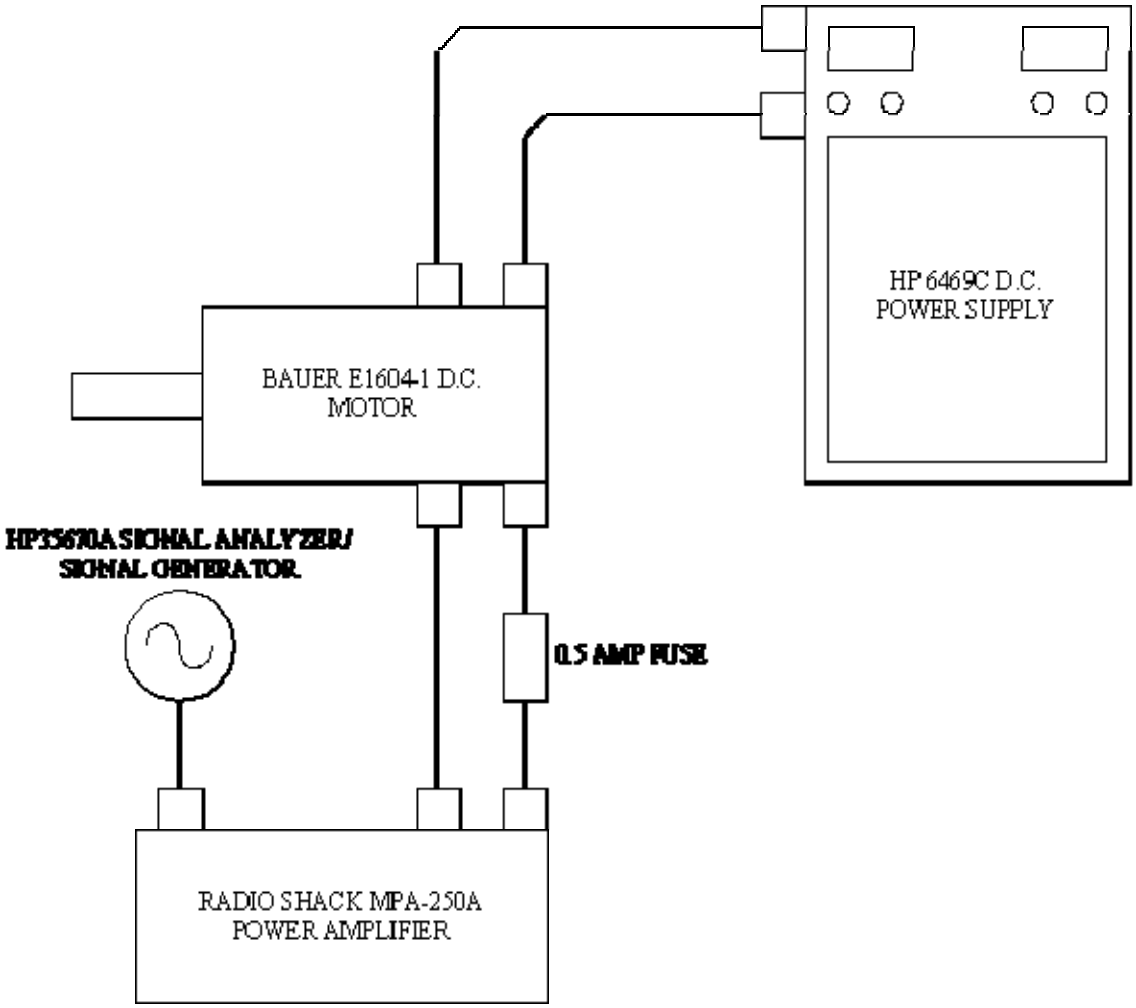

Fig 42: Schematic diagram of torsional excitation circuit

Instrumentation

The instrumentation for the test rig was kept as simple as possible to determine the minimum instrument array required to detect, identify and classify torsional vibrations. To this end, only three proximity probes were all that were required to be used. One probe was used as a keyphasor, on either of the gears or on the brake wheel. The two other probes were used as regular X and Y motion detectors on the shafts. The keyphasor and proximity probes are placed on the same shaft.

A LVTRC data acquisition system was used to gather, store, and analyze the lateral vibration data. LVTorsion was used to study the torsional signals from the test rig.

Torsional Mathematical Model

Fig 43 shows a schematic diagram of the coupled torsional-lateral vibration test rig. I_1, I_2, I_3 and I_4 are the respective polar moments of inertia at the motor, primary gear, secondary gear and break-wheel. θ_1, θ_2, θ_3 and θ_4 are the corresponding angular degrees of freedom and T_1, T_2, T_3 and T_4 the torques/moments at the respective inertias. K_p and K_s are the torsional stiffness values for the primary and secondary shafts respectively. Let N be the gear ratio.

The equations of motion for each of the inertias can be written as:

$$I_1 \ddot{\theta}_1 + K_p(\theta_1 - \theta_2) = T_1 \quad \ldots\ldots\ldots\ldots\ldots\ldots\ldots\ldots(1)$$

$$I_2 \ddot{\theta}_2 + K_p(\theta_2 - \theta_1) = T_2 \quad \ldots\ldots\ldots\ldots\ldots\ldots\ldots\ldots(2)$$

$$I_3 \ddot{\theta}_3 + K_s(\theta_3 - \theta_4) = T_3 \quad \ldots\ldots\ldots\ldots\ldots\ldots\ldots\ldots(3)$$

$$I_4 \ddot{\theta}_4 + K_s(\theta_4 - \theta_3) = T_4 \quad \ldots\ldots\ldots\ldots\ldots\ldots\ldots\ldots(4)$$

Let the gear teeth stiffness be very high when compared to the torsional stiffness of the shafts. Then the following kinematical constraints can be applied.

$$T_2 = -N \cdot T_3 \quad \ldots\ldots\ldots\ldots\ldots\ldots\ldots\ldots\ldots\ldots\ldots\ldots\ldots(5)$$

$$\theta_3 = -N \cdot \theta_2 \quad \ldots\ldots\ldots\ldots\ldots\ldots\ldots\ldots\ldots\ldots\ldots\ldots\ldots(6)$$

Substituting (5) into (3) gives

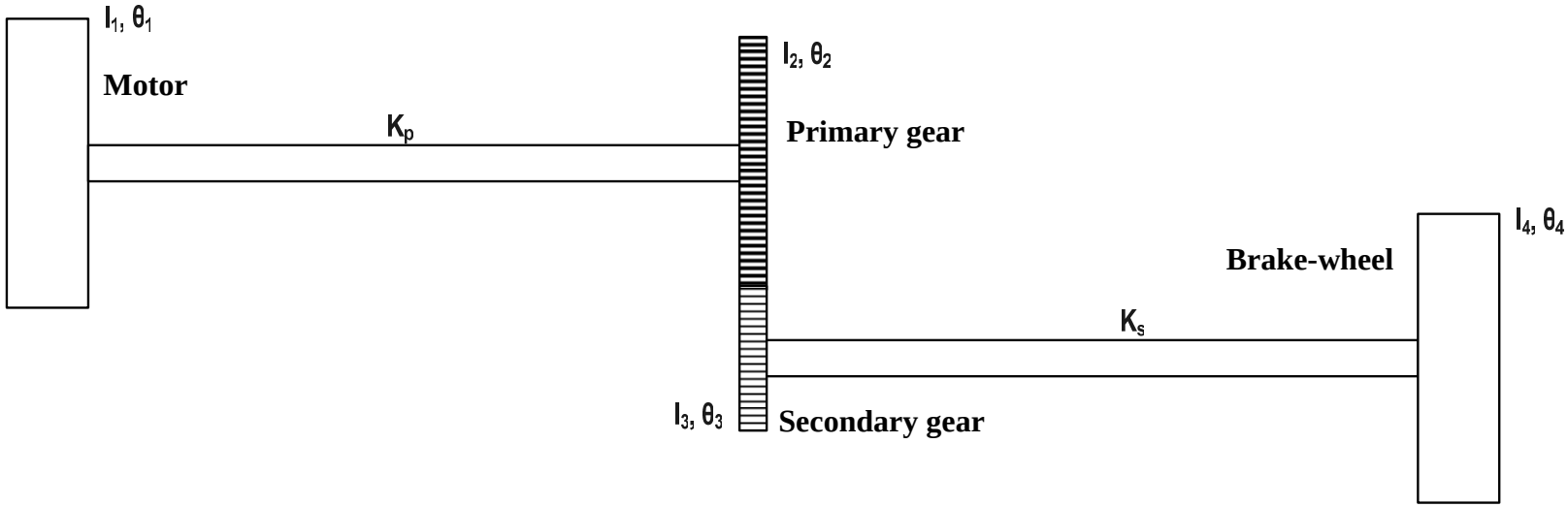

Fig 43: Schematic torsional model of the test rig

$$I_2\ddot{\theta}_2 + K_p(\theta_2 - \theta_1) = -N \cdot T_3 \quad \text{.....(7)}$$

Substituting (6) into (3) and (4) gives

$$N \cdot I_3\ddot{\theta}_2 + K_s(N \cdot \theta_2 - \theta_4) = T_3 \quad \text{.....(8)}$$

$$I_4\ddot{\theta}_4 + K_s(\theta_4 - N \cdot \theta_2) = T_4 \quad \text{.....(9)}$$

Simplifying and combining (7) and (8) to eliminate T_3 gives

$$(I_2 + N^2 I_3)\ddot{\theta}_2 + K_p(\theta_2 - \theta_1) + N^2 K_s\left(\theta_2 - \frac{\theta_4}{N}\right) = 0 \quad \text{.....(10)}$$

Writing (9) in a similar form gives

$$N^2 I_4 \frac{\ddot{\theta}_4}{N} + N^2 K_s\left(\frac{\theta_4}{N} - \theta_2\right) = N \cdot T_4 \quad \text{.....(11)}$$

Equations (1), (10) and (11) give the torsional equations of motion for the rotor system. For the eigen analysis, the right hand side of each equation is reduced to zero, thus giving the final eigen analysis model as,

$$I_1\ddot{\theta}_1 + K_p(\theta_1 - \theta_2) = 0$$

$$(I_2 + N^2 I_3)\ddot{\theta}_2 + K_p(\theta_2 - \theta_1) + N^2 K_s\left(\theta_2 - \frac{\theta_4}{N}\right) = 0$$

$$N^2 I_4 \frac{\ddot{\theta}_4}{N} + N^2 K_s\left(\frac{\theta_4}{N} - \theta_2\right) = 0$$

Writing in matrix format, and putting $\left(\frac{\theta_4}{N}\right) = \theta_4'$, we get

$$\begin{bmatrix} I_1 & 0 & 0 \\ 0 & I_2 + N^2 I_3 & 0 \\ 0 & 0 & N^2 I_4 \end{bmatrix} \begin{bmatrix} \ddot{\theta}_1 \\ \ddot{\theta}_2 \\ \ddot{\theta}'_4 \end{bmatrix} + \begin{bmatrix} K_p & -K_p & 0 \\ -K_p & K_p + N^2 K_s & -N^2 K_s \\ 0 & -N^2 K_s & N^2 K_s \end{bmatrix} \begin{bmatrix} \theta_1 \\ \theta_2 \\ \theta'_4 \end{bmatrix} = 0$$

This system of equations can be solved by substituting $\theta_n = A_n \cdot e^{st}$, solving the resultant quadrilateral equation in 's' and finding $\omega = \sqrt{|s|}$, where ω is the torsional natural frequency.

The torsional stiffness value of the shaft is evaluated using the formula $K = \frac{\pi \cdot G \cdot D^4}{32 \cdot L}$ lb-in/rad (N-m/rad) , where,

G = Shear Modulus, psi (Pa)

D = Diameter, in (m)

L = Length, in (m)

Using the geometric dimensions of the shaft, the torsional stiffness values are calculated to be K_p=1624.52 lb-in/rad (184 N-m/rad) and K_s=2901.89 lb-in/rad (328.67 N-m/rad)

The inertia values are evaluated as –

I_1 = 0.574 lb-in-sec^2 (0.0648 kg-m^2) (Refer Appendix IV)

I_2 = 1.006E-02 lb-in-sec^2 (0.001136 kg-m^2)

I_3 = 1.226 E-03 lb-in-sec^2 (0.0001385 kg-m^2)

I_4 = 1.339E-01 lb-in-sec^2 (0.01512 kg-m^2)

Substituting these values into the model obtained above, the first torsional natural frequency of the test rig is calculated to be 12.01 Hz, and the second natural frequency is found to be 140.56 Hz.

Non-rotating Tests

A non-rotating torsional 'rap' test was conducted first to determine the torsional natural frequency of the test rig. A proximity probe was placed at the brake-wheel to use the slots as encoders. The shaft was then rotated slightly by hand to ensure that the gear teeth were in contact. Then a small angular motion was given to the brake-wheel and the response measured on a Hewlett Packard 35670A signal analyzer. Fig 44 and Fig 45 show the response plots of the 'rap' test with respect to frequency and time domains, respectively. It can be seen that 11 Hz is the first torsional natural frequency of the system. This value is close to the calculated value of 12.01 Hz taking into account errors in estimating the inertia of the D.C. motor.

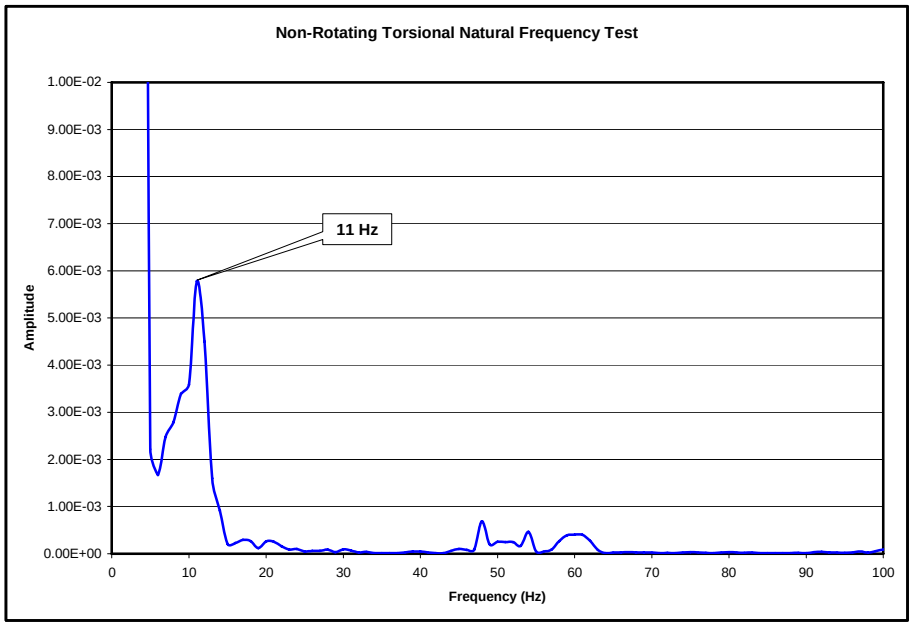

Fig 44: Non-rotating torsional rap test; amplitude vs. frequency plot

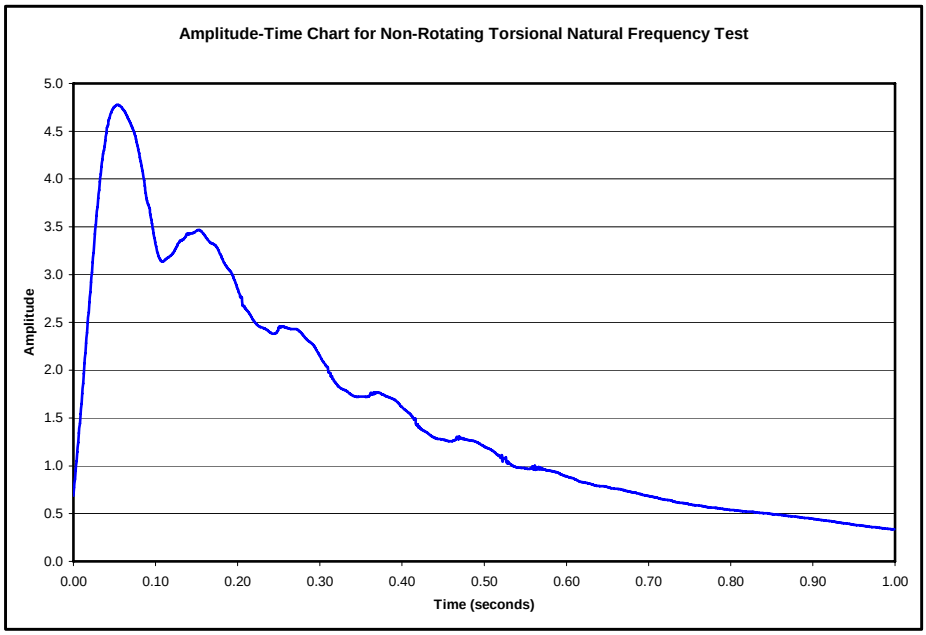

Fig 45: Non-rotating torsional rap test; amplitude vs. time plot

Rotating Tests

The first set of rotating tests was performed by placing the measurement probes on the primary shaft, with the keyphasor on the primary gear. The machine was slowly run up to a speed of 1400 rpm. On the run-up, it was found that the 2X signal excited the torsional natural frequency, evident from the sudden increase in the 2X amplitude as it passed through 11 Hz. This is shown in Fig 46. Also, when the synchronous speed coincided with the first torsional natural frequency at 11 Hz, there was a sudden spike in the synchronous response, showing the effect of a coupled torsional-lateral response. This is shown in Fig 47. Once the speed crossed the 1000 rpm limit, there were subsynchronous vibrations at the torsional natural frequency of 11 Hz, without any external excitation. These subsynchronous signals were breathing in nature and intermittent and the amplitudes were as large as half the synchronous response of the rotor. This result is shown in Fig 48. The rotor was then excited by supplying a sinusoidal voltage at 11 Hz to the field windings of the motor. The amplitude of the subsynchronous vibrations were now equal to the synchronous response and the nature of these vibrations were constant instead of breathing, as was seen in the earlier case with no external excitation. This response is shown in Fig 49.

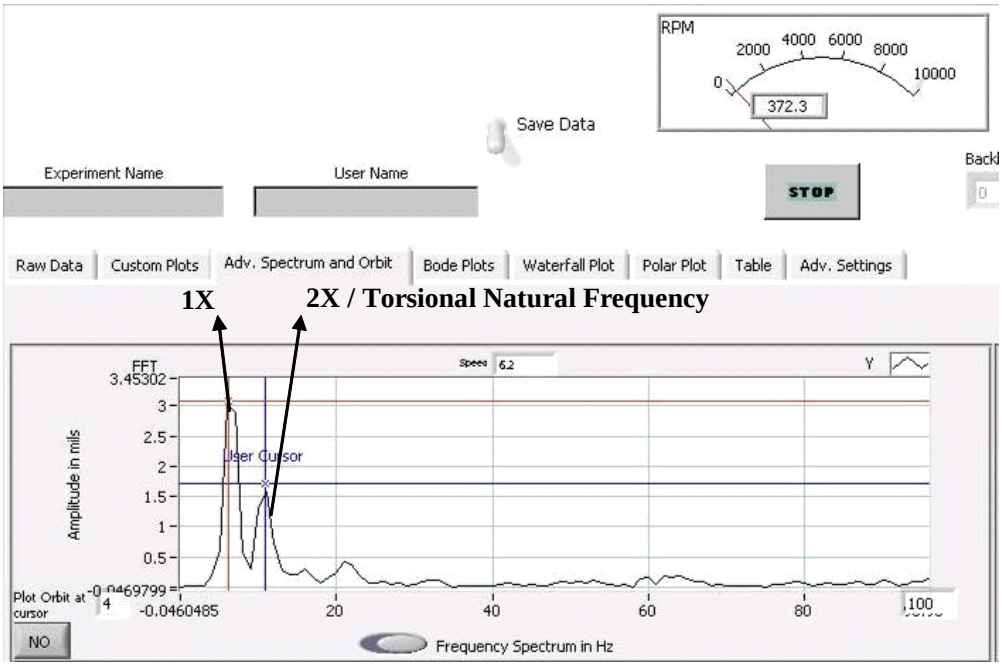

Fig 46: Torsional natural frequency excited by the 2X signal

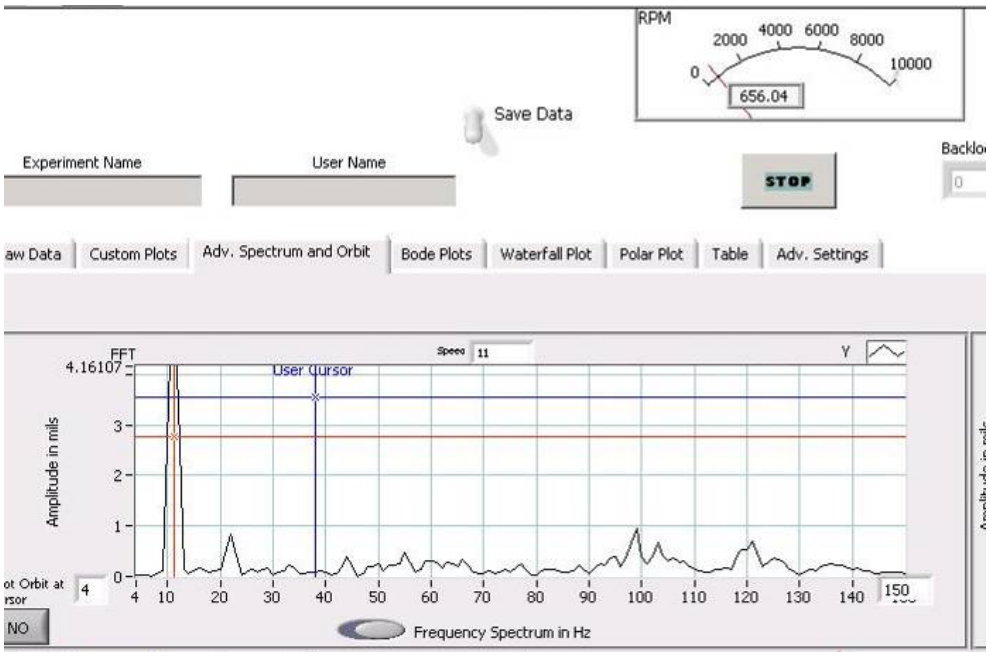

Fig 47: Spike in the lateral synchronous response at the first torsional natural frequency

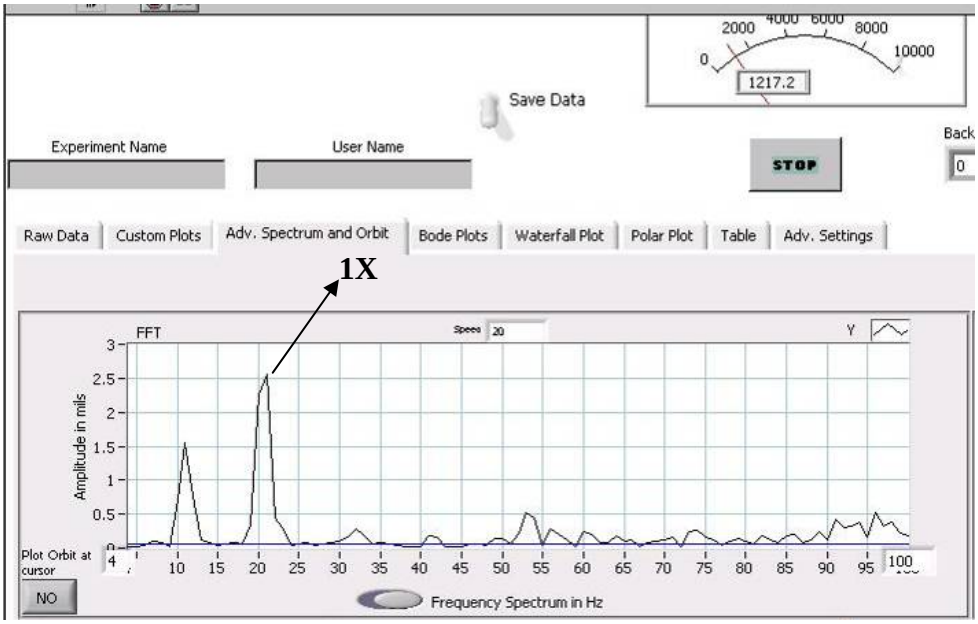

Fig 48: Subsynchronous vibration with no external excitation

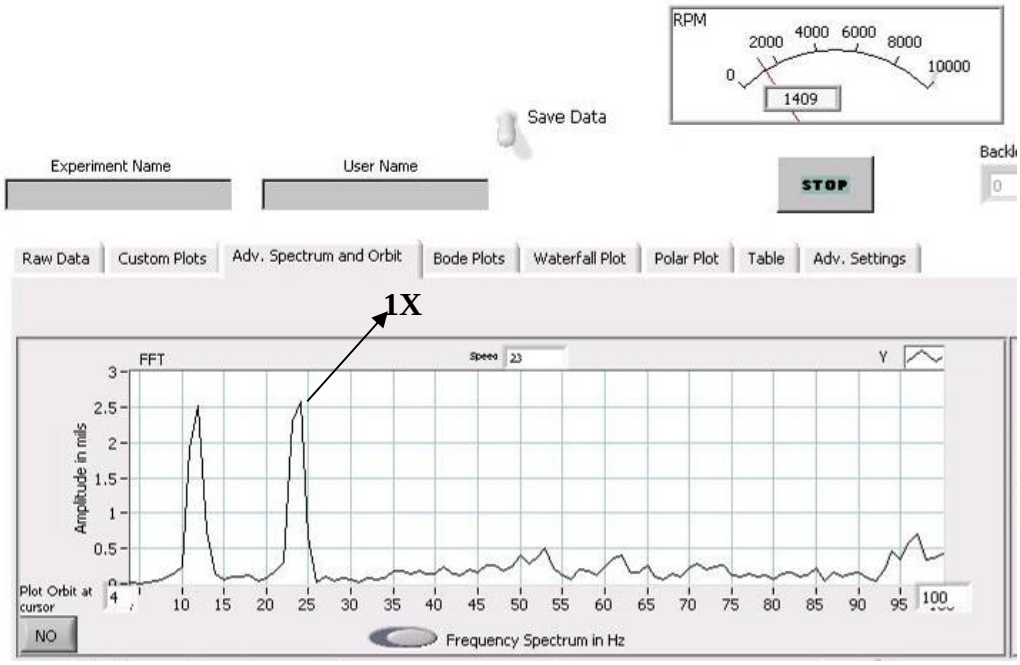

Fig 49: Subsynchronous response with external excitation

One unique way to identify torsional natural frequencies is to observe the frequency response at the carrier wave frequency, which in this case is the gear meshing frequency. Since, by their very nature, torsional natural frequencies cause speed fluctuation about the mean operating speed with an amplitude equal to the torsional natural frequency under excitation, the carrier wave can be expected to show side bands on either side of the mean carrier frequency. The difference between the mean carrier frequency and either of the side band frequencies is the frequency of the torsional natural frequency under excitation. If this difference matches the lateral subsynchronous frequency observed, then it would strongly indicate the presence of torsional vibrations as opposed to purely lateral excitations. Fig 50 shows the carrier wave frequency and side bands at the primary gear, measured by proximity probes on the primary shaft. Fig 51 shows the frequency response of the keyphasor on the primary gear. It can be seen that the side bands are very small in amplitude compared to the mean carrier wave frequency. This is because the gears are at the node of the first torsional mode and hence see small torsional amplitudes.

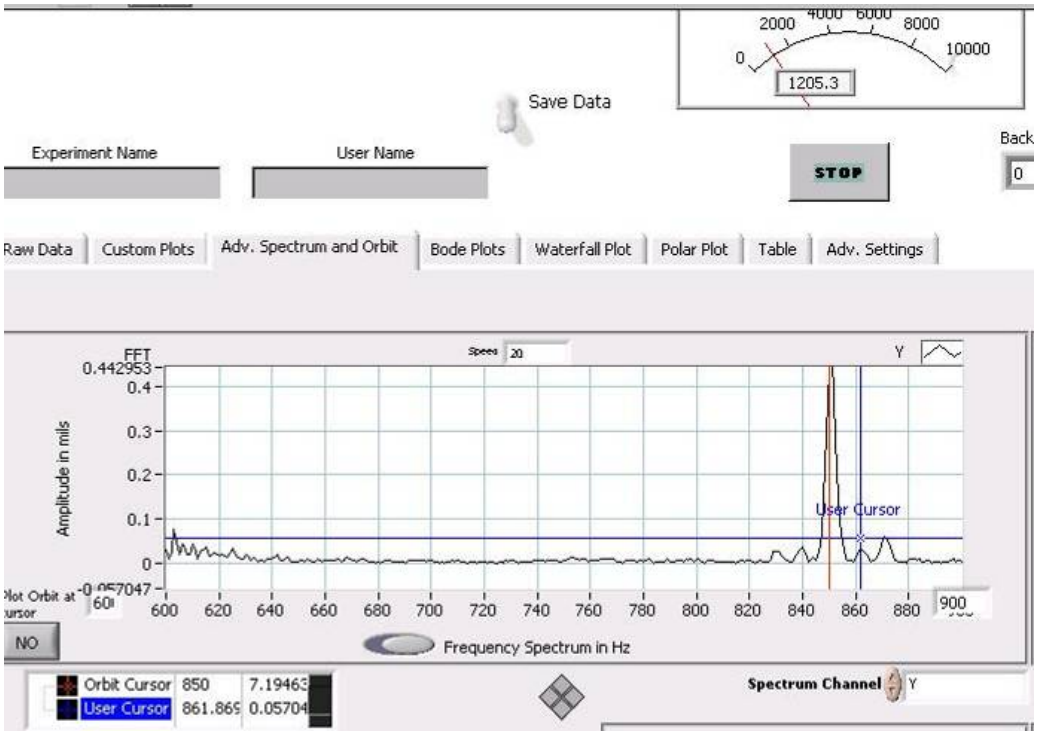

Fig 50: Carrier wave along with side-bands for the primary shaft measured by the 'Y' proximity probe

In order to better observe the side bands, the keyphasor was now placed at the brake-wheel, which is at the anti-node of the first torsional mode. Accordingly, the proximity probes were shifted to the secondary shaft. The subsynchronous vibration observed on this shaft was similar to that of the primary shaft. However, the side-bands near the carrier wave were larger and more pronounced than those measured at the primary shaft. The side bands measured at the 'X' proximity probe are shown in Fig 52, and the frequency response of the keyphasor is shown in Fig 53. LVTorsion was also

used to study the torsional vibration of the shafts. Fig 54 shows the torsional vibration data recorded on the secondary shaft and validates the results obtained from LVTRC.

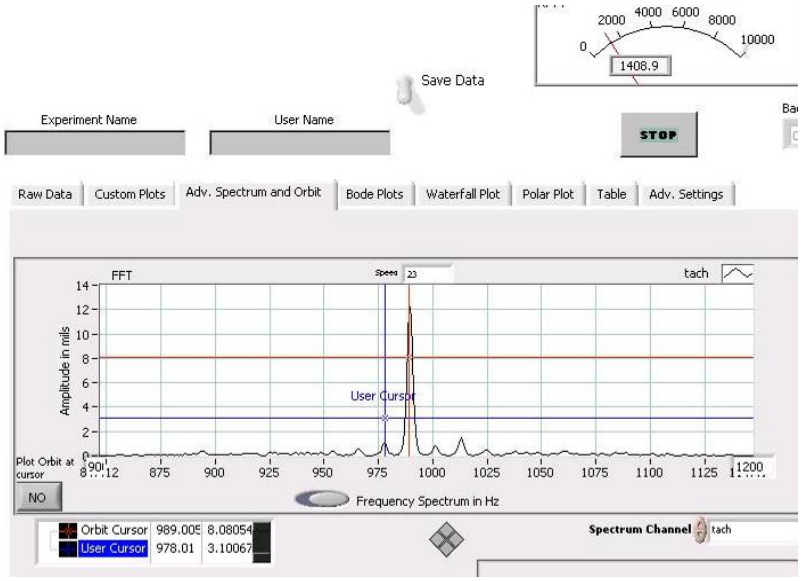

Fig 51: Carrier wave along with side-bands for the primary shaft seen in the keyphasor frequency response.

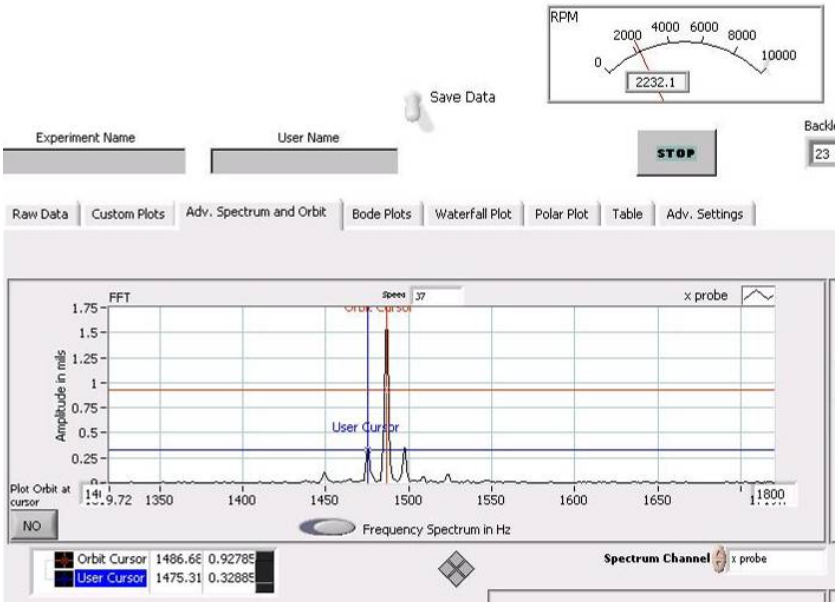

Fig 52: Carrier wave along with side-bands for the secondary shaft measured by the 'X' probe

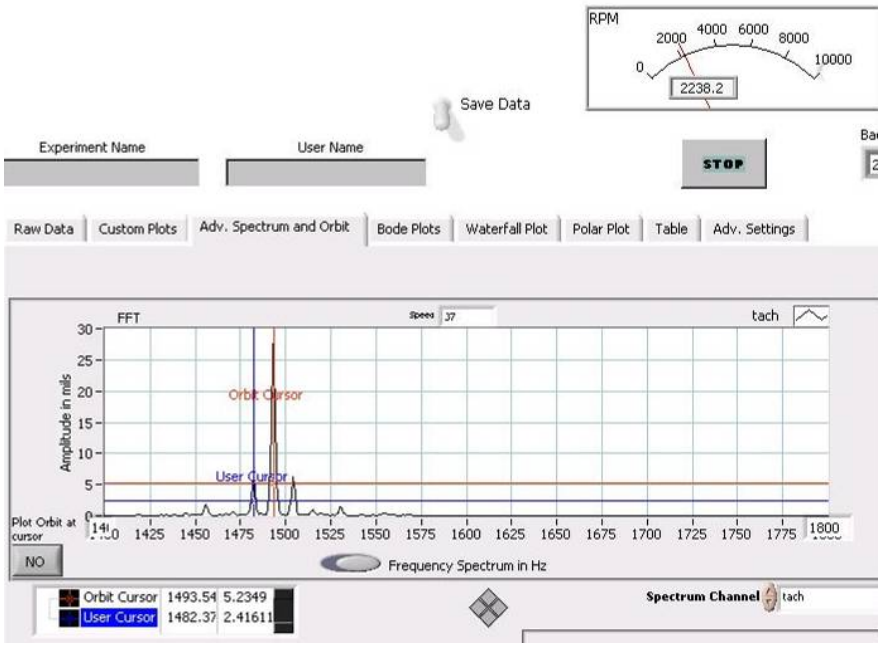

Fig 53: Carrier wave along with side-bands for the secondary shaft seen in the keyphasor frequency response

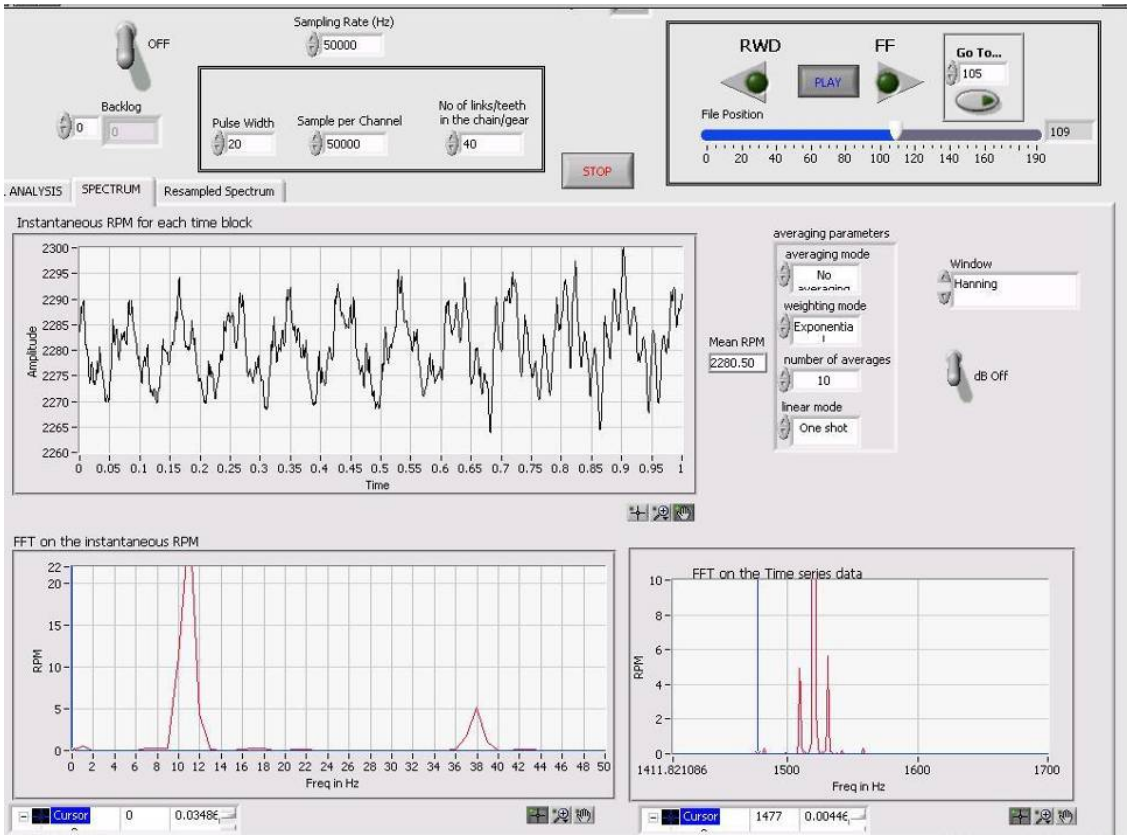

Fig 54: LVTorsion results confirming the torsional natural frequency at 11 Hz

It is now required to identify whether the subsynchronous vibration resulting from the torsional natural frequency is a true instability or a benign motion. To do this, orbit plots filtered at the subsynchronous vibration were studied in detail. They showed that the orbit filtered at the subsynchronous vibration, constantly oscillated between forward and backward whirl mode. By nature, lateral rotordynamic instabilities occur due to rotor whirl amplitudes building up in either the backward or forward whirl direction in an exponential manner, primarily due to loss of effective damping. Though, theoretically, the amplitudes should be infinitely large, most instabilities end in limit

cycles due to non-linear effects. In the case of the subsynchronous vibrations caused by torsional natural frequency interference, due to the constantly changing whirl direction, it is highly unlikely that the amplitudes would build up in a manner leading to instability. This subsynchronous motion is stable in nature. However, it is important to note here that stable vibration does not necessarily insure the machine from mechanical damage. These vibrations will still need to be eliminated to ensure reliable operation of the turbomachine. Fig 55 and Fig 56 show the constantly changing whirl direction in the orbit filtered at the subsynchronous vibration.

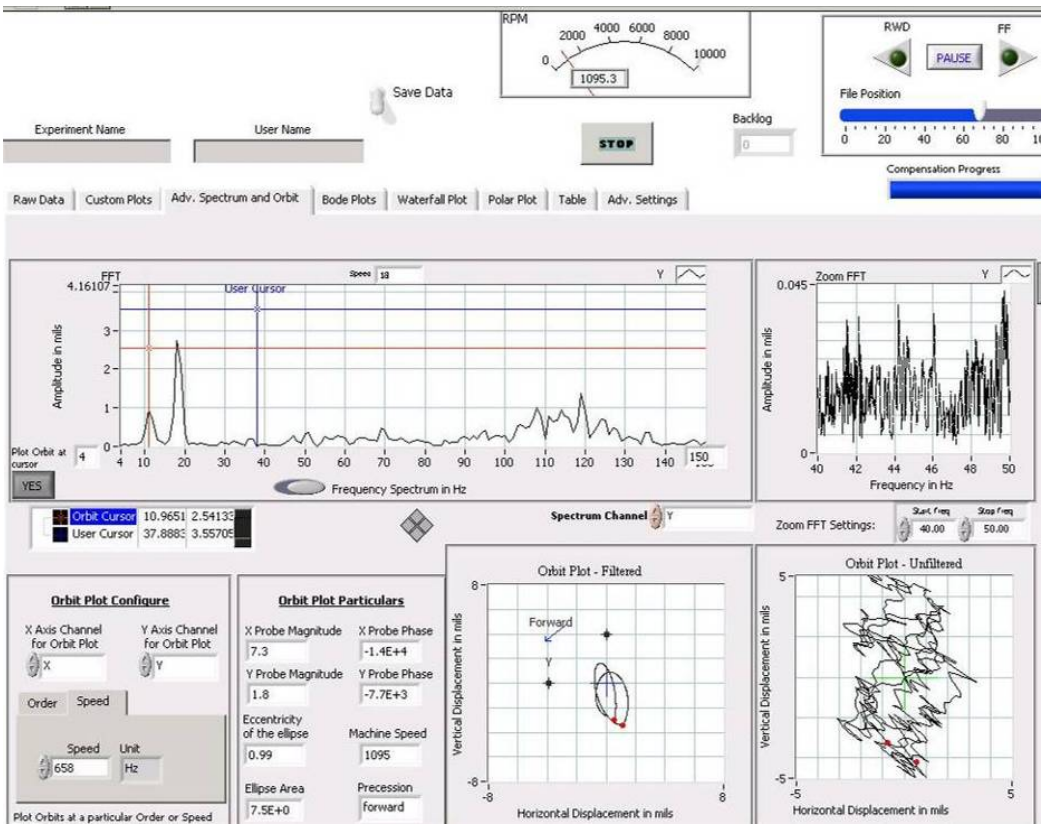

Fig 55: Subsynchronous orbit in forward whirl

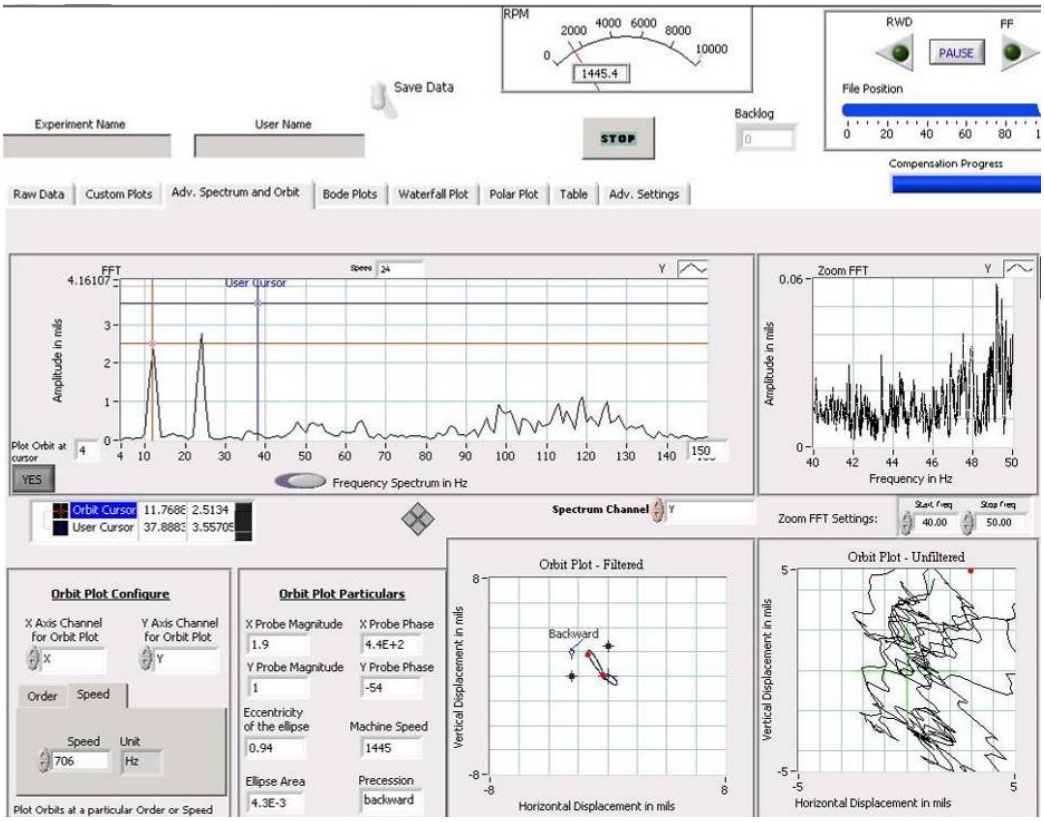

Fig 56: Subsynchronous orbit in backward whirl

CHAPTER VI

CONCLUSION

This thesis presents various cases of stable and unstable subsynchronous vibrations and methodologies to signal analyze them. Coupled torsional-lateral vibrations, subsynchronous vibrations from a loose bearing and dry friction whip have been experimentally simulated. Unique indicators to identify each of them have been presented. Ways to classify them as benign or unstable vibrations have also been reported.

The possibility of using phase angle as a potential indicator of instability has also been reported. Theoretical analysis has been performed on test rig rotors and the results from these analyses have been applied to real world machines. The results are encouraging.

It is the author's belief that, although only a few cases have been simulated and analyzed, the general rules applied to signal analyze these phenomena can be judiciously applied to any case on the field in order effect a quick and accurate diagnosis of rotordynamic problems.

REFERENCES

[1] Vance, John M, 1988, "Rotordynamics of Turbomachinery", John Wiley and Sons, New York.

[2] Fowlie, D.W., Miles, D.D., 1975, "Vibration Problems with High Pressure Centrifugal Compressors", ASME Paper No. 75 – PET – 28.

[3] Newkirk, B.L., 1924, "Shaft Whipping", General Electric Review, **27** (3), pp. 169-178.

[4] Kimball, Jr., A.L., 1924, "Internal Friction Theory of Shaft Whirling", General Electric Review, **27** (4), pp. 244-251.

[5] Childs, D.W., Ehrich, F.F., 1984, "Self-excited Vibration in High Performance Turbomachinery", Mechanical Engineering, **106** (5), pp. 66-79.

[6] Black, H., 1968, "Interaction of a Whirling Rotor with a Vibrating Stator across a Clearance Annulus", Journal of Mechanical Engineering Science, **10** (1), pp. 1-12.

[7] Childs, D., Bhattacharya, A., 2007, "Prediction of Dry-Friction Whirl and Whip between a Rotor and Stator", Journal of Vibrations and Acoustics, **129**, pp. 355-362.

[8] Schultheis, S.M., 2003, "Diagnosing Rubs in Turbomachinery", *Proceedings of the National Technical Training Symposium and 27th Annual Meeting of the Vibration Institute*, New Orleans, Louisiana, United States.

[9] Yu, J.J., Goldman, P., and Bently, D.E., 2000, "Rotor/Seal Experimental and Analytical Study of Full Annular Rub", *Proceedings of the ASME IGTI Turboexpo 2000*, New York, USA, Vol. 2000-GT-389, pp. 1-9.

[10] Smith, Kenneth J, 1975, "An Operational History of Fractional Frequency Whirl", *Proceedings of the Fourth Turbomachinery Symposium*, College Station, USA, pp. 115-125.

[11] Doyle, H.E., 1982, "Field Experiences with Rotordynamic Instability in High-Performance Turbomachinery", NASA Conference Publication 2133, pp. 3-4.

[12] Wachel J.C., 1982, "Rotordynamic Instability Field Problems", NASA Conference Publication 2250, pp. 1-19.

[13] Wachel, J. C., and Szenasi, F. R., 1980 "Field Verification of Lateral-Torsional Coupling Effects on Rotor Instabilities in Centrifugal Compressors", NASA Conference Publication 2133, pp. 15-34.

[14] Bently. D., 1974, "Forced Subrotative Speed Dynamic Action of Rotating Machinery", ASME Paper No. 74-PET-16.

[15] Childs, D.W., 1981, "Fractional-Frequency Rotor Motion Due to Non-symmetric Clearance Effects", ASME Paper No. 81-GT-145.

[16] Ertas, Bugra; Kar, Rahul; Vance, John, 2004, "Diagnosing Subsynchronous Vibration: Unstable or Benign", *Turbomachinery Research Consortium Meeting*, Report TRC-RD-2-04, Texas A&M University, College Station, TX.

[17] Kar. Rahul; Vance, John, 2007, "Subsynchronous Vibrations in Turbomachinery – Methodologies to Identify Potential Instability", ASME Paper No. GT2007-27048.

[18] Jafri, Syed Mohsin, 2007, "The Effect of Shrink Fits on the Threshold Speed of Rotordynamic Instability", Ph.D. Dissertation, Texas A&M University, College Station, TX.

[19] Jiang, Jun; Ulbrich, Heinz, 2005, "The Physical Reason and the Analytical Condition for the Onset of Dry Whip in Rotor-Stator Contact Systems", Journal for Vibration and Acoustics, Transactions of the ASME, **127** (6), pp. 594-603.

[20] Lingener, A., 1990, "Experimental Investigation of Reverse Whirl of a Flexible Rotor", Transactions, *IFToMM (International Federation for the Promotion of Mechanism and Machine Science) 3rd International Conference on Rotordynamics*, Lyon, France, pp. 19-26.

Supplemental References

[1] Ehrich, F.F., 1966, "Subharmonic Vibration of Rotors in Bearing Clearance", ASME Paper No. 66-MD-1.

[2] French, R.S., 1981, "An Experimental Study of Torsional Vibration Measurement", M.S. Thesis, Texas A&M University, College Station, Texas.

[3] Iwatsubo, T.; Arii, S.; Kawaii, R., 1984,"Coupled Lateral Torsional Vibration of A Geared Rotor System", *IMech E Conference Publications* (Institution of Mechanical Engineers), York, United Kingdom, pp. 59-66.

[4] Murphy, B.T., 1984, "Eigenvalues of Rotating Machinery", Ph.D. Dissertation, Texas A&M University, College Station, TX.

[5] Schwibinger, P., Nordmann, R., 1988, "Influence of Torsional-Lateral Coupling On Stability Behavior of Geared Rotor Systems", Journal of Engineering for Gas Turbines and Power, Transactions of the ASME, **110** (4), pp. 563-571.

[6] Muszynska, A., 1989, "Rotor-to-stationary Element Rub-Related Vibration Phenomena in Rotating Machinery", The Shock and Vibration Digest, **21**, pp. 3-11.

[7] Yao-Qun Lin, 1991, "Rotor Instability Induced by Dead-band Clearance in Bearing Supports", Ph.D. Dissertation, Texas A&M University, College Station, TX.

[8] Childs, D., 1993, Turbomachinery Rotordynamics: Phenomena, Modeling, and Analysis, John Wiley and Sons, New York.

[9] Muszynska, Agnes, Goldman, Paul, 1993, "Chaotic Vibrations of Rotor/bearing/stator Systems with Looseness or Rubs", ASME, Design Engineering Division DE, **54**, Nonlinear Vibrations, pp. 187-194.

[10] Walker, Duncan N, Torsional Vibration of Turbomachinery, McGraw-Hill, New York, 2003.

[11] Kar, Rahul; Vance, John, 2005, "Diagnostics of Subsynchronous Vibrations", *Turbomachinery Research Consortium Meeting*, Report TRC-RD-2-05, Texas A&M University, College Station, TX.

APPENDIX I

LATERAL ROTORDYNAMIC ANALYSIS OF THE EKOFISK COMPRESSOR

The lateral rotordynamic analysis for the Ekofisk compressor is carried out in XLTRC^2 rotordynamics code using the same model shown in Fig 12. The Ekofisk compressor that went unstable was the high pressure (HP) gas re-injection compressor in a series of two compressors that compressed gas received from the separator area at 986 psi (68 bar) to 9062 psi (625 bar). The low pressure (LP) compressor pressurized the gas from 986 psi (68 bar) to 3480 psi (240 bar) and the HP compressor further compressed the gas from the LP compressor to 9062 psi (625 bar). Each compressor had eight stages in a back-to-back arrangement with a rated operating speed of 8500 rpm.

It is clear from the pressure data that the overall compression ratio of the LP compressor is 3.53 and that of the HP compressor is 2.60. Assuming equal compression in each of the eight stages, the pressure ratio per stage for the LP compressor is 1.17 and for the HP compressor, 1.13. This puts the pressure on each side of the central labyrinth seal of the LP compressor at 1847 psi (127 bar) and 3480 psi (240 bar). The corresponding pressures for the HP compressor are 5674 psi (391 bar) and 9062 psi (625 bar). The pressure difference across the central labyrinth seal for the LP compressor is 1632 psi (113 psi) and for the HP compressor is 3389 psi (234 bar). It is also assumed that the pressure for the compressors varies linearly with speed. Using these assumptions

and values, the rotordynamic coefficients for the labyrinth seal was computed for an inlet swirl ratio of 0.5 and this is shown in Fig 57 below and Fig 58 shows the variation of the direct and cross-coupled stiffness coefficients with speed.

XLLaby™ Worksheet for labyrinth seals

Version 2.0, Copyright 1996 - 1998 by Texas A&M University. All rights reserved.

Title: Centre labyrinth seal_linear

Seal Radius	6.7	in	Ratio of Specific Heats	1.502	--
Radial Clearance	0.009	in	Gas Constant	315.016	ft-lb/ lb°R
Tooth Location	S	R or S	Compressibility Factor	1	--
Number of Teeth	19	--	Kinematic Viscosity	2.57E+01	cst
Tooth Pitch	0.28	in	Reservoir Temperature	210	F
Tooth Height	0.118	in	Reservoir Pressure	Use J	psi
Tooth Width	0.0276	in	Sump Pressure	Use K	psi
Stator Friction Constant	0.079	--	Inlet Tangential Velocity Ratio	0.5	--
Stator Friction Exponent	-0.25	--			
Rotor Friction Constant	0.079	--			
Rotor Friction Exponent	-0.25	--			

									J	K	
Speed	Kxx	Kxy	Kyx	Kyy	Cxx	Cxy	Cyx	Cyy	Res. Press.	Sump Press.	fw
rpm	lb/in	lb/in	lb/in	lb/in	lb-s/in	lb-s/in	lb-s/in	lb-s/in	psi	psi	-
500	1.745E+03	-8.699E+02	8.699E+02	1.745E+03	3.936E+01	6.236E+00	-6.236E+00	3.936E+01	2922.59	1792.48	-0.422
1000	9.086E+02	-1.841E+03	1.841E+03	9.086E+02	4.580E+01	1.394E+01	-1.394E+01	4.580E+01	3306.33	2035.06	-0.384
1500	-9.499E+02	-2.799E+03	2.799E+03	-9.499E+02	5.313E+01	2.299E+01	-2.299E+01	5.313E+01	3690.08	2277.65	-0.335
2000	-4.063E+03	-3.656E+03	3.656E+03	-4.063E+03	6.123E+01	3.323E+01	-3.323E+01	6.123E+01	4073.82	2520.23	-0.285
2500	-8.656E+03	-4.345E+03	4.345E+03	-8.656E+03	7.001E+01	4.461E+01	-4.461E+01	7.001E+01	4457.57	2762.82	-0.237
3000	-1.495E+04	-4.805E+03	4.805E+03	-1.495E+04	7.943E+01	5.711E+01	-5.711E+01	7.943E+01	4841.31	3005.41	-0.193
3500	-2.316E+04	-4.971E+03	4.971E+03	-2.316E+04	8.951E+01	7.072E+01	-7.072E+01	8.951E+01	5225.05	3247.99	-0.152
4000	-3.353E+04	-4.769E+03	4.769E+03	-3.353E+04	1.003E+02	8.544E+01	-8.544E+01	1.003E+02	5608.80	3490.58	-0.114
4500	-4.627E+04	-4.118E+03	4.118E+03	-4.627E+04	1.118E+02	1.013E+02	-1.013E+02	1.118E+02	5992.54	3733.16	-0.078
5000	-6.163E+04	-2.928E+03	2.928E+03	-6.163E+04	1.240E+02	1.183E+02	-1.183E+02	1.240E+02	6376.29	3975.75	-0.045
5500	-7.985E+04	-1.097E+03	1.097E+03	-7.985E+04	1.371E+02	1.365E+02	-1.365E+02	1.371E+02	6760.03	4218.34	-0.014
6000	-1.012E+05	1.491E+03	-1.491E+03	-1.012E+05	1.512E+02	1.559E+02	-1.559E+02	1.512E+02	7143.78	4460.92	0.01570
6500	-1.259E+05	4.963E+03	-4.963E+03	-1.259E+05	1.661E+02	1.766E+02	-1.766E+02	1.661E+02	7527.52	4703.51	0.04389
7000	-1.543E+05	9.465E+03	-9.465E+03	-1.543E+05	1.822E+02	1.986E+02	-1.986E+02	1.822E+02	7911.27	4946.09	0.07089
7500	-1.866E+05	1.516E+04	-1.516E+04	-1.866E+05	1.993E+02	2.220E+02	-2.220E+02	1.993E+02	8295.01	5188.68	0.09684
8000	-2.231E+05	2.222E+04	-2.222E+04	-2.231E+05	2.176E+02	2.467E+02	-2.467E+02	2.176E+02	8678.76	5431.26	0.12189
8500	-2.643E+05	3.087E+04	-3.087E+04	-2.643E+05	2.373E+02	2.730E+02	-2.730E+02	2.373E+02	9062.50	5673.85	0.14617

Fig 57: Rotordynamic coefficients for labyrinth seal

Wachel's formula from Wachel [12] was used to calculate cross-coupled forces created in the annular space between the impellers and the shroud at the maximum oprating speed of 8500 rpm. A linear variation was assumed for all other speeds. Fig 59 shows the cross-coupled stiffness values used for the analysis.

The bearings used for the Ekofisk compressor were 5-pad tilt pad bearings with load-on-pad configuration. The oil properties were taken at 124 ^{0}F (51 ^{0}C) as reported in Wachel [12] and are shown in Fig 60.

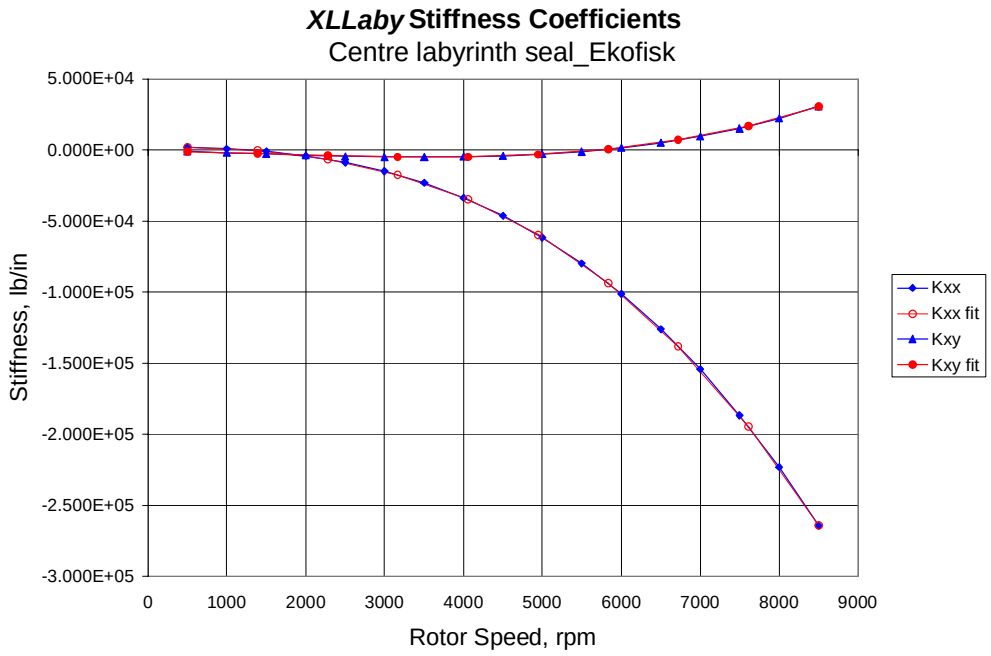

Fig 58: Variation of direct and cross-coupled stiffness coefficients with speed

Wachel [12] reports that the rigid support critical speed for the rotor as 4200 rpm. A model check showed that the rigid support critical speed to be at 4500 rpm, indicating a reasonably accurate model. Incorporating the central labyrinth seal stiffness increased

XLUseKCM™ User Defined Support Stiffness, Damping, and Mass Rotordynamic Coefficients — Press Control-F1 for help.

Title: Impeller_user

Perform a Paste/Special/Link for the Title box within XLTRC to create a link to your rotor model.

Speed	Kxx	Kxy	Kyx	Kyy	Cxx	Cxy	Cyx	Cyy	Mxx	Mxy	Myx	Myy
rpm	lb/in	lb/in	lb/in	lb/in	lb-s/in	lb-s/in	lb-s/in	lb-s/in	lb-s**2/in	lb-s**2/in	lb-s**2/in	lb-s**2/in
500	0	371.65	-371.65	0	0	0	0	0	0	0	0	0
1000	0	743.29	-743.29	0	0	0	0	0	0	0	0	0
1500	0	1114.94	-1114.94	0	0	0	0	0	0	0	0	0
2000	0	1486.59	-1486.59	0	0	0	0	0	0	0	0	0
2500	0	1858.24	-1858.24	0	0	0	0	0	0	0	0	0
3000	0	2229.88	-2229.88	0	0	0	0	0	0	0	0	0
3500	0	2601.53	-2601.53	0	0	0	0	0	0	0	0	0
4000	0	2973.18	-2973.18	0	0	0	0	0	0	0	0	0
4500	0	3344.82	-3344.82	0	0	0	0	0	0	0	0	0
5000	0	3716.47	-3716.47	0	0	0	0	0	0	0	0	0
5500	0	4088.12	-4088.12	0	0	0	0	0	0	0	0	0
6000	0	4459.76	-4459.76	0	0	0	0	0	0	0	0	0
6500	0	4831.41	-4831.41	0	0	0	0	0	0	0	0	0
7000	0	5203.06	-5203.06	0	0	0	0	0	0	0	0	0
7500	0	5574.71	-5574.71	0	0	0	0	0	0	0	0	0
8000	0	5946.35	-5946.35	0	0	0	0	0	0	0	0	0
8500	0	6318.00	-6318.00	0	0	0	0	0	0	0	0	0

Fig 59: Impeller aerodynamic cross-coupled stiffness using Wachel's formula

XLJrnl™ Spreadsheet for Journal Bearing Coefficients

Title: 5Pads Tilt pad bearings

Bearing Type: 5 Pad Tilting, LOP

Bearing Length	1.5	inches
Bearing Diameter	5	inches
Pad Clr, Cp	0.0035	inches
Bearing Load, F	710	lbf
Bearing Preload, m	0	--

Lubricant Viscosity	2.40E-06	Reyns
Lubricant Density	0.85	sp. gr.

Speed	Kxx	Kxy	Kyx	Kyy	Cxx	Cxy	Cyx	Cyy	W.F.R.	Ecc.	Attan.	Somm.
rpm	lb/in	lb/in	lb/in	lb/in	lb-s/in	lb-s/in	lb-s/in	lb-s/in			deg	
500	102519	0	0	2423630	6260	0	0	34821	0.00	0.68	0.00	0.4312
2500	236296	0	0	1101939	4871	0	0	7241	0.00	0.39	0.00	2.1558
4500	269417	0	0	815986	4401	0	0	4612	0.00	0.27	0.00	3.8804
6500	281779	0	0	660470	4180	0	0	3689	0.00	0.19	0.00	5.6051
7600	282349	0	0	614859	4097	0	0	3428	0.00	0.17	0.00	6.5536
8500	282816	0	0	577542	4045	0	0	3264	0.00	0.15	0.00	7.3297
10500	283852	0	0	494613	3961	0	0	3000	0.00	0.11	0.00	9.0543
12500	281453	0	0	454207	3905	0	0	2858	0.00	0.09	0.00	10.7790
14500	278483	0	0	420864	3864	0	0	2760	0.00	0.07	0.00	12.5036
16500	275514	0	0	387521	3833	0	0	2685	0.00	0.05	0.00	14.2282

Fig 60: Bearing rotordynamic coefficients

the rotor first critical speed to almost 5000 rpm. Fig 61 shows the natural frequency map with rigid supports and Fig 62 shows the natural frequency map with the rotor on tilt pad bearings and with labyrinth seal effects included at the mid span.

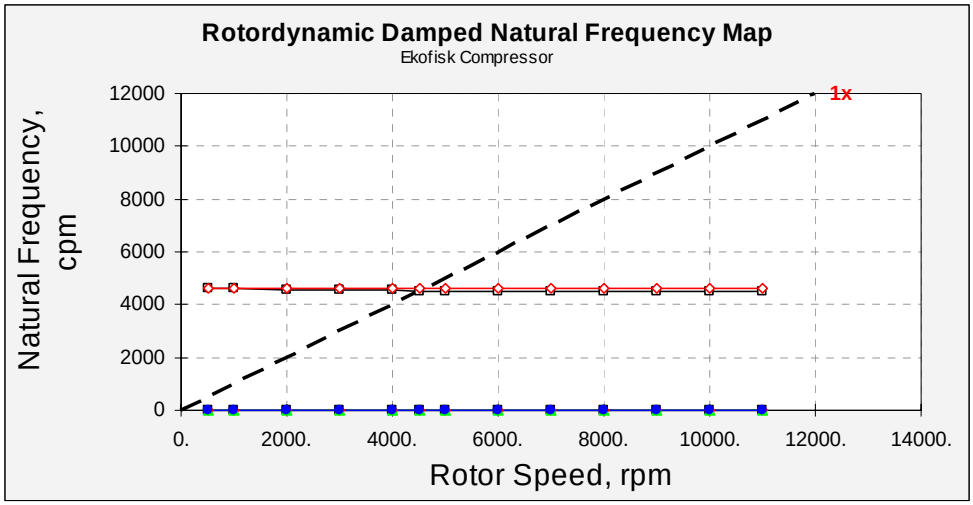

Fig 61: Natural frequency map of rigidly supported rotor

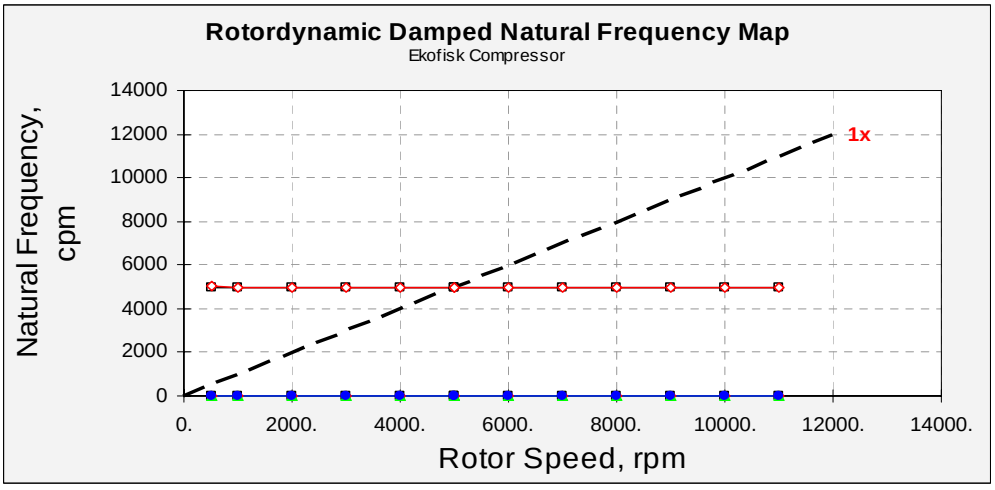

Fig 62: Natural frequency map of rotor on tilt-pad bearings and central labyrinth seal

Fig 63 shows the eigenvalue table obtained when after including impeller and labyrinth cross-coupled forces. It can be seen that the rotor continues to be stable at a speed of 8500 rpm, albeit with just 1.6% effective damping.

Speed	zeta1	cpm1	zeta2	cpm2	zeta3	cpm3	zeta4	cpm4	zeta5	cpm5	zeta6	cpm6	zeta7	cpm7
500.	1.000	0.0	1.000	0.0	1.000	0.0	1.000	11.8	-0.045	4999.7	0.091	5008.4	0.015	16917.8
1000.	1.000	0.0	1.000	0.0	1.000	0.0	1.000	0.0	-0.010	4994.6	0.061	4996.8	0.021	16897.8
2000.	1.000	0.0	1.000	0.0	1.000	0.0	1.000	0.0	0.048	4990.7	0.007	4995.3	0.021	16885.3
3000.	1.000	0.0	1.000	0.0	1.000	0.0	1.000	0.0	0.046	4986.7	0.013	4995.9	0.021	16872.8
4000.	1.000	0.0	1.000	0.0	1.000	0.0	1.000	0.0	0.046	4983.4	0.016	4996.3	0.022	16861.1
4996.	1.000	0.0	1.000	0.0	1.000	0.0	1.000	0.0	0.047	4980.7	0.017	4996.6	0.022	16850.0
5000.	1.000	0.0	1.000	0.0	1.000	0.0	1.000	0.0	0.047	4980.7	0.017	4996.6	0.022	16849.9
6000.	1.000	0.0	1.000	0.0	1.000	0.0	1.000	0.0	0.049	4978.8	0.017	4996.9	0.023	16838.9
7000.	1.000	0.0	1.000	0.0	1.000	0.0	1.000	0.0	0.050	4977.5	0.017	4997.4	0.023	16827.9
8000.	1.000	0.0	1.000	0.0	1.000	0.0	1.000	0.0	0.052	4976.7	0.016	4998.0	0.024	16816.7
9000.	1.000	0.0	1.000	0.0	1.000	0.0	1.000	0.0	0.054	4976.2	0.016	4998.6	0.024	16805.5
10000.	1.000	0.0	1.000	0.0	1.000	0.0	1.000	0.0	0.055	4976.0	0.015	4999.3	0.025	16794.1
11000.	1.000	0.0	1.000	0.0	1.000	0.0	1.000	0.0	0.057	4975.8	0.013	4999.9	0.025	16782.7

Fig 63: Damped eigenvalue table for Ekofisk compressor

Wachel [12] also reports an instance when the rotor becomes unstable at a running speed of 1.25 times the first critical speed. This is also not predicted by incorporating the currently available labyrinth seal/impeller codes. Fig 2 and Fig 3 show the synchronous response and phase angle respectively. The phase angle variation through the critical speed zone is a smooth 180^0 transition.

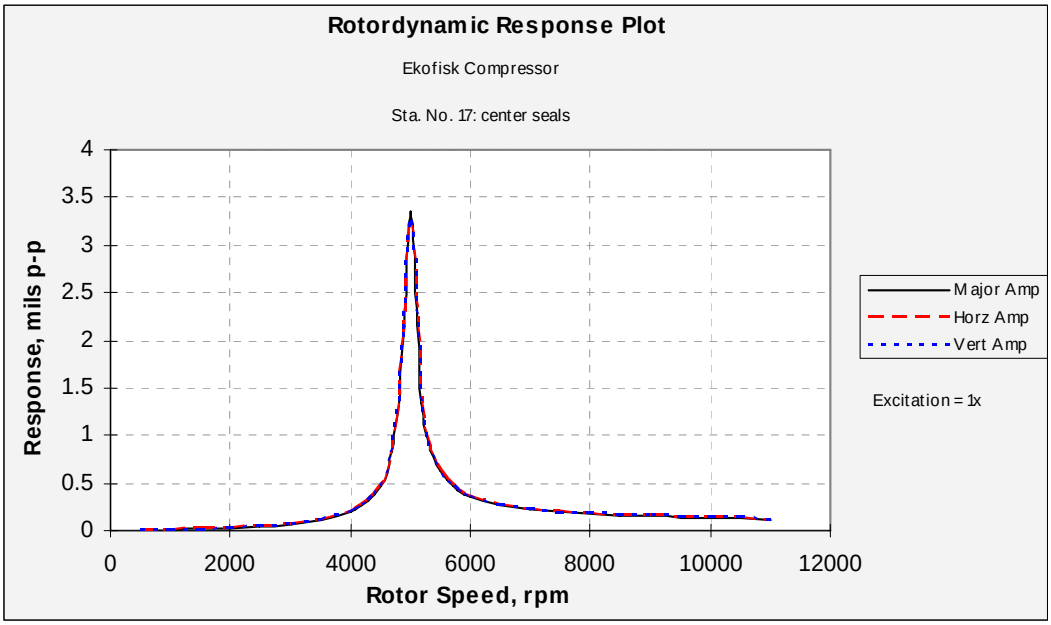

Fig 64: Ekofisk compressor synchronous response

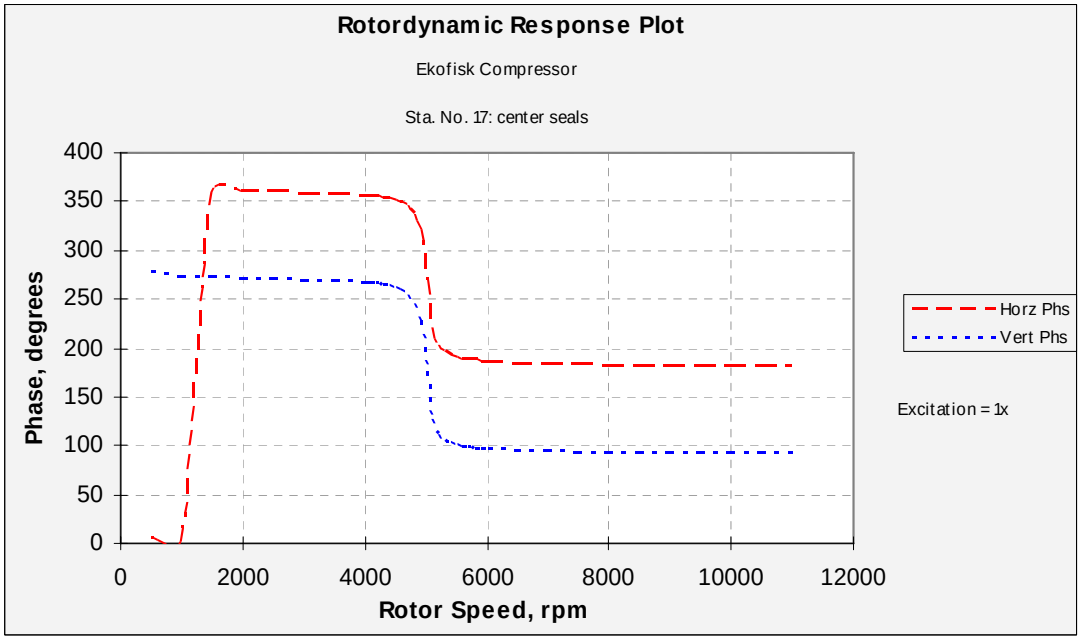

Fig 65: Ekofisk compressor synchronous phase angle

APPENDIX II

LATERAL ROTORDYNAMIC ANALYSIS OF THE KAYBOB COMPRESSOR

The Kaybob compressor that went unstable was the low pressure (LP) compressor in a gas re-injection compressor pair system operated by Chevron-Standard at the Kaybob South Beaverhill Lake at Alberta, Canada. Both the low pressure and the high pressure (HP) had a maximum continuous operating speed of 11,400 rpm. The LP compressor was an eight stage back-to-back compressor having a central labyrinth seal. Detailed data about the design pressures and speeds is not available. However, Smith [[10]] mentions that the rotor went violently unstable when the suction pressure was maintained at 1120 psi (77.2 bar) and the discharge pressure was 3300 psi (228 bar). The overall pressure ratio is 2.95. Assuming that the compression ratio in each impeller is the same, the impeller unit compression ratio is 1.14. The pressures on either side of the labyrinth (@ 11,400 rpm) can be easily calculated as 1922 psi (133 bar) and 3300 psi (228 bar) respectively. It is also further assumed that the pressures vary linearly with speed. Using this data, the rotordynamic coefficients of the labyrinth seal can be computed in XLTRC^2 rotordynamics code. Fig 66 shows the rotordynamic coefficients for an inlet swirl ratio of 0.5 and Fig 67 shows the variation of the cross-coupled stiffness coefficients with speed.

There is no available data regarding the composition of the gases and hence, aerodynamic cross-coupling around the impeller are not applied.

The bearing rotordynamic coefficients are evaluated at a temperature of 124^0F (51^0C) and these are shown in Fig 68.

***Centre Lab Seal* Worksheet for labyrinth seals**

Version 2.0, Copyright 1996 - 1998 by Texas A&M University. All rights reserved.

Title: labyrinth seal_linear

Seal Radius	4.531	in	Ratio of Specific Heats	1.502	--
Radial Clearance	0.009	in	Gas Constant	315.016	ft-lb/ lb^{0}R
Tooth Location	S	R or S	Compressibility Factor	1	--
Number of Teeth	15	--	Kinematic Viscosity	2.57E+01	cst
Tooth Pitch	0.28	in	Reservoir Temperature	210	F
Tooth Height	0.118	in	Reservoir Pressure	Use J	psi
Tooth Width	0.0276	in	Sump Pressure	Use K	psi
Stator Friction Constant	0.079	--	Inlet Tangential Velocity Ratio	0.5	--
Stator Friction Exponent	-0.25	--			
Rotor Friction Constant	0.079	--			
Rotor Friction Exponent	-0.25	--			

									J	K	
Speed	Kxx	Kxy	Kyx	Kyy	Cxx	Cxy	Cyx	Cyy	Res. Press.	Sump Press.	fw
rpm	lb/in	lb/in	lb/in	lb/in	lb-s/in	lb-s/in	lb-s/in	lb-s/in	psi	psi	-
300	3.183E+01	-2.012E+01	2.012E+01	3.183E+01	1.805E+00	4.451E-01	-4.451E-01	1.805E+00	1177.37	1140.31	-0.355
600	2.737E+01	-5.621E+01	5.621E+01	2.737E+01	2.533E+00	9.052E-01	-9.052E-01	2.533E+00	1234.74	1160.61	-0.353
900	-1.111E+01	-1.010E+02	1.010E+02	-1.111E+01	3.134E+00	1.385E+00	-1.385E+00	3.134E+00	1292.11	1180.92	-0.342
1200	-8.513E+01	-1.514E+02	1.514E+02	-8.513E+01	3.678E+00	1.887E+00	-1.887E+00	3.678E+00	1349.47	1201.22	-0.328
1500	-1.967E+02	-2.058E+02	2.058E+02	-1.967E+02	4.191E+00	2.409E+00	-2.409E+00	4.191E+00	1406.84	1221.53	-0.313
1800	-3.482E+02	-2.627E+02	2.627E+02	-3.482E+02	4.687E+00	2.953E+00	-2.953E+00	4.687E+00	1464.21	1241.84	-0.297
2100	-5.419E+02	-3.210E+02	3.210E+02	-5.419E+02	5.173E+00	3.519E+00	-3.519E+00	5.173E+00	1521.58	1262.14	-0.282
2400	-7.803E+02	-3.797E+02	3.797E+02	-7.803E+02	5.653E+00	4.106E+00	-4.106E+00	5.653E+00	1578.95	1282.45	-0.267
2700	-1.066E+03	-4.379E+02	4.379E+02	-1.066E+03	6.131E+00	4.716E+00	-4.716E+00	6.131E+00	1636.32	1302.76	-0.253
3000	-1.401E+03	-4.946E+02	4.946E+02	-1.401E+03	6.608E+00	5.348E+00	-5.348E+00	6.608E+00	1693.68	1323.06	-0.238
3300	-1.789E+03	-5.492E+02	5.492E+02	-1.789E+03	7.087E+00	6.003E+00	-6.003E+00	7.087E+00	1751.05	1343.37	-0.224
3600	-2.231E+03	-6.009E+02	6.009E+02	-2.231E+03	7.569E+00	6.680E+00	-6.680E+00	7.569E+00	1808.42	1363.67	-0.21059
3900	-2.731E+03	-6.486E+02	6.486E+02	-2.731E+03	8.055E+00	7.380E+00	-7.380E+00	8.055E+00	1865.79	1383.98	-0.19717
4200	-3.292E+03	-6.917E+02	6.917E+02	-3.292E+03	8.546E+00	8.102E+00	-8.102E+00	8.546E+00	1923.16	1404.29	-0.18405
4500	-3.915E+03	-7.294E+02	7.294E+02	-3.915E+03	9.043E+00	8.848E+00	-8.848E+00	9.043E+00	1980.53	1424.59	-0.17118
4800	-4.604E+03	-7.607E+02	7.607E+02	-4.604E+03	9.546E+00	9.617E+00	-9.617E+00	9.546E+00	2037.89	1444.90	-0.15855
5100	-5.362E+03	-7.848E+02	7.848E+02	-5.362E+03	1.006E+01	1.041E+01	-1.041E+01	1.006E+01	2095.26	1465.21	-0.14613
5400	-6.191E+03	-8.010E+02	8.010E+02	-6.191E+03	1.058E+01	1.123E+01	-1.123E+01	1.058E+01	2152.63	1485.51	-0.13395
5700	-7.094E+03	-8.080E+02	8.080E+02	-7.094E+03	1.110E+01	1.207E+01	-1.207E+01	1.110E+01	2210.00	1505.82	-0.12193
6000	-8.075E+03	-8.052E+02	8.052E+02	-8.075E+03	1.164E+01	1.293E+01	-1.293E+01	1.164E+01	2267.37	1526.12	-0.110112
6300	-9.135E+03	-7.913E+02	7.913E+02	-9.135E+03	1.218E+01	1.382E+01	-1.382E+01	1.218E+01	2324.74	1546.43	-0.098451
6600	-1.028E+04	-7.656E+02	7.656E+02	-1.028E+04	1.274E+01	1.473E+01	-1.473E+01	1.274E+01	2382.11	1566.74	-0.086954
6900	-1.151E+04	-7.268E+02	7.268E+02	-1.151E+04	1.331E+01	1.567E+01	-1.567E+01	1.331E+01	2439.47	1587.04	-0.075603
7200	-1.283E+04	-6.741E+02	6.741E+02	-1.283E+04	1.388E+01	1.663E+01	-1.663E+01	1.388E+01	2496.84	1607.35	-0.0644
7500	-1.424E+04	-6.058E+02	6.058E+02	-1.424E+04	1.447E+01	1.762E+01	-1.762E+01	1.447E+01	2554.21	1627.65	-0.053305
7800	-1.575E+04	-5.214E+02	5.214E+02	-1.575E+04	1.507E+01	1.864E+01	-1.864E+01	1.507E+01	2611.58	1647.96	-0.042351
8100	-1.735E+04	-4.190E+02	4.190E+02	-1.735E+04	1.569E+01	1.968E+01	-1.968E+01	1.569E+01	2668.95	1668.27	-0.031493
8400	-1.906E+04	-2.979E+02	2.979E+02	-1.906E+04	1.631E+01	2.075E+01	-2.075E+01	1.631E+01	2726.32	1688.57	-0.020761
8700	-2.088E+04	-1.562E+02	1.562E+02	-2.088E+04	1.695E+01	2.184E+01	-2.184E+01	1.695E+01	2783.68	1708.88	-0.010115
9000	-2.280E+04	7.083E+00	-7.083E+00	-2.280E+04	1.761E+01	2.297E+01	-2.297E+01	1.761E+01	2841.05	1729.19	0.000427
9300	-2.484E+04	1.937E+02	-1.937E+02	-2.484E+04	1.828E+01	2.412E+01	-2.412E+01	1.828E+01	2898.42	1749.49	0.010886
9600	-2.699E+04	4.049E+02	-4.049E+02	-2.699E+04	1.896E+01	2.530E+01	-2.530E+01	1.896E+01	2955.79	1769.80	0.021246
9900	-2.927E+04	6.428E+02	-6.428E+02	-2.927E+04	1.966E+01	2.651E+01	-2.651E+01	1.966E+01	3013.16	1790.10	0.031541
10200	-3.167E+04	9.086E+02	-9.086E+02	-3.167E+04	2.038E+01	2.775E+01	-2.775E+01	2.038E+01	3070.53	1810.41	0.041751
10500	-3.419E+04	1.204E+03	-1.204E+03	-3.419E+04	2.111E+01	2.902E+01	-2.902E+01	2.111E+01	3127.89	1830.72	0.051899
10800	-3.685E+04	1.532E+03	-1.532E+03	-3.685E+04	2.186E+01	3.031E+01	-3.031E+01	2.186E+01	3185.26	1851.02	0.061981
11100	-3.964E+04	1.893E+03	-1.893E+03	-3.964E+04	2.263E+01	3.164E+01	-3.164E+01	2.263E+01	3242.63	1871.33	0.071995
11400	-4.258E+04	2.290E+03	-2.290E+03	-4.258E+04	2.342E+01	3.301E+01	-3.301E+01	2.342E+01	3300.00	1891.64	0.081919

Fig 66: Rotordynamic coefficients for the central labyrinth seal

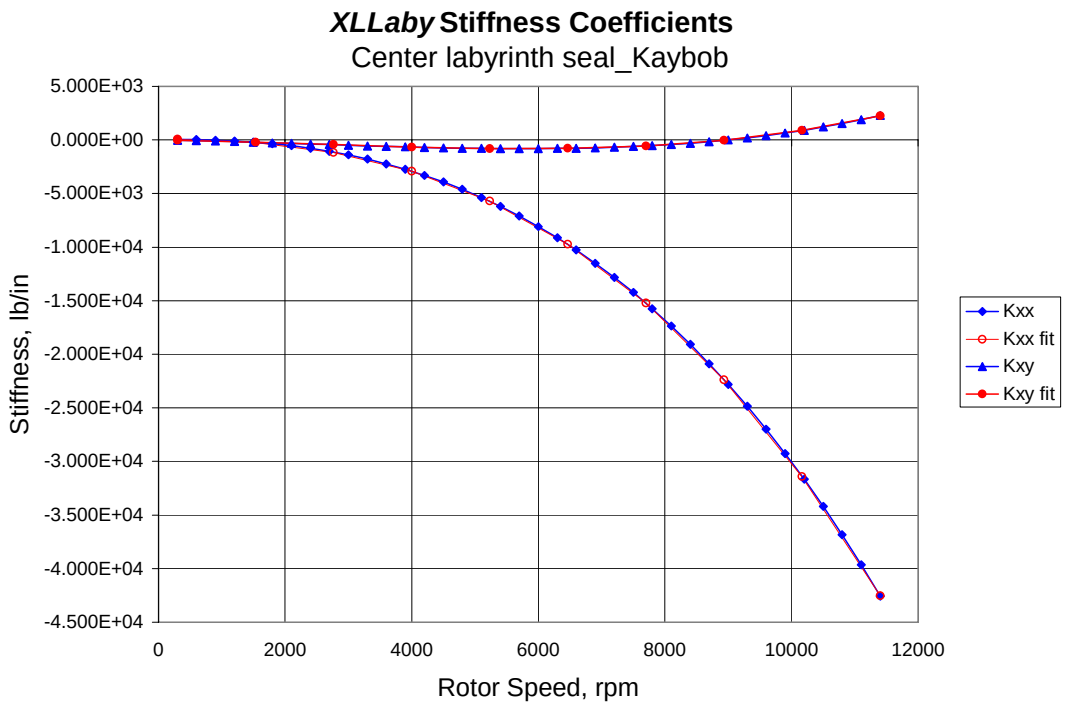

Fig 67: Variation of direct and cross-coupled stiffness coefficients with speed

5-Tilt Pad Spreadsheet for Journal Bearing Coefficients

Title: 5 tilt pad brng

Bearing Type: 5 Pad Tilting, LOP

Bearing L/D	0.8	--
Bearing Diameter	4.14	inches
Pad Clr, Cp	0.008	inches
Bearing Load, F	650	lbf
Bearing Preload, m	0.2	--

Lubricant Viscosity	0.0000024	Reyns
Lubricant Density	0.85	sp. gr.

Speed	Kxx	Kxy	Kyx	Kyy	Cxx	Cxy	Cyx	Cyy	W.F.R.	Ecc.	Attan.	Somm.
rpm	lb/in	lb/in	lb/in	lb/in	lb-s/in	lb-s/in	lb-s/in	lb-s/in			deg	
500	98105	0	0	1252507	2889	0	0	14061	0.00	0.68	0.00	0.1130
2500	279254	0	0	709860	2146	0	0	3161	0.00	0.39	0.00	0.5649
4500	421910	0	0	681904	1970	0	0	2165	0.00	0.26	0.00	1.0169
6500	582964	0	0	758851	1931	0	0	1877	0.00	0.19	0.00	1.4688
8500	775854	0	0	911428	1946	0	0	1793	0.00	0.14	0.00	1.9208
10500	968743	0	0	1064005	1956	0	0	1742	0.00	0.10	0.00	2.3727
12500	1242487	0	0	1323701	2027	0	0	1791	0.00	0.09	0.00	2.8247
14500	1520423	0	0	1588951	2082	0	0	1831	0.00	0.07	0.00	3.2766
16500	1798359	0	0	1854201	2123	0	0	1862	0.00	0.05	0.00	3.7286

Fig 68: Bearing rotordynamic coefficients

Using these values, a lateral rotordynamic analysis was carried out and the natural frequency map is show in Fig 69. The first critical speed is found to be at about 4520 rpm. The damped eigenvalue table is shown in Fig 70.

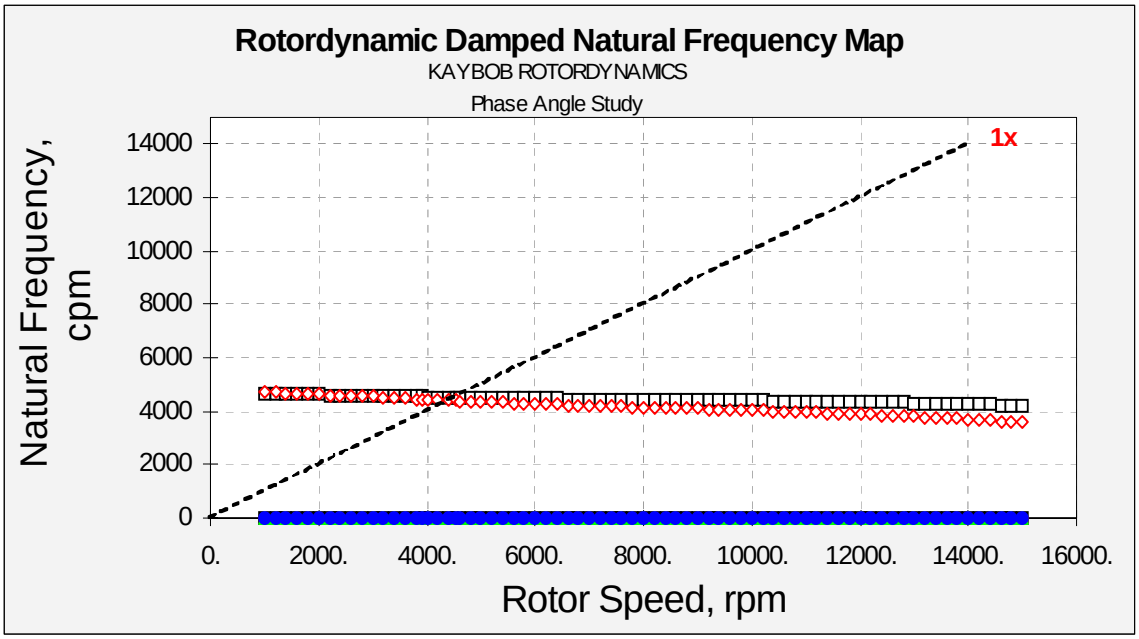

Fig 69: Natural frequency map for the Kaybob compressor

Speed	zeta1	cpm1	zeta2	cpm2	zeta3	cpm3	zeta4	cpm4	zeta5	cpm5	zeta6	cpm6
1000.	1.000	0.0	1.000	0.0	1.000	0.0	1.000	0.0	0.104	4677.8	0.036	4704.6
1200.	1.000	0.0	1.000	0.0	1.000	0.0	1.000	0.0	0.108	4665.0	0.042	4691.1
1400.	1.000	0.0	1.000	0.0	1.000	0.0	1.000	0.0	0.110	4653.2	0.048	4676.5
1600.	1.000	0.0	1.000	0.0	1.000	0.0	1.000	0.0	0.112	4642.1	0.053	4661.0
1800.	1.000	0.0	1.000	0.0	1.000	0.0	1.000	0.0	0.114	4631.4	0.059	4644.7
2000.	1.000	0.0	1.000	0.0	1.000	0.0	1.000	0.0	0.116	4621.1	0.064	4627.8
2200.	1.000	0.0	1.000	0.0	1.000	0.0	1.000	0.0	0.117	4611.0	0.068	4610.5
2400.	1.000	0.0	1.000	0.0	1.000	0.0	1.000	0.0	0.118	4601.2	0.073	4592.8
2600.	1.000	0.0	1.000	0.0	1.000	0.0	1.000	0.0	0.119	4591.6	0.077	4574.8
2800.	1.000	0.0	1.000	0.0	1.000	0.0	1.000	0.0	0.119	4582.4	0.080	4556.5
3000.	1.000	0.0	1.000	0.0	1.000	0.0	1.000	0.0	0.119	4573.5	0.084	4538.0
3200.	1.000	0.0	1.000	0.0	1.000	0.0	1.000	0.0	0.120	4565.2	0.087	4519.1
3400.	1.000	0.0	1.000	0.0	1.000	0.0	1.000	0.0	0.120	4557.3	0.090	4500.1
3600.	1.000	0.0	1.000	0.0	1.000	0.0	1.000	0.0	0.119	4549.9	0.092	4480.8
3800.	1.000	0.0	1.000	0.0	1.000	0.0	1.000	0.0	0.119	4543.0	0.094	4461.6
3900.	1.000	0.0	1.000	0.0	1.000	0.0	1.000	0.0	0.119	4539.6	0.095	4452.0
4000.	1.000	0.0	1.000	0.0	1.000	0.0	1.000	0.0	0.119	4536.3	0.096	4442.5
4200.	1.000	0.0	1.000	0.0	1.000	0.0	1.000	0.0	0.119	4529.8	0.097	4423.7
4400.	1.000	0.0	1.000	0.0	1.000	0.0	1.000	0.0	0.118	4523.4	0.098	4405.3
4520.	1.000	0.0	1.000	0.0	1.000	0.0	1.000	0.0	0.118	4519.5	0.099	4394.6
4600.	1.000	0.0	1.000	0.0	1.000	0.0	1.000	0.0	0.118	4516.9	0.099	4387.5
4800.	1.000	0.0	1.000	0.0	1.000	0.0	1.000	0.0	0.118	4510.5	0.100	4370.2
5000.	1.000	0.0	1.000	0.0	1.000	0.0	1.000	0.0	0.117	4504.2	0.100	4353.5
5200.	1.000	0.0	1.000	0.0	1.000	0.0	1.000	0.0	0.116	4497.9	0.100	4337.3
5400.	1.000	0.0	1.000	0.0	1.000	0.0	1.000	0.0	0.116	4491.7	0.100	4321.5
5600.	1.000	0.0	1.000	0.0	1.000	0.0	1.000	0.0	0.115	4485.7	0.099	4306.3
5800.	1.000	0.0	1.000	0.0	1.000	0.0	1.000	0.0	0.114	4479.9	0.099	4291.4
6000.	1.000	0.0	1.000	0.0	1.000	0.0	1.000	0.0	0.113	4474.2	0.098	4277.0
6200.	1.000	0.0	1.000	0.0	1.000	0.0	1.000	0.0	0.112	4468.8	0.097	4262.9
6400.	1.000	0.0	1.000	0.0	1.000	0.0	1.000	0.0	0.110	4463.6	0.096	4249.2
6600.	1.000	0.0	1.000	0.0	1.000	0.0	1.000	0.0	0.109	4458.6	0.095	4235.8
6800.	1.000	0.0	1.000	0.0	1.000	0.0	1.000	0.0	0.108	4453.8	0.094	4222.7
7000.	1.000	0.0	1.000	0.0	1.000	0.0	1.000	0.0	0.106	4449.2	0.093	4209.8
7200.	1.000	0.0	1.000	0.0	1.000	0.0	1.000	0.0	0.105	4444.8	0.092	4197.2
7400.	1.000	0.0	1.000	0.0	1.000	0.0	1.000	0.0	0.104	4440.7	0.091	4184.7
7600.	1.000	0.0	1.000	0.0	1.000	0.0	1.000	0.0	0.102	4436.6	0.090	4172.4
7800.	1.000	0.0	1.000	0.0	1.000	0.0	1.000	0.0	0.101	4432.8	0.088	4160.2
8000.	1.000	0.0	1.000	0.0	1.000	0.0	1.000	0.0	0.099	4429.0	0.087	4148.1
8200.	1.000	0.0	1.000	0.0	1.000	0.0	1.000	0.0	0.097	4425.4	0.086	4136.1
8400.	1.000	0.0	1.000	0.0	1.000	0.0	1.000	0.0	0.096	4421.8	0.085	4124.1
8600.	1.000	0.0	1.000	0.0	1.000	0.0	1.000	0.0	0.094	4418.3	0.083	4112.1
8800.	1.000	0.0	1.000	0.0	1.000	0.0	1.000	0.0	0.093	4414.9	0.082	4100.1
9000.	1.000	0.0	1.000	0.0	1.000	0.0	1.000	0.0	0.091	4411.5	0.081	4088.0
9200.	1.000	0.0	1.000	0.0	1.000	0.0	1.000	0.0	0.090	4408.0	0.080	4075.9
9400.	1.000	0.0	1.000	0.0	1.000	0.0	1.000	0.0	0.088	4404.6	0.079	4063.6
9600.	1.000	0.0	1.000	0.0	1.000	0.0	1.000	0.0	0.087	4401.1	0.078	4051.1
9800.	1.000	0.0	1.000	0.0	1.000	0.0	1.000	0.0	0.085	4397.5	0.077	4038.5
10000.	1.000	0.0	1.000	0.0	1.000	0.0	1.000	0.0	0.084	4393.8	0.076	4025.7
10200.	1.000	0.0	1.000	0.0	1.000	0.0	1.000	0.0	0.082	4389.9	0.075	4012.6
10400.	1.000	0.0	1.000	0.0	1.000	0.0	1.000	0.0	0.081	4386.0	0.074	3999.3
10600.	1.000	0.0	1.000	0.0	1.000	0.0	1.000	0.0	0.079	4381.8	0.074	3985.7
10800.	1.000	0.0	1.000	0.0	1.000	0.0	1.000	0.0	0.078	4377.5	0.073	3971.8
11000.	1.000	0.0	1.000	0.0	1.000	0.0	1.000	0.0	0.076	4373.0	0.072	3957.6
11200.	1.000	0.0	1.000	0.0	1.000	0.0	1.000	0.0	0.075	4368.2	0.072	3943.0
11400.	1.000	0.0	1.000	0.0	1.000	0.0	1.000	0.0	0.074	4363.2	0.071	3928.1
11600.	1.000	0.0	1.000	0.0	1.000	0.0	1.000	0.0	0.072	4357.9	0.071	3912.8
11800.	1.000	0.0	1.000	0.0	1.000	0.0	1.000	0.0	0.071	4352.4	0.071	3897.1
12000.	1.000	0.0	1.000	0.0	1.000	0.0	1.000	0.0	0.070	4346.5	0.070	3880.9
12200.	1.000	0.0	1.000	0.0	1.000	0.0	1.000	0.0	0.068	4340.3	0.070	3864.3
12400.	1.000	0.0	1.000	0.0	1.000	0.0	1.000	0.0	0.067	4333.8	0.070	3847.3
12600.	1.000	0.0	1.000	0.0	1.000	0.0	1.000	0.0	0.066	4326.9	0.070	3829.7
12800.	1.000	0.0	1.000	0.0	1.000	0.0	1.000	0.0	0.065	4319.7	0.070	3811.7
13000.	1.000	0.0	1.000	0.0	1.000	0.0	1.000	0.0	0.064	4312.0	0.070	3793.1
13200.	1.000	0.0	1.000	0.0	1.000	0.0	1.000	0.0	0.062	4304.0	0.071	3774.0
13400.	1.000	0.0	1.000	0.0	1.000	0.0	1.000	0.0	0.061	4295.5	0.071	3754.4
13600.	1.000	0.0	1.000	0.0	1.000	0.0	1.000	0.0	0.060	4286.6	0.072	3734.2
13800.	1.000	0.0	1.000	0.0	1.000	0.0	1.000	0.0	0.059	4277.2	0.072	3713.4
14000.	1.000	0.0	1.000	0.0	1.000	0.0	1.000	0.0	0.058	4267.4	0.073	3692.0
14200.	1.000	0.0	1.000	0.0	1.000	0.0	1.000	0.0	0.056	4257.0	0.074	3670.1
14400.	1.000	0.0	1.000	0.0	1.000	0.0	1.000	0.0	0.055	4246.2	0.075	3647.4
14600.	1.000	0.0	1.000	0.0	1.000	0.0	1.000	0.0	0.054	4234.8	0.076	3624.1
14800.	1.000	0.0	1.000	0.0	1.000	0.0	1.000	0.0	0.053	4222.9	0.077	3600.2
15000.	1.000	0.0	1.000	0.0	1.000	0.0	1.000	0.0	0.052	4210.5	0.078	3575.6

Fig 70: Damped eigenvalue table for Kaybob compressor

It can be seen from the eigenvalue table that the rotor is stable for all speeds up to its maximum operating speed. The labyrinth seal codes by themselves do not accurately predict the onset speed of instability correctly. Fig 71 and Fig 72 show the synchronous response and phase angle respectively. The phase angle change through the critical speed is a smooth 180^0 transition.

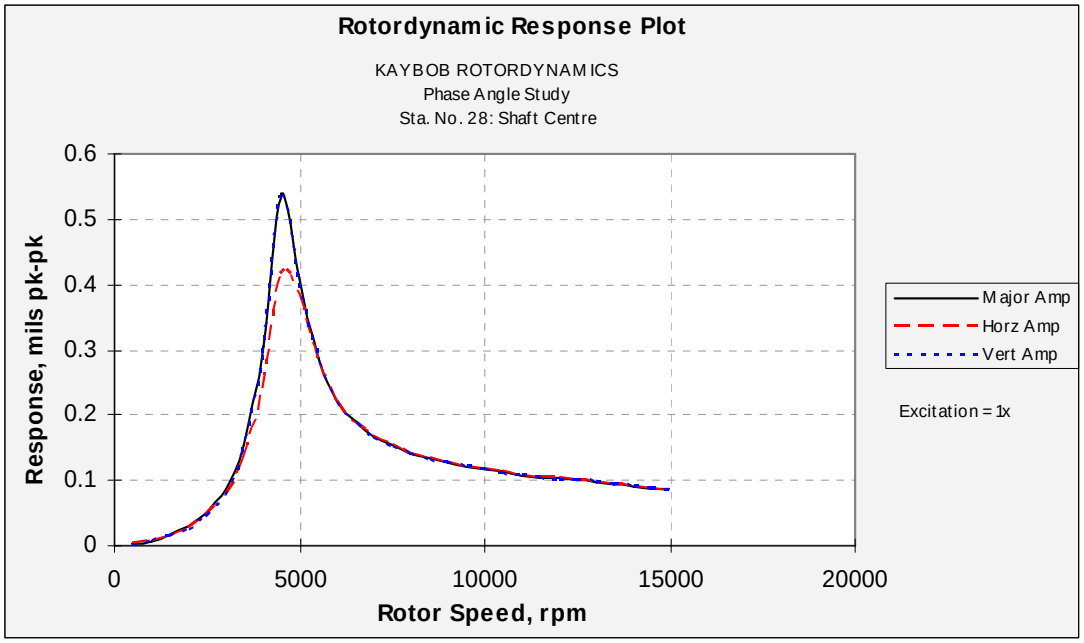

Fig 71: Kaybob compressor synchronous response

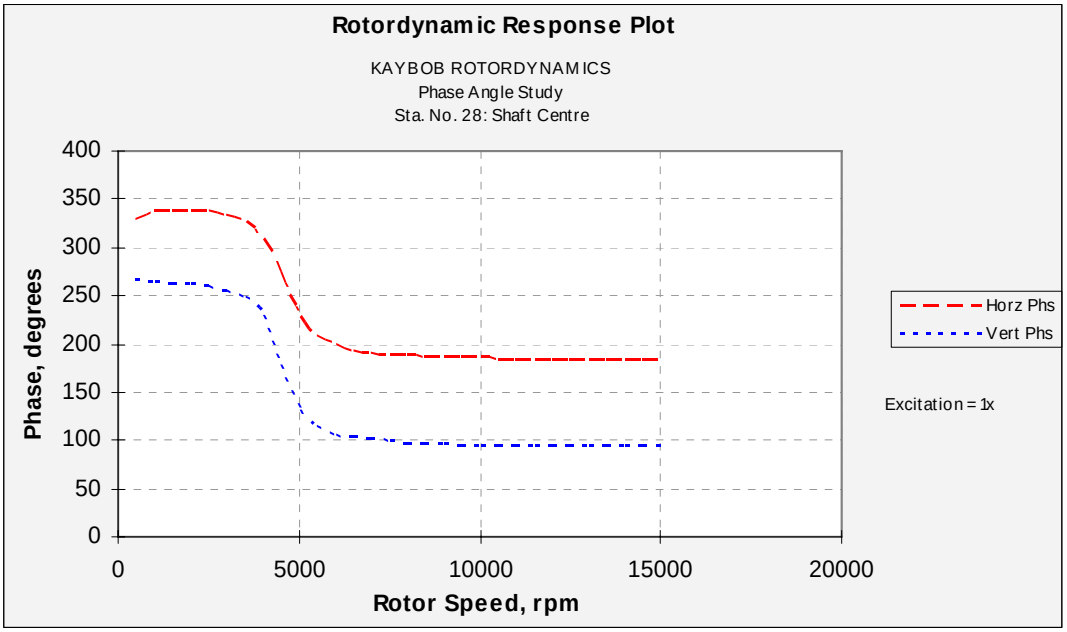

Fig 72: Kaybob compressor synchronous phase angle

APPENDIX III

LATERAL ROTORDYNAMIC ANALYSIS OF THE COUPLED TORSIONAL-LATERAL VIBRATIONS TEST RIG

A lateral rotordynamic analysis was performed on both the primary and secondary shafts to determine their critical speeds. XLTRC^2 rotordynamics code was used for the analysis.

Primary Shaft

The geometric dimensioning and layout of the primary shaft is explained in Section 2. Fig 73 below shows XLTRC^2 the rotordynamic model for the primary shaft.

The three ball-bearings were modeled with a high stiffness value of 300,000 lb/in and a very low damping value of 1.0E-5 lb-s/in An imbalance of 1.0E-5 oz-in was introduced at larger diameter section of the gear (station 8). The eigenvalue analysis showed the first critical speed to be at 6900 rpm and the second at around 30,000 rpm. Fig 74 shows the Natural Frequency Map and Fig 75 shows the mode shape of the first mode.

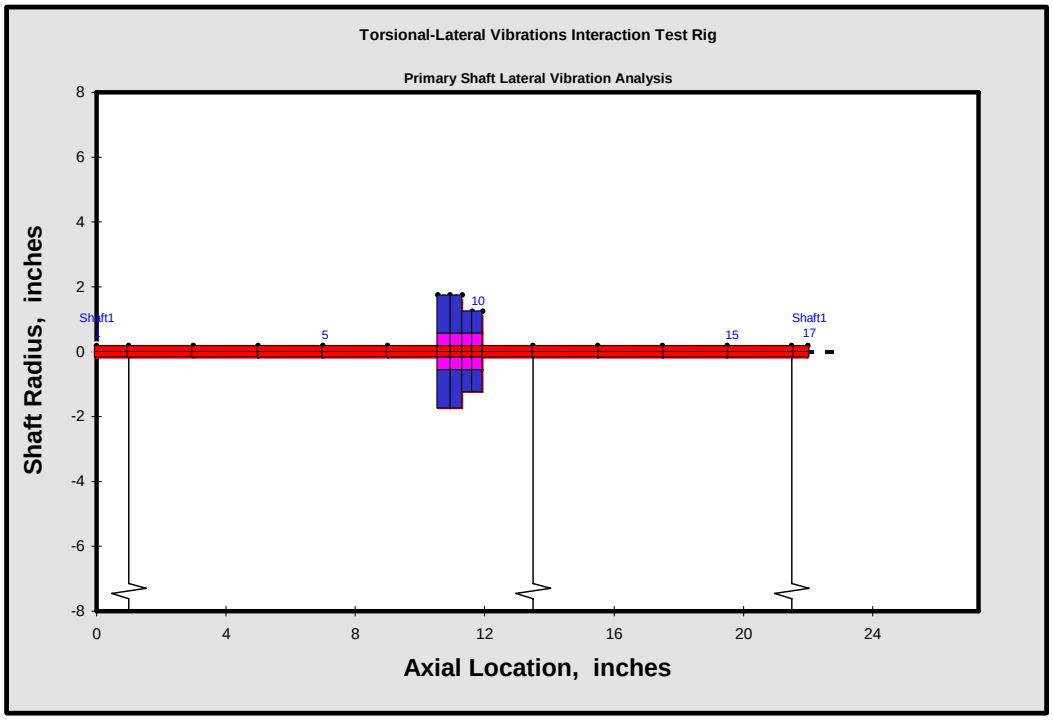

Fig 73: XLTRC^2 model of the primary shaft

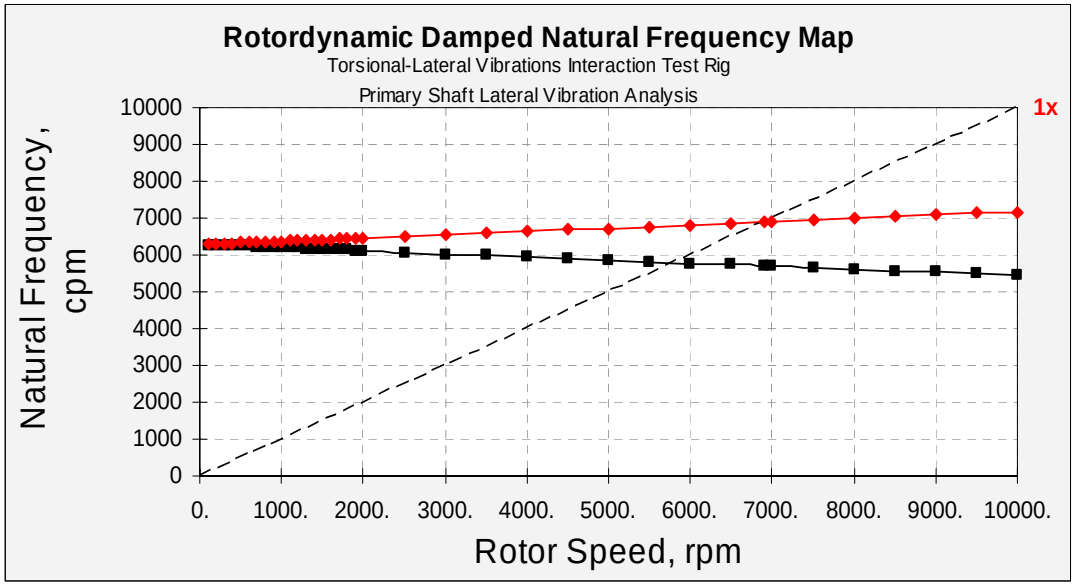

Fig 74: Natural frequency map for the primary shaft

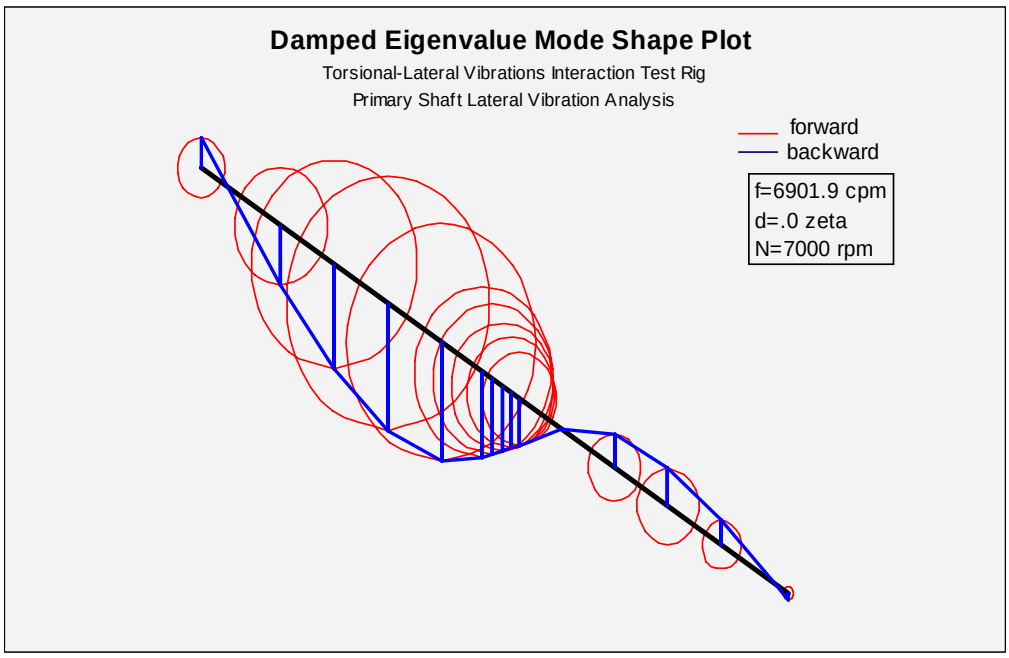

Fig 75: First mode shape of the primary shaft

Secondary Shaft

The geometric dimensioning and layout of the secondary shaft is explained in Section 2. Fig 76 below shows XLTRC^2 the rotordynamic model for the secondary shaft. As in the case of the primary shaft, ball-bearings were modeled with a high stiffness value of 300,000 lb/in and a very low damping value of 1.0E-5 lb-s/in An imbalance of 1.0E-5 oz-in was introduced at larger diameter section of the gear (station 6) and another imbalance of 1.0E-4 was introduced at the break-wheel end (station 24). The eigenvalue analysis showed the first critical speed to be at 4000 rpm and the second at around

10,000 rpm. Fig 77 shows the Natural Frequency Map and Fig 78 shows the mode shape of the first mode.

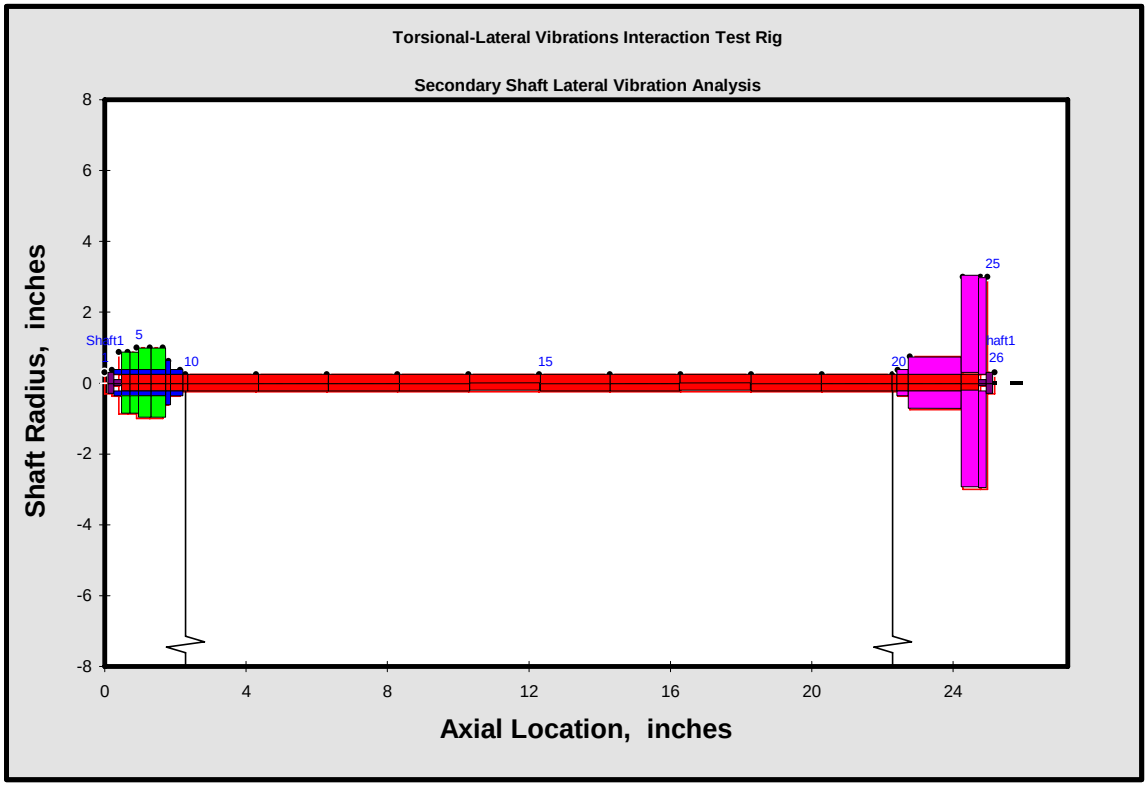

Fig 76: Geometric plot of the secondary shaft in XLTRC[2]

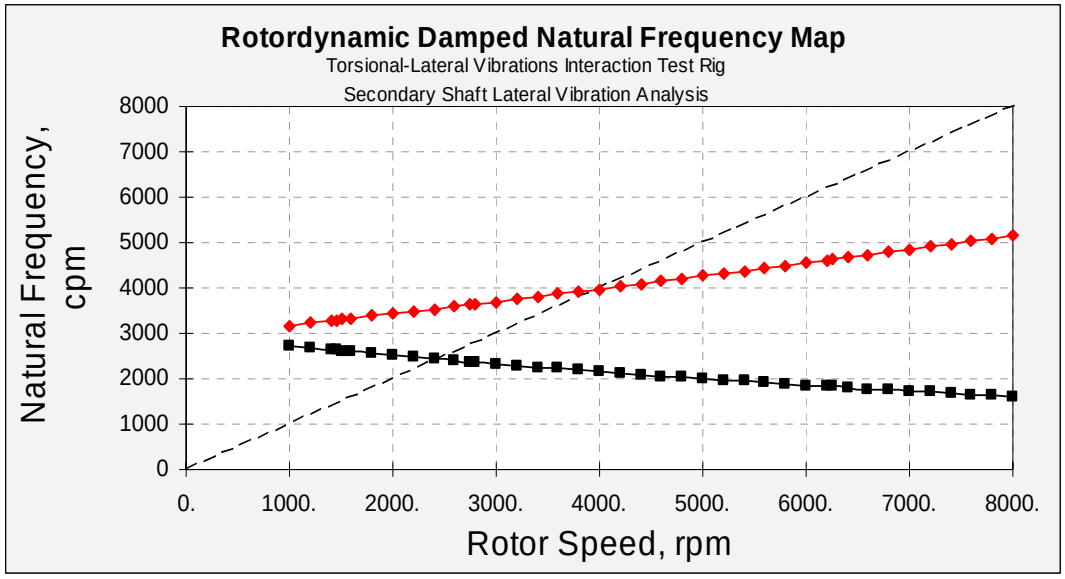

Fig 77: Natural frequency map for the secondary shaft

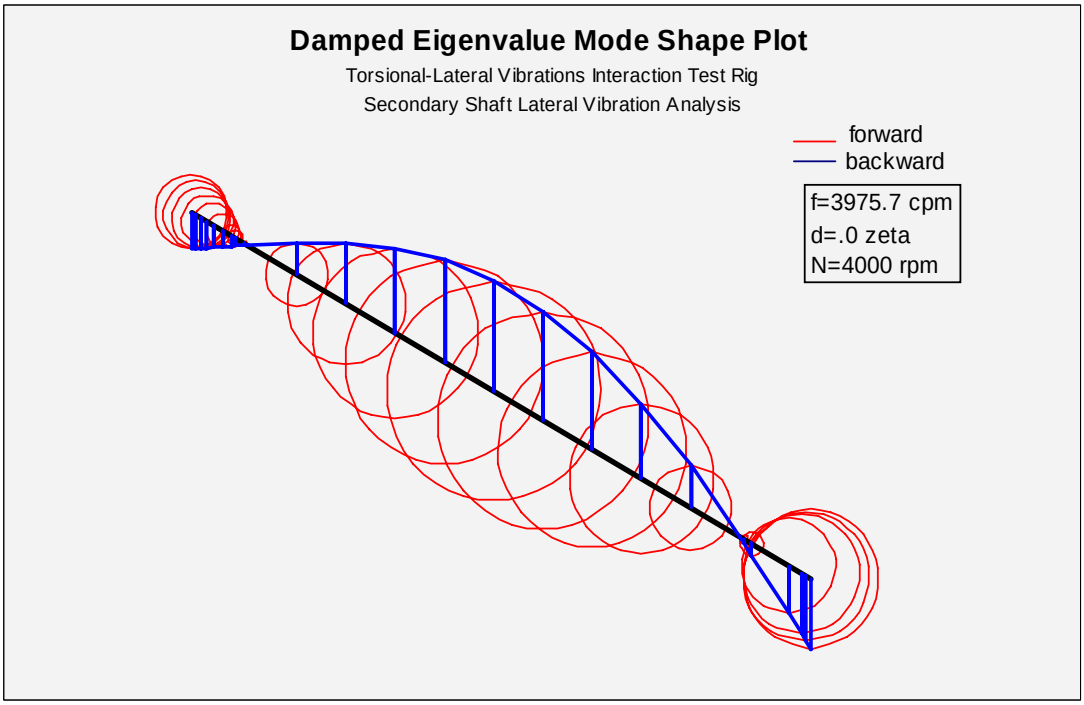

Fig 78: First mode shape for the secondary shaft

APPENDIX IV

EVALUATING INERTIA OF D.C. MOTOR

The inertia of the D.C. motor including the coupling was evaluated experimentally. A few turns of a thin nylon chord was wrapped around the coupling and dead weights were hung at the end of the chord. The time taken by these dead-weights to fall through a pre-determined distance was recorded. Also, the minimum weight to get the motor to just start turning was noted. This was done to account for the friction due to the brushes in the motor. These values were input into the mathematical model below to calculate the inertia of the motor.

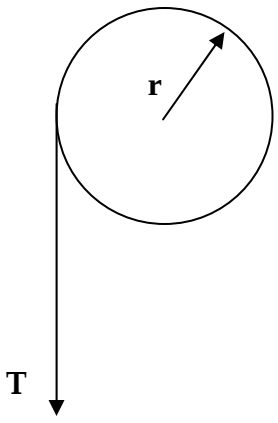

Motor Inertia

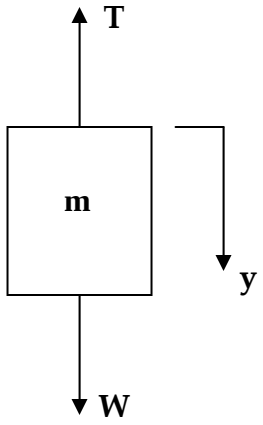

Falling Mass

$$rT - rW_f = I\ddot{\theta} \quad \ldots\ldots(1B)$$

$$W - T = m\ddot{y} = mr\ddot{\theta} \quad \ldots\ldots(2B)$$

Where,

r = radius where the dead weights are suspended

W = weight of the suspended mass

W_f = minimum weight required to turn the motor shaft

T = tension in the chord

Substituting for 'T' from equation 2B into 1B, we get

$$rW - rW_f = (I + mr^2)\ddot{\theta} \quad \text{.....(3B)}$$

If "S" is the distance through which the dead-weight falls, and "t" is the time taken, then,

$$\ddot{\theta} = \frac{2S}{rt^2} \quad \text{.....(4B)}$$

Substituting the value for from 4B into 3B, we get

$$rW - rW_f = (I + mr^2)\frac{2S}{rt^2} \quad \text{.....(5B)}$$

The following values are substituted into the above equation –

r = 1.5in (38.1 mm)

Wf = 4.851 lb (21.63 N)

W = 6.616 lb (29.50 N)

m = 0.017 snail (3.01 kg)

S = 19in (482 mm)

t = 2.42 seconds

The moment of inertia 'I' for the motor is obtained as, I = 0.574 lb-in-sec^2 (0.0648 kg-m^2).

VITA

Vinayaka Narayanan Rajagopalan was born in Chennai, India. He is the son of N. Rajagopalan and Vijayalakshmi Rajagopalan. He completed his high school from Bishop Cotton Boys' School, Bangalore, India and joined R.V. College of Engineering, in Bangalore, India in 1997. After receiving his Bachelor of Engineering in mechanical engineering in September 2001, he worked for TurboTech Precision Engineering (P) Ltd., in Bangalore, India as a design engineer for three years. He then pursued his graduate course in mechanical engineering at Texas A&M University in September 2005. After completing his degree requirements, he plans to work for Solar Turbines in San Diego, California in an engineering position.

Vinayaka Narayanan Rajagopalan
Department of Mechanical Engineering,
3123 TAMU, College Station, Texas 77843
USA